Western University
Scholarship@Western

Digitized Theses | Digitized Special Collections

1993

Surface Modifications Of Silicon Induced By Low Energy Reactive Ion Bombardment

Wayne Harold Chang

Follow this and additional works at: https://ir.lib.uwo.ca/digitizedtheses

Recommended Citation

Chang, Wayne Harold, "Surface Modifications Of Silicon Induced By Low Energy Reactive Ion Bombardment" (1993). *Digitized Theses*. 2279.
https://ir.lib.uwo.ca/digitizedtheses/2279

This Dissertation is brought to you for free and open access by the Digitized Special Collections at Scholarship@Western. It has been accepted for inclusion in Digitized Theses by an authorized administrator of Scholarship@Western. For more information, please contact tadam@uwo.ca, wlswadmin@uwo.ca.

SURFACE MODIFICATIONS

OF

SILICON

INDUCED BY

LOW ENERGY

REACTIVE ION BOMBARDMENT

by

Wayne Harold Chang

Faculty of Engineering Science

Submitted in partial fulfillment

of the requirements for the degree of

Doctor of Philosophy

Faculty of Graduate Studies

The University of Western Ontario

London, Ontario

September 1993

© Wayne Harold Chang 1993

National Library of Canada

Acquisitions and Bibliographic Services Branch

395 Wellington Street
Ottawa, Ontario
K1A 0N4

Bibliothèque nationale du Canada

Direction des acquisitions et des services bibliographiques

395, rue Wellington
Ottawa (Ontario)
K1A 0N4

Your file Votre référence

Our file Notre référence

The author has granted an irrevocable non-exclusive licence allowing the National Library of Canada to reproduce, loan, distribute or sell copies of his/her thesis by any means and in any form or format, making this thesis available to interested persons.

L'auteur a accordé une licence irrévocable et non exclusive permettant à la Bibliothèque nationale du Canada de reproduire, prêter, distribuer ou vendre des copies de sa thèse de quelque manière et sous quelque forme que ce soit pour mettre des exemplaires de cette thèse à la disposition des personnes intéressées.

The author retains ownership of the copyright in his/her thesis. Neither the thesis nor substantial extracts from it may be printed or otherwise reproduced without his/her permission.

L'auteur conserve la propriété du droit d'auteur qui protège sa thèse. Ni la thèse ni des extraits substantiels de celle-ci ne doivent être imprimés ou autrement reproduits sans son autorisation.

ISBN 0-315-83954-6

Canada

ABSTRACT

The effects of low energy reactive ion bombardment of semiconducting silicon material have been investigated by X-ray photoelectron spectroscopy. The residual surface damage induced by a conventional fluorocarbon plasma reactive ion etching of silicon consisted of a uniform fluorocarbon deposited film approximately 4nm in thickness which covered a silicon compound reaction layer. This reaction layer was comprised of silicon oxides, carbide and fluorosilyl species distributed in depth to approximately 2nm. The removal of the residual surface damage was accomplished by an ozone oxidation plus a wet oxide chemical etching step processing and monitored by surface charge spectroscopy. This residual surface damage to silicon was simulated by mass-filtered reactive F^+, and CF^+ ion beam bombardment of silicon at normal incidence and room temperature. In addition, the effects of Cl^+ ion beam bombardment of silicon were studied in order to provide fundamental information on the chlorine plasma dry etching. The ion kinetic energy range of interest was 1eV to 100eV for ion doses between $3x10^{14}$ and $1x10^{18}/cm^2$. The residual surface damage to the silicon was seen as surface incorporation of the reactive ion species in the form of a fluorosilyl species layer for F^+ bombardment, a fluorocarbon deposited layer and a silicon carbide/fluorosilyl layer for CF^+ bombardment, and finally, surface oxidation and subsequent sputtering of the oxygenated species by Cl^+ bombardment. The surface species of SiX_n with X=F or Cl, and for n ranging from 1 to 4 were different for the two halogen ions investigated. For Cl^+ bombardment, n was less than 2 for the ion energy range of 1 to 100eV, while for F^+ ions, n included 1 to 4. Distinct surface reaction products were consistent with the reactivity of the specific ion/silicon systems

ACKNOWLEDGEMENTS

I would like to sincerely thank my Faculty Advisor, Dr. Leo W.M. Lau for his tremendous support, encouragement and confidence in me throughout my entire stay as a graduate student under his supervision. He has provided an environment of tremendous freedom for his research group tempered with demanding standards. I owe everything that I have learned to him.

To the Microelectronics Group, I have learned so much, both tangible and intangible. Many thanks to Dr. Igor Bello for sharing his insights into ion beam technology and vacuum physics. He is one of the finest individuals that I have had the privilege of working with in the Group. Many thanks also go to Dr. Liji Huang for his inumerable support in a variety of ways. He exemplifies intuition and efficiency. To Dr. Raymund Kwok (presently Faculty Member, Department of Chemistry, Chinese University of Hong Kong), I express my gratitude for all his friendship and support, sense of humour, and positive adrenaline!

To Surface Science Western, I would like to sincerely thank Dr. Stewart McIntyre (Director) for providing such a dynamic environment to learn, adapt and be pro-active. His dedication and devotion to the development of one of the very best comprehensive surface analysis facilities is passionate. To the entire staff of S.S.W., I thank them very, very much for all their help in so many ways. The list is longer than the number of pages in this manuscript.

To my fellow graduate students past, Dr. Richard Mycroft, Dr. Bernie Flinn and Laura Flinn, and Dr. Perry Spevack I will always remember their generosity and friendship. To my fellow graduate student soon-to-be past, Steven Splinter I will

always remember his intuitive and insightful discussions. He is the very finest graduate student that I have had the honour and good fortune of knowing.

To Albert Chan (graduate student soon-to-be past), I would like to thank him for his support and friendship over my entire duration as a graduate student. I am amazed at how someone can consume four times his bodyweight in food at buffet restaurants!!

To the Department of Materials Engineering, I express my sincere thanks for financial support in the form of undergraduate Teaching Assistanships.

I would like to thank sincerely Dr. Tom Abraham, Northern Telecom Electronics Ltd, for providing the device quality Si wafers used in this research

TABLE OF CONTENTS

Page

CERTIFICATE OF EXAMINATION. ii

ABSTRACT. iii

ACKNOWLEDGEMENTS. iv

TABLE OF CONTENTS. vi

LIST OF TABLES. x

LIST OF FIGURES. xi

CHAPTER 1. INTRODUCTION. 1

1.1 Objectives of the thesis. 1

1.2 Scope of investigation. 1

CHAPTER 2. GENERAL REVIEW. 2

2.1 Semiconductor silicon. 2

2.1.1 Material properties. 2

2.1.2 Microelectronic device fabrication. 4

2.2 Dry etching processes. 7

2.2.1 Physical etching. 8

2.2.2 Chemical etching. 8

2.2.3 Physico-chemical etching. 9

2.3 Reactive ion etching of silicon. 12

2.3.1 Plasma chemistry. 12

2.3.2 Residual surface damage. 13

2.3.3 Future trends. 16

References. 17

CHAPTER 3. INSTRUMENTAL METHODS. 20

3.1 Introduction. 20

3.2 Sample preparation. 20

3.3 Ultra-high vacuum considerations. 21

3.4 Generation of low energy, mass-filtered ion beams. 22

3.4.1 The custom-built, low energy ion beam system. 22

3.4.2 Ion source. 26

3.4.3 Beam focussing. 27

3.4.4 Ion beam mass-separation. 28

3.4.5 Beam deceleration. 29

3.4.6 Ion mass and kinetic energy characterization. 29

3.4.7 Ion dose determination. 33

3.4.8 Vacuum transfer. 34

3.5 Surface Analysis: X-ray photoelectron spectroscopy. . . . 35

3.5.1 Concepts and principles. 35

3.5.2 Elemental identification. 38

3.5.3 Chemical state identification. 41

3.5.4 Non-destructive shallow depth-profiling. 42

3.5.5 Destructive ultra-shallow depth-profiling. 48

3.5.6 Surface charging spectroscopy. 51

3.5.7 Instrumentation. 53

3.5.8 Quantitative analysis. 57

References. 61

CHAPTER 4. RIE OF SILICON: SURFACE CHARACTERIZATION. . . 65

4.1 Introduction. 65

4.2 Experimental procedure. 69

4.3 Results and discussion. 71

4.3.1 Fluorocarbon film characteristics. 71

4.3.2 Ultrashallow, chemical species depth-profiling. 86

4.3.3 Surface Fermi level pinning and damage removal. 95

4.4 Conclusions. 104

References. 106

CHAPTER 5. SURFACE REACTIONS INDUCED BY

F^+ ION BOMBARDMENT. 109

5.1 Introduction. 109
5.2 Experimental Procedure. 112
5.3 Results and Discussion. 114
5.3.1 Effect of ion dose at 100eV. 114
5.3.2 Effect of ion kinetic energy at $3x10^{16}/cm^2$. 126
5.3.3 Effect of vacuum heating to 800°C. 140
5.4 Conclusions. 143
References. 144
CHAPTER 6. SURFACE REACTIONS INDUCED BY
CF^+ ION BOMBARDMENT. 149
6.1 Introduction. 149
6.2 Experimental procedure. 152
6.3 Results and discussion. 153
6.3.1 Effect of CF^+ ion kinetic energy. 153
6.3.2 Structure of residual damage layer at 100eV. 176
6.4 Conclusions. 187
References. 188
CHAPTER 7. SURFACE REACTIONS INDUCED BY
Cl^+ ION BOMBARDMENT. 190
7.1 Introduction. 190
7.2 Experimental procedure. 193
7.3 Results and discussion. 194
7.3.1 Surface oxidation induced by 1eV Cl^+ ions. 194
7.3.2 Effect of ion kinetic energy at $3x10^{16}/cm^2$ dose. 199
7.3.3 Effect of ion fluence at 100eV and 40eV. 207
7.4 Conclusions. 223
References. 224
CHAPTER 8. GENERAL SUMMARY. 227
8.1 Conclusions. 227
8.2 Future recommendations. 229

VITA 231

LIST OF TABLES

Page

Table 2.1 Properties of silicon and silicon dioxide formed under dry oxidation conditions at 300K. 3

Table 3.1 Surface compositions of elements present after wet HF etching of silicon and list of sensitivity factors used in the quantification of surface elements. 59

Table 4.1 Surface compositions of Si after reactive ion etching in a CHF_3/O_2 plasma at various XPS polar angles corresponding to different sampling depths. 74

Table 4.2 Assignment of core-level binding energies for C1s, Si2p, O1s. and F1s. 81

LIST OF FIGURES

Page

Figure 2.1 Simple schematic drawings through the various steps of a photolithographic process using a positive resist . . 5

Figure 2.2 Schematic drawings of the different dry etching processes . 10

Figure 3.1 Schematic of the (a) UHV system incorporating the low energy ion beam (LEIB) system and vacuum transfer chambers, and (b) the ion optics used in the LEIB system. 23

Figure 3.2 Mass spectra of the ion beam generated from the Colutron ion source using a CF_4 feedgas, (a) all species present before mass separation by the Wien filter, and (b) mass 31 corresponding to CF^+ ions after mass discrimination. 31

Figure 3.3 Simple schematic energy level diagram illustrating the photelectric effect. 36

Figure 3.4 Examples of XPS spectra as (a) survey scan of Si surface after wet HF etch, and (b) high-resolution scan of the Si2p core-level of an Si surface with a thin SiO_2 native oxide overlayer . . . 39

Figure 3.5 The "universal curve" dependence of IMFP on electron kinetic energy (due to Seah and Dench [3.27]). . . . 43

Figure 3.6 Variation in XPS surface analysis depth with changes in the polar

angle of photoelectron detection. 46

Figure 3.7 Schematic drawing of the custom-built UHV system incorporating the SSX-100 XPS spectrometer. 54

Figure 4.1 XPS survey scan of the RIE-processed Si surface. 72

Figure 4.2 Effect of 300μm diameter X-ray beam exposure of the surface contaminants on Si as a function of time (polar angle θ=55°). 76

Figure 4.3 XPS high resolution spectra corresponding to Figure 4.1; (a) C1s spectrum, and (b) Si2p spectrum (see Table 4.2 for actual binding energy positions for the Si-C,O,F species). 78

Figure 4.4 The uniform overlayer model; (a) plot of $\ln([C+O+F]/[Si]+1)$ versus $1/(\lambda \cos\theta)$, the slope corresponding to film thickness was determined by linear regression to be d=4.3nm, and (b) plot of $[C+O+F]/[Si]$ versus polar angle θ, comparison between experimental data and the uniform overlayer model. 84

Figure 4.5 C1s spectra of the fluorocarbon film on Si after ultra-shallow depth-profiling. 87

Figure 4.6 Si2p spectra of the fluorocarbon film on Si after ultra-shallow depth-profiling. 90

Figure 4.7 F1s spectra of the fluorocarbon film on Si after ultra-shallow depth-profiling. 93

Figure 4.8 O1s spectra of the fluorocarbon film on Si after ultra-shallow depth-profiling. 96

Figure 4.9 Change in semiconductor surface potential corresponding to changes in core-level binding energy as measured by surface charge spectroscopy at successive depths of 0.5nm . . . 99

Figure 4.10 Schematic diagram of the model physical structure of silicon surface residual damage induced by fluorocarbon plasma RIE (from Oehrlein and Lee [4.11]), and the information provided from this thesis is shown in the lower diagram. 102

Figure 5.1 XPS surface compostion ratio of F/Si (at a photoemission polar angle of 55° with respect to the sample surface normal) as a function of F^+ ion dose at a constant kinetic energy of 100eV 115

Figure 5.2 XPS high resolution Si2p spectra for p-type Si(100) after 100eV F^+ ion bombardment at doses of $3x10^{14}$, $3x10^{16}$ and $1x10^{17}/cm^2$; (a) spectra scaled and overlayed to the same peak height, and (b) spectra overlayed with each spectrum normalized to total area under each peak profile. 118

Figure 5.3 Effect of ion dose on surface Fermi level position as a result of F^+ ion bombardment at 100eV. 124

Figure 5.4 XPS surface composition ratio of F/Si (at a polar photoemission angle of 55° with respect to the sample surface normal) as a function of F^+ ion kinetic energy with a constant dose of $3x10^{16}/cm^2$ for room temperature bombardment conditions 127

Figure 5.5 High resolution XPS spectra of the Si2p core-level for Si(100) surfaces receiving 20 and 100eV F^+ at $3x10^{16}$ions/cm^2 for room temperature conditions; and the control spectrum represented an unbombarded surface region of the Si(100) sample; (a) spectra scaled and overlayed to the same peak height, and (b) spectra overlayed with each spectrum normalized to total area under each peak profile. 131

Figure 5.6 Variation of (F1s/F2s) peak area ratio with F^+ ion kinetic energy at a constant dose $3x10^{16}/cm^2$ for room temperature conditions. 135

Figure 5.7 Valence band photoemission spectra corresponding to Figure 5.5. . . .138

Figure 5.8 Effect of vacuum heating to 800°C on surface F/Si composion ratio for the ion kinetic energy range of 20 to 100eV at a constant dose of $3x10^{16}/cm^2$. 141

Figure 6.1 Effect of ion kinetic energy on (a) [CF]/[Si] surface composition ratio, (b) estimated fluorocarbon film thickness. 155

Figure 6.2 High resolution C1s core-level spectra of the Si surfaces bombarded by 2eV and 10eV CF^+ ions at a dose of $1x10^{16}/cm^2$. 157

Figure 6.3 High resolution Si2p core-level spectra corresponding to Figure 6.2. .159

Figure 6.4 High resolution C1s core-level spectra of Si surface after 80eV and 100eV CF^+ ion bombardment at a dose of $3x10^{16}/cm^2$. 165

Figure 6.5 High resolution Si2p core-level spectra corresponding to Figure 6.4. .168

Figure 6.6 High resolution F1s core-level spectra of Si surface after 10eV and 100eV CF^+ ion bombardment. 171

Figure 6.7 Valence band photoemission spectra for Si surfaces bombarded by 60eV, 80eV and 100eV CF^+ ions. The valence band spectrum of the wet HF/H_2O etched Si control surface represents the surface before ion beam bombardment. 174

Figure 6.8 High resolution XPS spectra of Si surface after 100eV CF^+ ion bombardment with $3x10^{16}/cm^2$ showing the effects of two different photoemission polar angles of $\theta=0°$ and $\theta=63°$ on (a) C1s core-level spectra, and (b) Si2p core-level spectra. 177

Figure 6.9 Changes in percent area of C1s and Si2p core-level intensities attributed to Si-F and C-Si species as a function of photoemission polar angle, θ corresponding to Figure 6.8. Included in the Figure is the approximate sampling depth axis. .180

Figure 6.10 Normalized concentration depth-profile for Si-containing species calculated with the B-H algorithm using the data from Figure 6.9 IMFP was constant at 3nm. 182

Figure 6.11 Valence photoemission spectra of Si surface after 100eV CF^+ ion bombardment with dose of $3x10^{16}/cm^2$ at various photoemission polar angles. The control surface was the same as that described for Figure 6.7. 185

Figure 7.1 High resolution XPS spectra of (a) Cl2p and, (b) Si2p core-levels

for Si surface receiving 1eV Cl^+ ion bombardment with a dose of $3x10^{16}/cm^2$. The control surface was for the same sample wet etched in aqueous HF solution before ion beam exposure. 195

Figure 7.2 High resolution XPS spectra of (a) Cl2p and, (b) Si2p core-levels for Si surface receiving 20eV Cl^+ ion bombardment with a dose of $3x10^{16}/cm^2$. The control surface was for the same sample wet etched in aqueous HF solution before ion beam exposure. 200

Figure 7.3 XPS surface composition ratio of Cl/Si (at a polar photoemission angle of 55° with respect to the sample surface normal) as a function Cl^+ ion kinetic energy. 205

Figure 7.4 XPS surface composition ratio of Cl/Si (at a photoemission polar angle of 55° with respect to the sample surface normal) as a function Cl^+ ion dose at (a) K.E.=100eV, and (b) K.E.=40eV. 208

Figure 7.5 XPS high resolution spectra of the Cl2p core-level for Cl^+ ion bombardment at 100eV showing the effects of ion dose at $3x10^{15}$ and $1.5x10^{18}/cm^2$. 212

Figure 7.6 XPS high resolution spectra of the Cl2p core-level for Cl^+ ion bombardment at 40eV showing the effects of ion dose at $3x10^{15}$ and $1x10^{18}/cm^2$. 214

Figure 7.7 XPS high resolution spectra of the Si2p core-level for Cl^+ ion bombardment at 40eV showing the effects of ion dose at $3x10^{15}$ and $1x10^{18}/cm^2$. 217

Figure 7.8 Effect of ion dose on surface Fermi level position as a result of Cl^+ ion bombardment at (a) 100eV, and (b) 40eV. 220

The author of this thesis has granted The University of Western Ontario a non-exclusive license to reproduce and distribute copies of this thesis to users of Western Libraries. Copyright remains with the author.

Electronic theses and dissertations available in The University of Western Ontario's institutional repository (Scholarship@Western) are solely for the purpose of private study and research. They may not be copied or reproduced, except as permitted by copyright laws, without written authority of the copyright owner. Any commercial use or publication is strictly prohibited.

The original copyright license attesting to these terms and signed by the author of this thesis may be found in the original print version of the thesis, held by Western Libraries.

The thesis approval page signed by the examining committee may also be found in the original print version of the thesis held in Western Libraries.

Please contact Western Libraries for further information:
E-mail: libadmin@uwo.ca
Telephone: (519) 661-2111 Ext. 84796
Web site: http://www.lib.uwo.ca/

CHAPTER 1.

INTRODUCTION

1.1 Objectives of the thesis

The purpose of this thesis was to investigate the surface reactions induced by reactive ion bombardment of p-type Si(100) as it applies to dry etching in microelectronics fabrication. The residual surface damage was investigated by surface analysis using X-ray photoelectron spectroscopy. The development of ancilliary techniques centred about XPS was also investigated.

1.2 Scope of the investigation

The residual surface damage of p-type Si(100) induced by a conventional plasma reactive ion etching (RIE) system is investigated as a model system. The residual surface damage induced by mass-purified reactive ion beams is used to simulate the effects of different energetic reactive ions impinging onto the silicon surface. The reactive positive ions of interest are F^+, CF^+, and Cl^+ because these ions are employed in present generation dry etching schemes. The ion energy range studied is 1 to 100eV because these ion energies have not been investigated for these reactive ions of interest, and also because this energy range is prevalent in present dry etching systems.

CHAPTER 2.

GENERAL REVIEW

2.1 Semiconductor silicon

2.1.1 Material properties

Semiconductor silicon (Si) material is the dominant industrial material used in the fabrication of integrated-ciruit (IC) devices today. The emergence of this material is due to a number of advantages [2.1] in microelectronics fabrication. Silicon can be readily oxidized to form silicon dioxide (SiO_2). This latter dielectric material possesses high-quality electrical insulation as well as desirable interfacial electrical properties with Si [2.2], and is an effective diffusion barrier for the selective diffusion steps involved in IC fabrication. Si is a natural, abundant element and thus provides a low-cost starting material. This semiconductor material can be produced on a commercial scale as single crystals with very high purity (up to one electrically active impurity for every 10^9 silicon atoms [2.3]). This high-purity starting material can be processed by the controlled introduction of impurity atoms or dopants to affect desirable semiconducting properties The prevalence of computers and information processing is a direct consequence of the widespread availability of silicon IC chip technology [2.3]

Table 2.1 lists some of the properties of semiconducting silicon Silicon is a Group IV element in the Periodic Table. In terms of bonding, the Si atoms in the solid may be thought of as having 10 inner, closed-shell electrons which are transparent to bonding, and 4 outer electrons (valence electrons) which do participate in covalent

Table 2.1 Properties of silicon and silicon dioxide formed under dry oxidation conditions at 300K.

Properties	Silicon	Silicon dioxide
bandgap	1.12eV	~ 9eV
structure	diamond	amorphous
lattice constant	0.543nm	_____
density	2.33g/cm^3	2.27g/cm^3
atoms/cm^3, molecules/cm^3	5.0x10^{22}	2.27x10^{22}
relative dielectric constant	11.9	3.9
thermal conductivity	1.48W/cm.K	0.014W/cm.K
drift mobility of electrons	1500cm^2/V.s	_____
drift mobility of holes	450cm^2/V.s	_____

from J.W. Mayer, S.S. Lau, Electronic Materials Science: For Integrated Circuits in Si and GaAs, Macmillan Publishing, New York, 1990.

bonding. These covalent bonds are directional which results in a symmetric, tetrahedral configuration giving rise to the diamond crystal lattice structure These covalent bonds between atoms mean that there are very few free electrons available for charge transport as in the case of metals such as copper or aluminum. The semiconductor Si has an indirect bandgap of appoximately 1.1eV, and if energy greater than this bandgap energy is supplied to a sample, then these covalent bonds are broken and the liberated electrons move within the crystal. Additionally, the absent site originally occupied by the electron can be thought of as an effective positively charged particle called a hole Both the electrons and holes can transport charge leading to a current. The conductivity (due to electron-hole current) of pure Si lies between that of metallic conductors and insulators, hence the name "semiconductor".

2.1.2 Microelectronic device fabrication

The Si semiconductor material is used to fabricate microelectronic devices The device physics is described in the literature (for example reference [2 4]) The fabrication processes include [2.1,3,5]: the oxidation and doping of Si, the deposition of insulating films and the development of interconnects and contacts. These processes are dependent on lithography [2.1]- the transfer of patterns of windows to the Si wafer surface in the form of masks. The various steps involved in a simple photolithographic process are shown in Figure 2.1. The removal of material (selectively or non-selectively) is achieved by wet and dry etching processes. The wet etching process uses a liquid chemical solution/agent and is applied to the non-selective removal of a film material [2 1,3,5] The dry etching process is used to achieve selective and directional (anisotropic) erosion

Figure 2 1 Simple schematic drawings through the various steps of a photolithographic process using a positive resist. Monochromatic light illuminates the mask and specific areas are shadowed. The light-exposed resist is altered and is removed. The remaining patterns of unexposed resist protect regions of silicon dioxide from subsequent dry etching (section 2.2). The dry etching process removes the oxide only in desired areas to expose the underlying silicon.

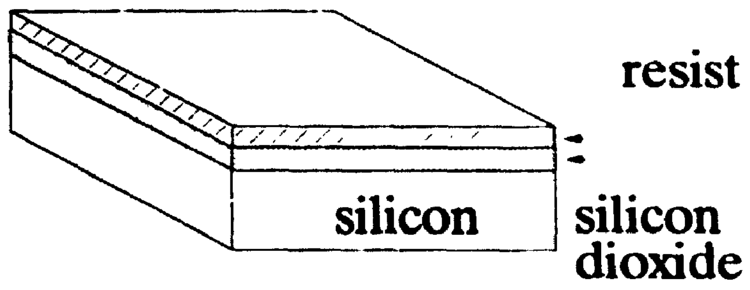
resist
silicon
silicon
dioxide

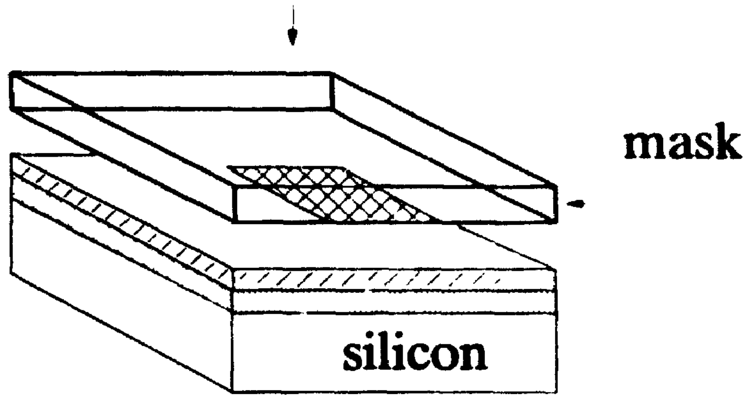
mask
silicon

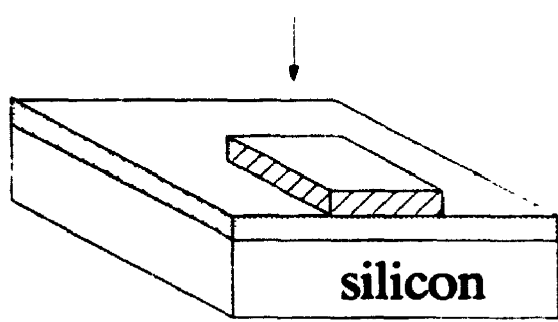
silicon

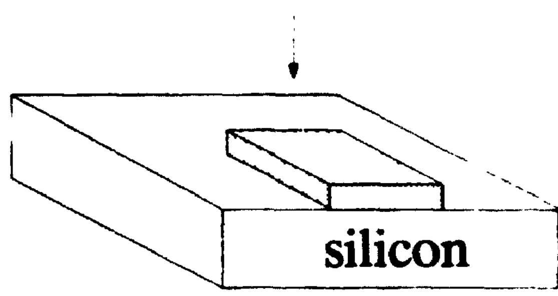
silicon

of a material and is discussed further in the next section.

2.2 Dry etching processes

The term "dry etching" refers to the removal of material such as silicon via gas phase etch species. Gaseous reactant particles (in the form of either ions, atoms or molecules) impinge onto the surface of the material being etched and yield these species. The etch species can also be in the form of atoms, molecular fragments or reaction products In some critical cases, the dry etching is required to be selective and anisotropic Selectivity means that the etching is capable of removing different material at different etch rates and is conventionally quantified as a ratio of etch rates between two materials For example, the selectivity of SiO_2:Si > 4 corresponds to the selective removal of SiO_2 over Si wherein the dry etching rate ratio of the SiO_2 to Si is greater than four. In this example, the selectivity is important for removing the oxide to expose the underlying Si for subsequent electrical contact with a metal layer. Anisotropic etching is required to produce vertical profiles (see Figure 2.1) in order to maintain the fidelity of the pattern transfer from the lithographic process. If the dry etching process was isotropic, then undercutting below the photoresist would cause the degradation of pattern transfer Also, neighbouring regions which are isolated by the vertical etch profiles could possibly come into electrical contact causing shortcircuiting. The degree of selectivity and anisotropy is attained by the type of dry etching employed The classification of the particular dry etching methods due to Fonash [2.6] is adopted in this thesis, and is described below

2.2.1 Physical etching

This dry etching technique involves energetic ion bombardment (at energies of a few keV) of the material. The physical sputtering process is derived from the momentum transfer from the incident ion bombardment to the target surface atoms resulting in disruption of the crystal surface, bond breaking, and dissipation of kinetic energies in the collisional cascades [2.7] by the ejection of surface atoms and molecular fragements In the fabrication process, physical sputtering is accomplied by using a chemically inert gas to form a plasma, and the etching chamber is configured to direct energetic inert ions onto the surface of the material being etched. This process is anisotropic because the ions can be accelerated to the target surface by biasing the sample electrode and consequently etching is by a line-of-sight direction. Although the etching rate is dependent on the material, the selectivity is poor compared to the other sputtering techniques

2.2.2 Chemical etching

This mechanism occurs via a surface chemical reaction to produce volatile etch products which are pumped away by the vacuum system. Chemical etching as discussed with respect to dry etching is a very selective process Chemical etching occurs via a sequence of steps, any number of which may be rate-controlling

(a) gaseous etchant species arrive at and diffuse about the surface of material to be etched,

(b) reactions with the surface takes place to form products incorporating the material being etched;

(c) these reaction products are volatile and desorb from the surface,

(d) the desorbed species are pumped away by the vacuum system.

By choosing the appropriate etching gas to be very reactive with one material while relatively inert to another material, high selectivity is produced. However, this mechanism is non-directional (i.e. isotropic) and undercutting of resist masks occurs. In some very special cases, chemical etching may give rise to crystallographic etching, but this is not considered prevalent in IC fabrication. This chemical etching process is therefore generally isotropic, but very selective, and is achieved without energetic ion bombardment as in the situation of physical etching.

2.2.3 Physico-chemical etching

The synergistic effects of physical and chemical etching are described by this etching process with consequences of selective and anisotropic etching at etch rates greater than the combined isolated physical and chemical etching rates [2.8]. Physico-chemical etching encompasses the cases of energetic inert ion bombardment of the material in the presence of an etching gas flux, energetic reactive ion bombardment of materials, and of energetic reactive ion bombardment plus reactive neutral etching gas flux to etch a material surface. Figure 2.2 shows simple schematic drawings depicting the different dry etching classifications. In general, this third dry etching technique has been proposed to be caused by:

(i) chemically-enhanced physical sputtering (i.e. chemically weakened surface bonds facilitate physical sputtering [2.9]);

(ii) damage-enhanced chemical reactions leading to volatile products [2.10,11];

Figure 2.2 Schematic drawings of the different dry etching processes

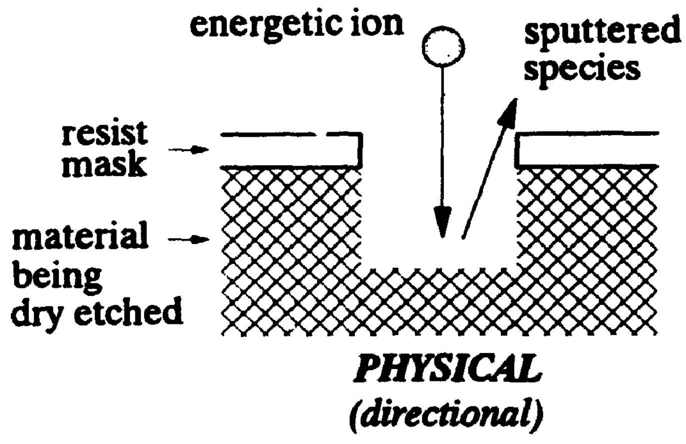

PHYSICAL
(directional)

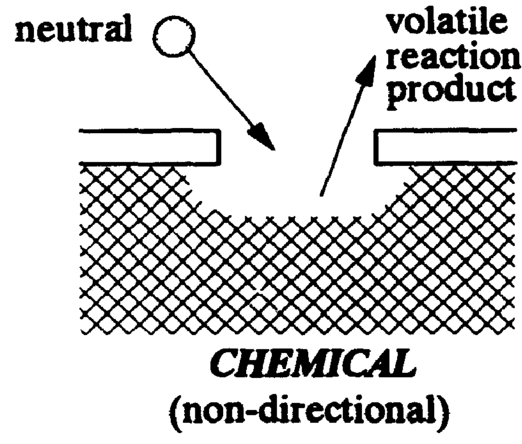

CHEMICAL
(non-directional)

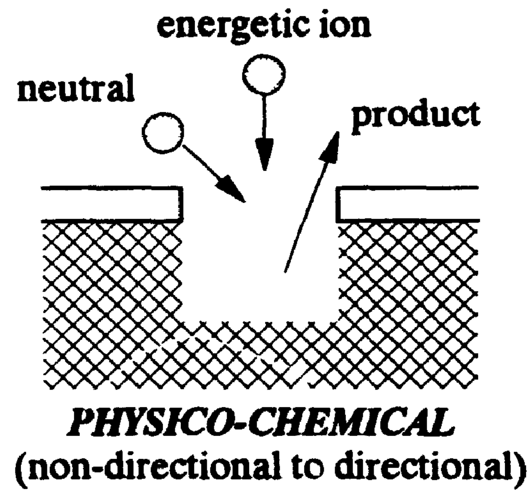

PHYSICO-CHEMICAL
(non-directional to directional)

(iii) chemical sputtering (i.e. ion bombardment provides the energy to drive the chemcial reactions leading to desorption of volatile species [2.12]).

A significant number of fundamental and applied studies have been carried out to determine the actual mechanism(s) which gives the enhanced etch rates from physico-chemical etching, but much controversy still exists in the scientific community. For an excellent recent review, the reader is directed to the work of Winters and Coburn [2.8].

In commercial environments the physico-chemical etching is accomplished by generating reactive ions, free radicals and neutrals in a reactive plasma, and directing the etching species at normal incidence onto target sample wafers. The various types of dry etching chamber configurations have been reported in the literature [2.6]. The term "reactive ion etching" (RIE) has been applied to one particular dry etching configuration [2.6] where it implies that the reactive positive ions are mainly responsible for etching. However, the presence of a significant neutral reactive flux has been associated [2.6] with the enhanced etch rates. This RIE process is a dominant dry etch technique in the fabrication process because it provides high etch rates, selectivity and anisotropy.

2.3 Reactive Ion Etching of Silicon

2.3.1 Plasma chemistry

In present generation RIE, fluorocarbon feedgases such as CF_4, C_3F_8, and CHF_3 are used to generate the reactive species needed to achieve etching of Si as well as SiO_2. A CF_4 plasma produces fluorine (F) atoms, and these atoms react with Si to form

primarily SiF_4 at room temperature. The etching of Si by fluorine has been extensively studied [2.8]. The addition of oxygen (O_2) and hydrogen (H_2) to these fluorocarbon gases allows the selectivity to be varied. CF_4 + H_2 RIE gives SiO_2:Si selectivity of 35:1 [2.13], and an increase in H_2 additions produces an increase in selectivity [2.14]. This increased selectivity is attributed to the decrease in the Si etch rate as a result of the development of a fluorcarbon film residue on the silicon surface. This example serves to illustrate the importance of the plasma chemistry in RIE. For an in-depth presentation of various plasma chemistries related to silicon RIE, the reader is referred to the literature [2.15,16].

2.3.2 Residual surface damage

The reactive ion etching process induces surface residual damage because energetic ions are involved. These reactive positive ions deliver energies of a few hundreds of electronvolts (as determined by the self-bias voltage in the RIE configuration) to the surface of the material being dry etched. Such ion bombardment results to varying degrees in physical damage to the Si crystalline surface, surface region contamination from the implantation of atoms from the RIE plasma, and the formation of Si-containing surface compounds. These various effects from reactive ion bombardment are manifested as modified structural, chemical and electrical properties [2.17]. All these different surface modifications will be collectively referred to as residual surface damage in this thesis

The surface physical damage up to 30nm is seen by transmission electron microscopy as extended defects, {111} planar defects, gas bubbles and an amorphized surface region[2.18,19]. X-ray double-crystal diffraction also confirms the presence of

this amorphous and/or polycrystalline silicon surface region [2.20] to depths of 20nm Thermal wave measurements also indicate the presence of disorder and defects to a sampling depth of 3μm [2.21]. The amorphized very surface region is a direct consequence of the energetic ion bombardment and the defects present below the surface are due to permeation of atoms [2.17] which are implanted from the plasma as well as from enhanced diffusion driven by non-equilibrium point-defect densities [2.22]

The consequences of the residual surface damage are usually detrimental to devices fabricated on such surfaces. CF_4 RIE of boron-doped silicon results in boron acceptor neutralization to depths of the order of microns below the Si surface [2.23] The presence of hydrogen from CF_4/H_2 feedgas mixtures also results in hydrogen incorporation or permeation [2.24]. This hydrogen is known to form hydrogen-boron-silicon complexes which deactivate the dopant [2.25]. Anomalous high contact resistance to the p+ silicon surface after RIE has been observed [2.21]. A correlation is reported [2.19] between the Si surface lattice damage and leakage current properties of thermal oxides grown on the damaged silicon. Capacitance-voltage (C-V) measurements indicate inferior high- and low-frequency curves compared to a surface not subjected to CF_4 RIE [2.26] In addition, interface trap states are uniformly distributed throughout the bandgap with net trap densities fivefold greater than for an unetched Si surface [2.26] RIE of silicon in a NF_3 plasma results in a net positive surface charge which leads to an increase in Schottky barrier height on p-type Si and a decrease on n-type Si [2.27]

The fluorocarbon RIE process is known [2.22,28,29] to leave a residual passivation layer containing mainly carbon (C) and fluorine (F). Several analytical techniques [2.22,30-32] have been employed to study the residue film composition and crystalline

damage including Rutherford backscattering spectrometry/ion channelling (RBS/channelling), nuclear reaction analysis (NRA), X-ray photoelectron spectroscopy (XPS), and spectroscopic ellipsometry (SE). The conclusions from these studies are that the fluorocarbon residue film layer caps a modified Si-containing compound layer of oxides, carbides and oxyfluoride species extending to depths of 3nm with a deeper (30nm) region of hydrogen penetration and crystalline damage. Hence the residual surface damage induced by fluorocarbon RIE of silicon is manifested as a complex, Si-modified surface region comprised of carbon, fluorine, oxygen, and hydrogen contaminants in the forms of a residue layer, a compound layer which is also heavily damaged, and a permeated or diffused region which also possesses crystalline disorder.

As a result of exposing Si to the reactive plasma environment in RIE, reactive ions and neutrals all simultaneously irradiate the silicon surface to be dry etched. It is therefore difficult to assign the contributions of the various reactive species to the development of the residual damaged surface region. A valuable parameter to control is the reactive species kinetic energy [2.33]. The effects of ion bombardment energy from RIE of silicon using CF_4 and SF_6 feedgases have been shown [2.34] to affect the extent of residual damage in the form of fluorosilyl (SiF_n, n=1,2,34) species formation. However, the precise kinetic energy of the reactive ions was not determined. The presence of reactive neutrals in the plasma at vacuum pressures of milli-Torr means that the energetic ions collide with these neutral species and thus lose energy [2.30,35]. Hence the energies of reactive species (both reactive ions and neutrals) range from a few hundreds of electronvolts down to almost zero energy. In order to gain a fundamental understanding of the development of residual surface damage, the independent control of

the different reactive ions as well as the kinetic energy is required.

2.3.3 Future trends

A recent review [2.36] has stated that dry processing in microelectronics will be moving towards low pressure plasma technology. With linewidths being reduced to below 0.35μm, the maintenance of vertical trench profiles becomes more difficult if the energetic ions lose their directionality from collisions with neutral species from the plasma. Hence, by reducing the plasma pressure, less neutrals are present with a concomitant increase in ion current density arriving at the sample surface. This situation has been called [2.37] high density plasma (HDP) etching. In this low pressure situation, the reactive ions will actually be dominant in the etching process, and true reactive ion etching takes place.

The reactive ion energies in the HDP are lower than for conventional RIE, i.e. 25 to 70eV [2.36,37] compared to a few hundreds of electronvolts. This produces less severe residual surface damage after the dry etching, and the etching chemistry is different [2.36] at the lower ion energies. At these energies the chemistries of the ion-solid interactions involved in the dry etching process are likely dominated by the ion energy. This reactive ion kinetic energy regime of 100 to 20eV is of fundamental as well as technological importance to the study of residual surface damage on silicon.

REFERENCES

2.1 R.C. Jaeger, in Introduction to Microelectronic Fabrication, Modular Series on Solid State Devices, Vol. 5, edited by G.W Reading, 1988.

2.2 L.G. Meiners, H.H. Wieder, Mater. Sci. Rep., 3, 139, 1988.

2.3 J W. Mayer, S.S. Lau, Electronic Materials Science: For Integrated Circuits in Si and GaAs, Macmillan Publishing, New York, 1990.

2.4 S.M. Sze, Physics of Semiconductor Devices, McGraw-Hill, New York, 1981.

2.5 S.K. Ghandhi, VLSI Fabrication Principles, J. Wiley & Sons, New York, 1983.

2.6 S.J Fonash, Solid State Technol., 28(1), 150, 1985.

2.7 R. Behrisch, in Sputtering by Particle Bombardment II, Topics in Applied Physics, Vol. 52, edited by R. Behrisch, Springer-Verlag, Berlin, 1983.

2.8 H.F. Winters, J.W. Coburn, Surf. Sci. Rep., 14, 161, 1992; and references therein.

2.9 J.L. Mauer, J.S. Logan, L.B. Zielinski, G.S. Schwarts, J. Vac. Sci. Technol., 15, 1734, 1978.

2.10 J W. Coburn, H.F. Winters, J. Appl. Phys., 50, 3189. 1979.

2.11 D.L. Flamm, V.M. Donnelly, Plasma Chem. Plasma Process., Vol. 1, 317, 1981.

2.12 Y Y. Tu, T.J. Chuang, H.F. Winters, Phys. Rev. B, 23, 823, 1981.

2.13 L.M. Ephrath, J. Electrochem. Soc., 126, 1419, 1979.

2.14 R.A.H. Heinecke, Solid-State Electon., 18, 1146, 1975.

2.15 J W Coburn, Plasma Etching and Reactive Ion Etching, American Vacuum

Society Monograph Series, edited by N.R. Whetten, American Institute of Physics, New York, 1982.

2.16 G.S. Oehrlein, in Handbook of Plasma Processing Technology Fundamentals, Etching, Deposition, and Surface Interactions, edited by S M Rossnagel, J.J. Cuomo, W.D. Westwood, Noyes Publications, New Jersey, 1989.

2.17 S.J. Fonash, Solid State Technol., 28(4), 201, 1985.

2.18 S.J. Jeng, G.S. Oehrlein, G.J. Scilla, Appl. Phys. Lett., 53(18), 1735, 1988

2.19 I.W.H Connick, A. Bhattacharyya, K.N. Ritz, W.L. Smith, J. Appl Phys., 64(4), 2059, 1988.

2.20 M. Nemiroff, M. Stuber, R. Troutt, D. Gerber, S. Mittal, J Appl Phys., 62(9), 3677, 1987.

2.21 H. Nordstrom, G. Kittlesen, P. Wiklund, M. Ostling, E. Niemi, Vacuum, 38, 801, 1988.

2.22 G.S. Oehrlein, R.M. Tromp, Y.H. Lee, E.J. Petrillo, Appl. Phys Lett, 45, 420, 1984

2.23 X.C. Mu, S.J. Fonash, R. Singh, Appl. Phys. Lett., 49(2), 67, 1986

2.24 X.C. Mu, S.J. Fonash, A. Rohatgi, J. Rieger, Appl. Phys Lett, 48(17), 1147, 1986.

2.25 L.J. Huang, W.M Lau, J. Vac. Sci. Technol., A10(4), 812, 1992

2.26 F.Y. Chen, Lin I, J. Appl. Phys., 64(3), 1589, 1988

2.27 S. Ashok, T.P. Chow, B.J Baliga, Appl. Phys Lett, 42(8), 687, 1983

2.28 J W. Coburn, J. Appl. Phys., 50, 5210, 1979.

2.29 D.J Vitkavage, T.M Mayer, J. Vac. Sci. Technol, B4(6), 1283, 1986

2.30 G.S Oehrlein, R.M. Tromp, J.C. Tsang, Y.H. Lee, E.J. Petrillo, J Electrochem. Soc., 132, 1441, 1985.

2.31 G.J. Coyle, G.S. Oehrlein, Appl. Phys. Lett., 47, 604, 1985.

2.32 Y.H. Lee, G S. Oehrlein, C. Ransom, Rad. Effect. Def. Sol., 111/112, 221, 1989.

2.33 D. Bollinger, S. Ida, O. Matsumoto, Solid State Technol., 27(6), 167, 1984.

2.34 G.S Oehrlein, J. Vac. Sci. Technol., A11(1), 34, 1993.

2.35 K Kohler, J.W. Coburn, D.E. Horne, E. Kay, J.H. Keller, J. Appl. Phys., 57, 59, 1985.

2.36 M. Pichot, Vacuum, 41, 895, 1990.

2.37 J W Coburn, Plasma Etching and RIE, AVS Short Course Lecture Notes, 1992.

CHAPTER 3.

INSTRUMENTAL METHODS

3.1 Introduction

In this chapter, the instrumental aspects of the methods used in this thesis are reviewed. The level of detail in each section reflects the background information needed to understand the experimental results. Detailed theoretical development of the instruments is considered beyond the scope of this work Such developments are cited in the various sections for further reading.

3.2 Sample preparation

The silicon (Si) samples used in this thesis were prepared from device quality p-type Si(100) wafers implanted with boron (B) at 16keV and dose of 1 $6\times10^{15}/cm^2$ followed by rapid thermal annealling at 1050°C for 30s. The samples are wet etched in a dilute hydrofluoric acid (HF) and deionized water solution (approximately 5vol % HF) for 30s followed by rinsing in deionized water for 30 to 45s, and blown dry with a nitrogen gas (N_2) for 60s before loading into the UHV-LEIB system (see section 3 4 for a description of the system) This wet HF etch treatment produces a hydrogen-terminated Si surface which is resistant to air oxidation[3 1,2] over the time period (approximately 1min) needed to load the sample into the LEIB system No further surface cleaning procedure is applied prior to or after the ion beam bombardment experiments

3.3 Ultra-high vacuum considerations

The surface reactions induced by reactive ion bombardment of silicon are conducted as experiments under vacuum conditions. This vacuum requirement is needed to ensure that surface contamination does not drastically affect the studies, that the reactive ion species can be delivered to the target surface and electrons can be detected by an analyzer without being significantly scattered by gas phase molecules. In many cases, surface contamination can seriously alter the interpretation of analytical results. The principle source of contamination is from the residual gas present in the vacuum system [3.3]

Gas phase kinetic theory predicts that for a sticking probability of unity, i.e. every gas molecule that impinges onto a surface will stay on that surface, a background pressure of 1×10^{-6}mbar (1mbar=1Torr) causes an accumulation of 1 monolayer of contaminant in 1s at room temperature [3.4] If an arbitrary acceptable limit on rate of contamination is chosen to be less than 1monolayer in 30min, then gas kinetic theory says that the pressure must be no greater than 5×10^{-10}Torr. At room temperature the sticking probabilities are usually less than unity, and most experiments can be conducted with base pressures of the order of 10^{-8} to 10^{-10}Torr This pressure regime is typically called ultra-high vacuum (UHV)

For the experiments conducted in this thesis, the low energy ion beam system is typically at pressures below 5×10^{-9}Torr, and the XPS surface analysis system is at pressures below 6×10^{-9}Torr

3.4 Generation of low energy, mass-filtered ion beams

3.4.1 The custom-built, low energy ion beam system

The design of the low energy ion beam (LEIB) system was such that ions were extracted, accelerated and transported at energies of a few keV from the ion source, through a mass-filter system, and finally decelerated through an electrostatic lens system before bombardment onto the sample surface. Increase of the ion beam diameter due to space charge repulsion during ion beam transportation has been identified as a serious problem in low energy ion beam systems [3.5]. This ion beam spreading can significantly reduce both the available ion current due to current losses in the ion beam column and the current density at the specimen surface. The design philosophy of high ion energy transportation through the column and then final ion deceleration minimizes these beam spreading effects.

The custom-designed and constructed LEIB system incorporates a slight modification of the Colutron G-2 Ion Gun model [3.6]. Figure 3.1 shows a general schematic of the low energy ion beam system and vacuum transfer chambers. The LEIB system consists of the ion source which generates the reactive, positive ions and neutrals in a small volume plasma. These species are extracted through a small, approximately 1mm diameter hole in the anode (see Figure 3.1b). After being focussed by Einzel lenses in the extraction-focussing chamber, the ion beam is mass-separated using a Wien filter. An "elbow" in the ion beam column is used to separate neutral species from the positive ions in the beam. Electrostatic deflection plates (1st Horizontal Deflector in Figure 3.1b)

Figure 3.1 Schematic of the (a) UHV system incorporating the low energy ion beam (LEIB) system and vacuum transfer chambers, and (b) the ion optics used in the mass-resolved LEIB unit from (a).

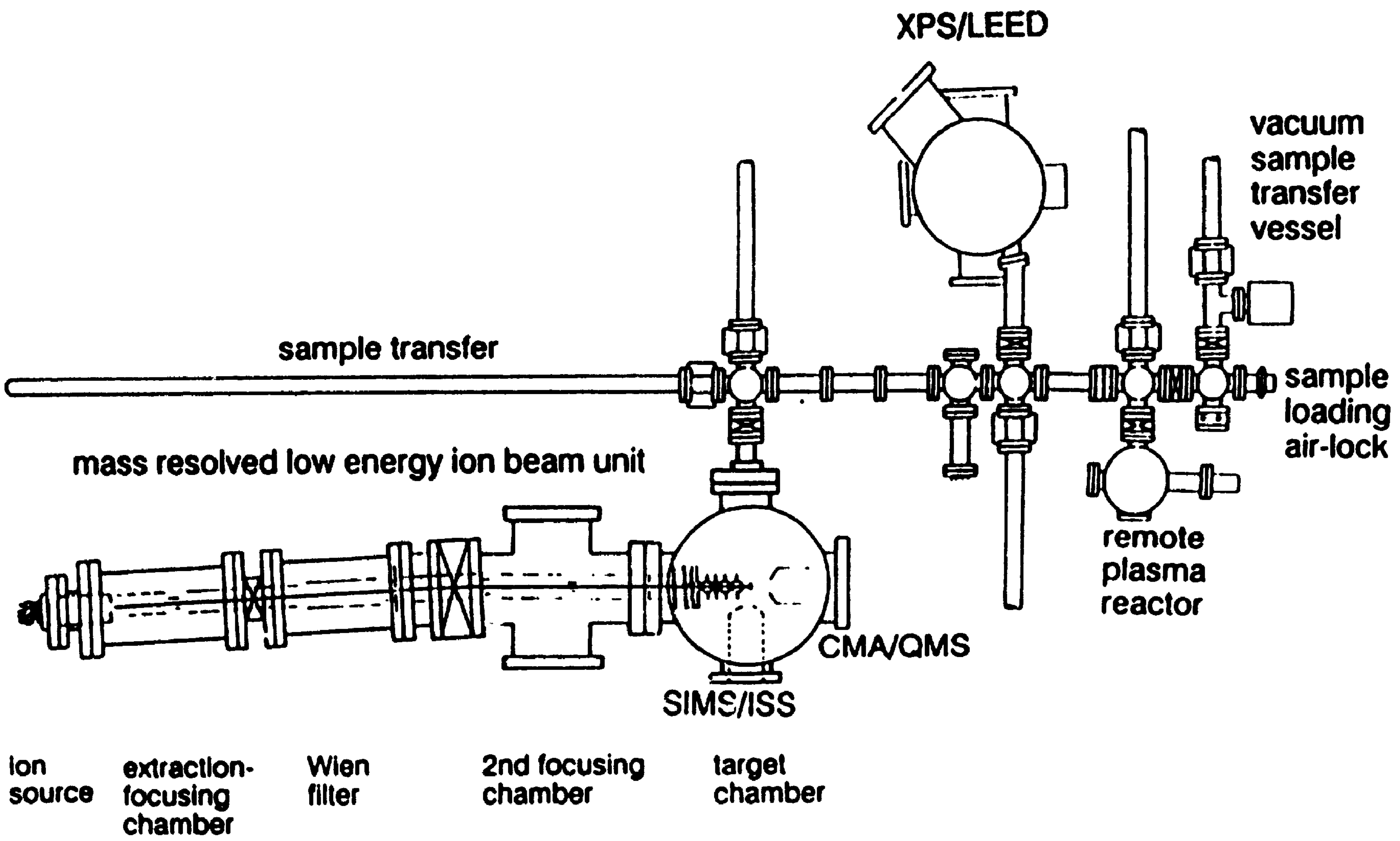
XPS/LEED
vacuum sample transfer vessel
sample transfer
sample loading air-lock
mass resolved low energy ion beam unit
remote plasma reactor
CMA/QMS
SIMS/ISS
ion source
extraction-focusing chamber
Wien filter
2nd focusing chamber
target chamber

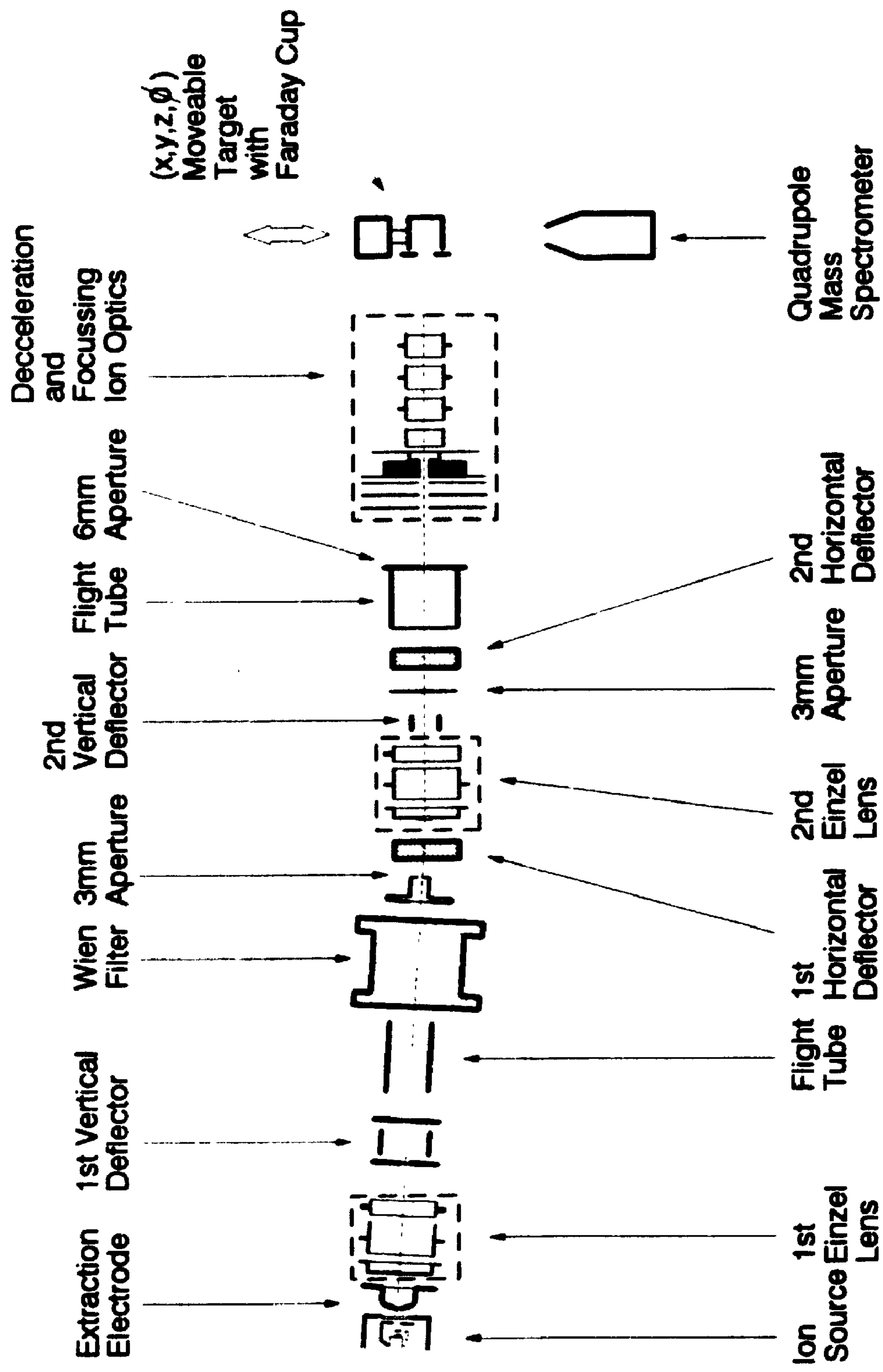

Ion Source
Extraction Electrode
1st Einzel Lens
1st Vertical Deflector
Flight Tube
Wien Filter
3mm Aperture
1st Horizontal Deflector
2nd Einzel Lens
2nd Vertical Deflector
3mm Aperture
2nd Horizontal Deflector
Flight Tube
6mm Aperture
Decceleration and Focussing Ion Optics
Quadrupole Mass Spectrometer
(x,y,z,ϕ) Moveable Target with Faraday Cup

are used to direct the ion beam through to a 2nd Einzel lens. The neutrals species are not influenced by the electrostatic field, so are separated from the ions at the "elbow". Finally, the mass-filtered ion beam is focussed and decelerated by a series of electrostatic lenses (Deceleration and Focussing Ion Optics from Figure 3.1b). The final filtered and focussed ion beam impinges onto either a Faraday cup or the sample.

For the LEIB system in Figure 3.1a, vacuum conditions are maintained by a turbomolecular pump backed by a rotary pump for the ion source chamber, the extraction-focussing chamber, and the chamber housing the Wien filter. The typical operating pressures are near 1×10^{-5}Torr with the ion source chamber at $3\text{-}5\times10^{-2}$Torr. The second ion beam focussing chamber and the target/specimen chamber are each separately pumped by cryopumps with routine base pressures of 1×10^{-9} Torr. The ion beam is blocked from impinging onto the sample or Faraday cup by a gate valve separating the Wien filter chamber and the second focussing chamber. During ion beam bombardment of the sample, the pressure in the target chamber rises to a limit of 5×10^{-9}Torr.

3.4.2 Ion source

The type of ion source for any ion beam system is very important. For research environments, the ion source should be capable of generating the ion species of interest, the kinetic energy spread of the ions should be 10eV or less, and ion current densities of at least a few microamperes per square centimetre should be achievable. Other considerations include cost of maintenance and operation of this component.

The most widely used type of ion source is the hot-cathode source [3.7]. The basic principle of operation involves heating a tungsten cathode within an ionization

chamber When a potential is applied between the cathode and anode, a region of space-charge-limit potential is developed. Thermionic emission of electrons [3.3,4] occurs at the hot cathode. These energetic electrons are accelerated towards the anode and collide with the feedgas present in the space-charge-limit potential region. As a consequence of gas phase collisions between the electrons and feedgas atoms, ions and secondary electrons are generated. As more gas particles collide and are ionized, a cloud of ions and electrons is produced (i.e. a plasma is formed). The ions will tend to move towards the cathode and electrons will tend to move from the cathode to the plasma [3.8]. If this condition is self-sustaining, the plasma is maintained.

The positive ions are extracted axially from the plasma through a circular aperture at the centre of the anode plate (see Figure 3.1b). The hollow cathode housing the tungsten filament is placed axially in the ion source. The high electron density from the thermionic emission process optimizes the ionization of the feedgas. The Colutron hot-filament dc ion source operates at a power of approximately 500W. Current densities of near 150μA/cm^2 for Ar^+ have been obtained for this ion source. For the reactive ion species used in this thesis, the current density ranged from 1 to 100μA/cm^2.

3.4.3 Beam focussing

The ions extracted from the plasma are accelerated to a potential of 3keV by an extraction plate electrode (see Figure 3.1b). This extracted ion beam is of very high current density and is also defocussed. Focussing and collimation of the beam is carried out by an Einzel lens located at the exit point of the extraction plate. The kinetic energy of ion species in the beam entering and leaving the lens are the same. The

focussed/collimated ion beam which enters the Wien filter is usually defocussed by the mass-filtering effect. As a result, a second Einzel lens is placed after the Wien filter in order to re-collimate and re-focus the mass-filtered ion beam before final deceleration to the desired ion energy. Hence, beam focussing is needed to minimize ion current losses due to defocussing.

3.4.4 Ion beam mass-separation

The ion beam entering the Wien filter (or velocity filter) contains species of different masses with the same energy. Mass-separation or discrimination is necessary to ensure that only the positive ion species of interest will bombard the target specimen Mass-filtering is accomplished in this system by a Wien (or velocity) filter [3 3,8] This velocity or (E x B) filter involves the balancing of electric and magnetic fields to filter or discriminate between the ions of different masses. In the Wien filter, the magnetic and electric field directions are required to be perpendicular to each other, and the resultant force due to the influence of both fields upon a charged particle such as positive ions in this case is given by:

$$q\,\boldsymbol{E} - q\,(\boldsymbol{v} \times \boldsymbol{B}) = 0$$

where $\boldsymbol{E}$ is the electric field strength, $\boldsymbol{v}$ is the velocity of the charged ion particle and $\boldsymbol{B}$ is the magnetic field strength The ion of mass M passing through the perpendicular electric and magnetic fields is given by

$$M = 2\,q\,v\,(B/E)^2$$

Hence, by altering the magnetic or electric field strengths, ions of mass M may be selected or filtered from the mixed species ion beam. The Colutron velocity filter model 600B is able to separate ion species ±1amu from each other (see section 3.4.6). The reactive ion species of interest for this work were $^{19}F^+$, $^{31}CF^+$, and $^{35}Cl^+$. The $^{35}Cl^+$ isotopic mass is separable from the $^{37}Cl^+$ ions in this LEIB system.

3.4.5 Beam deceleration

The five-electrode deceleration lens system used in this work performs under two dynamic modes of operation: (a) single step deceleration by using just two active electrodes; and (b) multiple focussing-deceleration by activating all five electrodes. The second operation mode was used in this thesis. The design and construction of this deceleration lens system is considered beyond the scope of this discussion and has been reported elsewhere [3.9-12]. The ion beam can be decelerated from 500eV down to 10eV. For example, Ar^+ has been decelerated to 10eV with an energy spread of ±0.5eV [3.9,12]

3.4.6 Ion mass and kinetic energy characterization

For reactive ion beam exposures of specimens, it is important to characterize the ion beam in terms of its kinetic energy spread and mass purity before ion bombardment The mass characterization is accomplished with a quadrupole mass spectrometer (QMS).

The QMS in its basic form is comprised of four metallic rods to which direct current (dc) and radio frequency (rf) signals are applied. The resulting electric field allows ion species of a given charge to mass ratio to follow a stable path through the rods to reach a detector. All other ions do not possess this stable trajectory and collide with the rods or housing chamber before reaching the detector. In this way, masses of the various ions from the low energy ion beam can be determined. The detailed performance of QMS instruments may be found in the literature [3.13,14].

A VG model SPX300 QMS used for measuring the ion beam species mass is attached to the LEIB target chamber either along the ion beam axis (Figure 3.1) or perpendicular to the beam axis. This QMS is equipped with a VG model CMX500 cylindrical mirror energy analyzer (CMA) which measures the kinetic energy of the ion beam species. A set of ion electrodes is mounted in front of the QMS for directing the ion beam into the analyzer. For the QMS located along the beam axis, the sample/Faraday cup manipulator is translated vertically until the assembly is above the ion beam (see Figure 3.1b). This allows the ion beam to enter the QMS for mass and energy characterization. For the QMS positioned at a right angle to the beam axis, a positive potential is applied with respect to ground potential to repel the positive ion beam. By turning the Faraday cup assembly to 45° with respect to the beam axis towards the QMS, the ion beam is effectively "reflected" into the QMS. In this fashion the sample/Faraday cup assembly acts as an ion beam "mirror".

Figure 3.2 shows an example of ion beam mass characterization. In Figure 3.2a, all the various positive ion species extracted from the CF_4 plasma are detected by the QMS. It should be noted that such a mass spectrum is not the same as for a CF_4 plasma

Figure 3.2 Mass spectra of the ion beam generated from the Colutron ion source using a CF_4 feedgas, (a) all species present before mass separation by the Wien filter, and (b) mass 31 corresponding to CF^+ ions after mass discrimination.

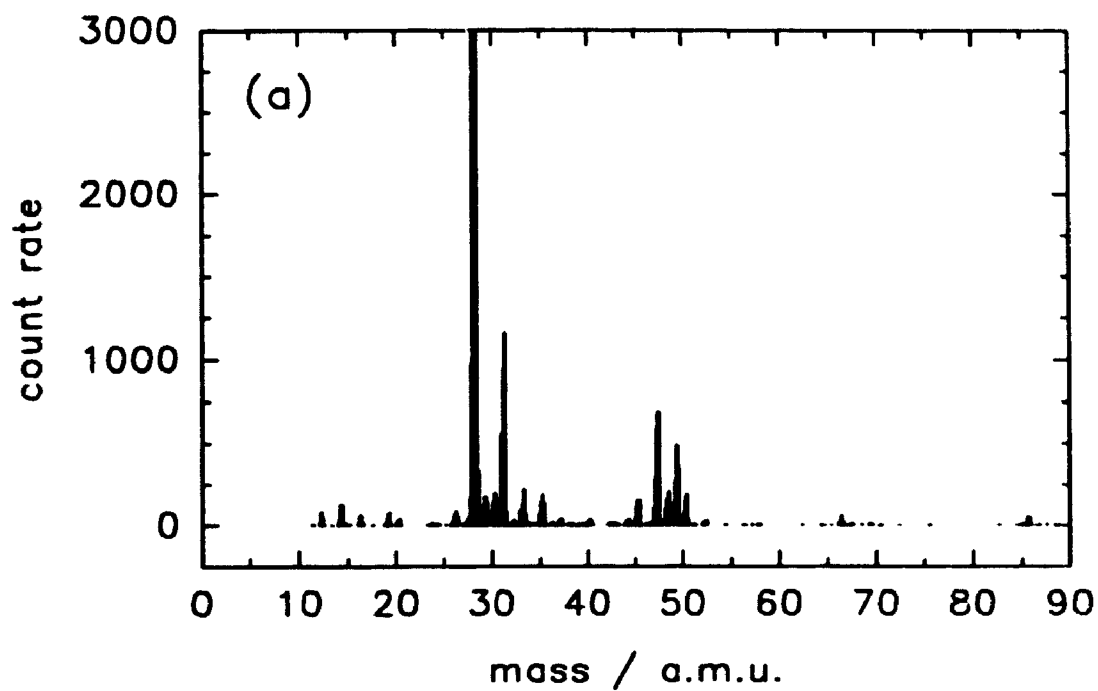
(a)
count rate
3000
2000
1000
0
0
10
20
30
40
50
60
70
80
90
mass / a.m.u.

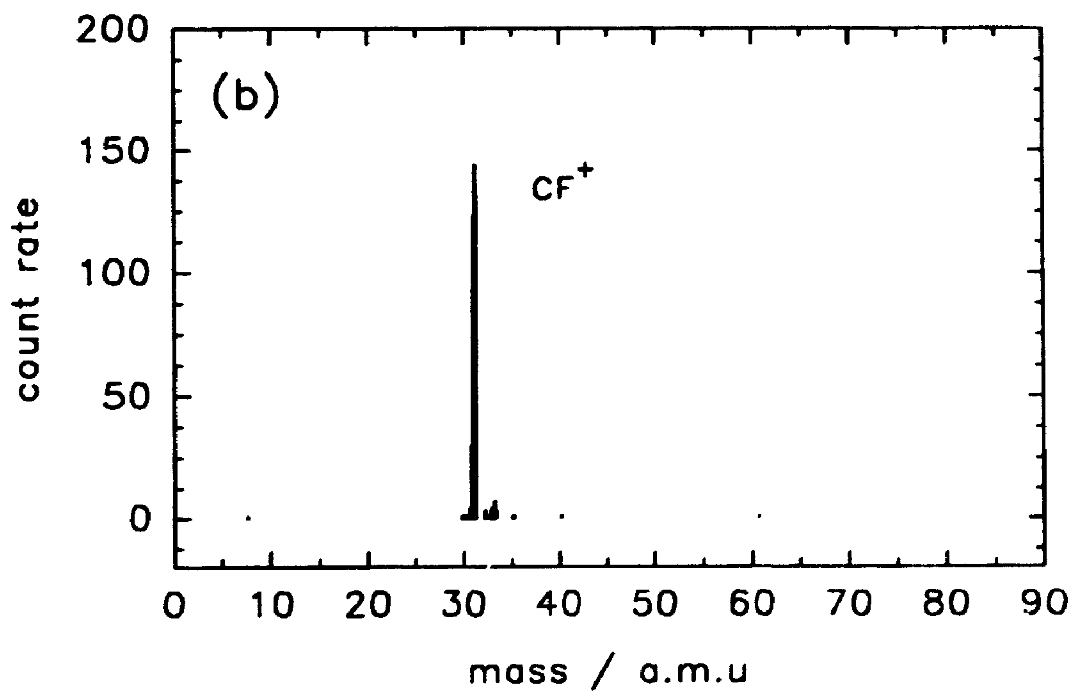
(b)
count rate
CF+
200
150
100
50
0
0
10
20
30
40
50
60
70
80
90
mass / a.m.u

present in commercial RIE systems [3.15]. In the Colutron ion source, the plasma is confined within a very small volume by a graphite jacket and exposed to relatively high temperatures, hence there is appreciable interaction between the plasma and the graphite walls [3.16]. Figure 3.2b shows the mass separation of CF^+ ions.

The ion beam energy spread is measured by the CMA. An Ar^+ ion beam at 100eV has a full-width-at-half-maximum of 1.3eV (or ±0.7eV), while at 10eV the energy spread is ±0.5eV [3.9,12]. This high energy resolution allows the low ion energy range of 1eV to 100eV to be studied.

3.4.7 Ion dose determination

The Faraday cup assembly is placed along the beam axis in order to measure the ion current. The screening hole is approximately 1.3mm in diameter and is used for beam profiling. The maximum current densities are achieved by directing and focussing the ion beam into this small hole into the Faraday cup. The ion current density inside the 1.3mm hole was calculated, and the time to achieve a required dose was estimated as

$$\text{time(s)} = [\text{ion dose}(\text{cm}^{-2}) \times 1.602\times10^{-19}(\text{C})] \,/\, [\text{current density } (\text{C s}^{-1}\,\text{cm}^{-2})]$$

For doses of 3×10^{14} to 1×10^{18} ions/cm^2 used in this work, the time to achieve such doses ranged from a few minutes to several hours.

Once the time for the required dose is calculated, the ion beam is blocked off with the gate valve between the 2nd focussing chamber and the target chamber (see Figure 3.1a), and the sample holder mounted directly above the Faraday cup is lowered into

position along the ion beam axis. The gate valve is opened and the required dose delivered to the sample surface. The dose is stopped by closing the gate valve

3.4.8 Vacuum transfer

Once a sample is exposed to the reactive ion beam, it is transferred under vacuum ($<5\times10^{-8}$Torr) to the long transfer corridor rod (see Figure 3.1a). From there it is transported into the vacuum sample transfer vessel located at the end of the corridor rod. Gate valves isolate this transfer vessel, and the vessel is removed from the system. The vacuum in this vessel is maintained below 1×10^{-7}Torr. The sample is then transferred to the XPS system for surface analysis.

3.5 Surface Analysis: X-ray photoelectron spectroscopy

3.5.1 Concepts and principles

The surface of a material is defined in its simplest sense as the outermost atomic layer of a solid [3.17], or more generally as the boundary layer of one phase at its interface with another [3.18], e.g. the outermost layer of a material in contact with a vacuum environment as in conventional surface analysis. The surface properties of a material have practical importance. For instance the surface properties of a semiconductor will influence the subsequent passivation and fabrication of a microelectronic device [3.19]. The surface properties of primary interest in this work were the concentrations of surface constituents, the chemical composition of surface species, the depth distribution of such species, and the surface band-bending characteristics.

X-ray photoelectron spectroscopy (XPS) or electron spectroscopy for chemical analysis (ESCA) is a surface sensitive technique which provides information on both the atomic concentration and chemical states of surface constituents. The fundamental principle underlying XPS is the photoelectric effect as first proposed by Albert Einstein [3.20]. Very briefly, a beam of X-rays with energy $h\upsilon$ irradiates a solid surface under ultra high vacuum conditions (see section 3.3) and the kinetic energy, *K.E.*, of photoelectrons which are ejected from the surface atoms are detected and analyzed. Figure 3.3 shows a simple energy level diagram of the process. The binding energy, *B.E.* of the photoelectrons can be determined by

Figure 3.3 Simple schematic energy level diagram illustrating the photelectric effect.

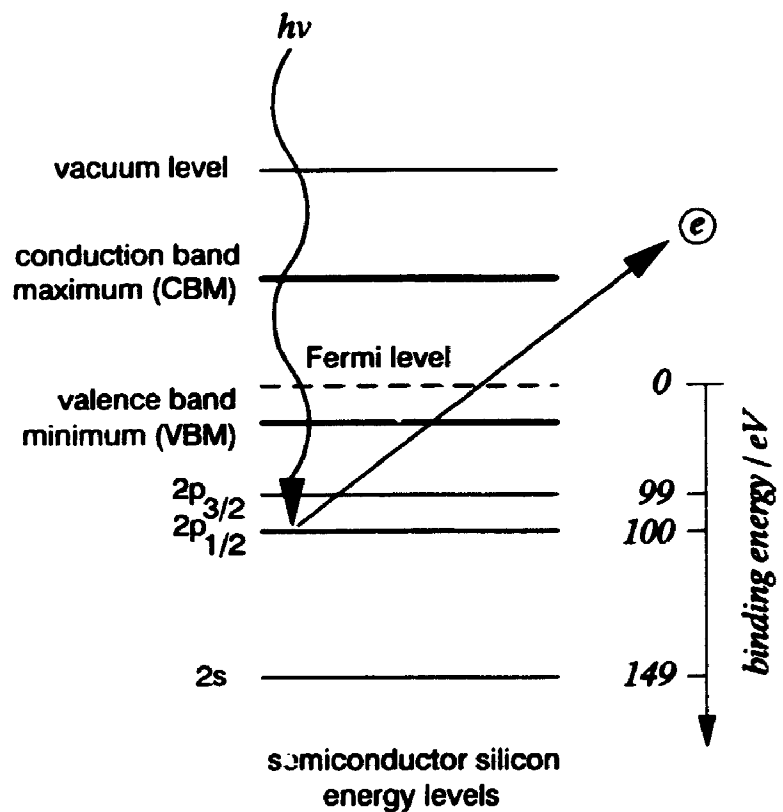

photoemission process

$$B.E. = h\upsilon - K.E. - \phi_s$$

where ϕ_s is a correction term due to the analyzer work function [3 21,22]

From this equation, if the energy of the incident X-ray beam, $h\upsilon$, and analyzer work function, ϕ_s, are predetermined, then the binding energies of the photoelectrons, *B.E.*, are known from the detection and analysis of the photoelectron kinetic energies, *K.E.*. The characteristic XPS spectrum is conventionally presented as the number of electrons detected, *N(E)* or intensity, versus electron binding energy Figure 3.4 shows examples of XPS spectra acquired with a wide electron binding energy window (low resolution survey or broad scan) and acquired with a narrow binding energy window for an isolated core-level electron (high resolution narrow scan) XPS is capable of identifying all the elements present in the periodic table except for hydrogen and helium

The kinetic energies are such that only those photoelectrons generated from the near surface region are detected since photoelectrons generated deeper within the sample undergo inelastic collisions and thus lose significant kinetic energy and are either unable to escape from the surface or escape with an energy loss. The latter photoelectrons contribute to the inelastic background signal detected in the spectrum but not to the well-defined photoelectron peaks. A further discussion of the surface sampling depth by XPS is presented in section 3.5.4.

3.5.2 Elemental identification

Surface elemental identification is possible since the binding energies of the core electrons are specific to each element In the majority of cases, XPS studies focus on the

Figure 3 4 Examples of XPS spectra as (a) survey scan of Si surface after wet HF etch, and (b) high-resolution scan of the Si2p core-level of an Si surface with a thin SiO_2 native oxide overlayer.

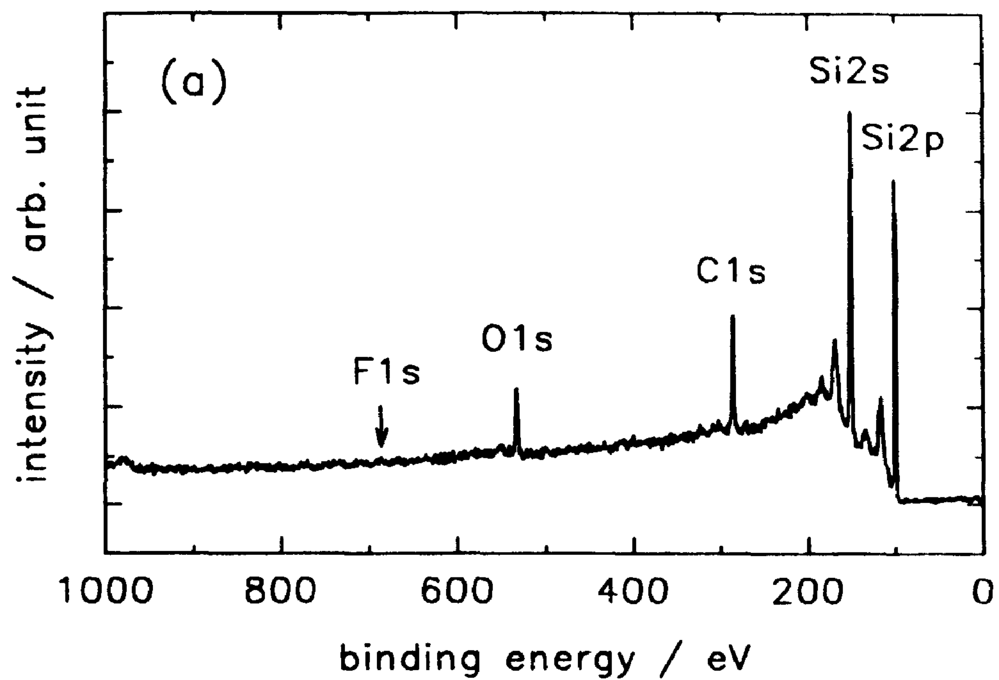
(a)
Si2s
Si2p
C1s
O1s
F1s
intensity / arb. unit
1000
800
600
400
200
0
binding energy / eV

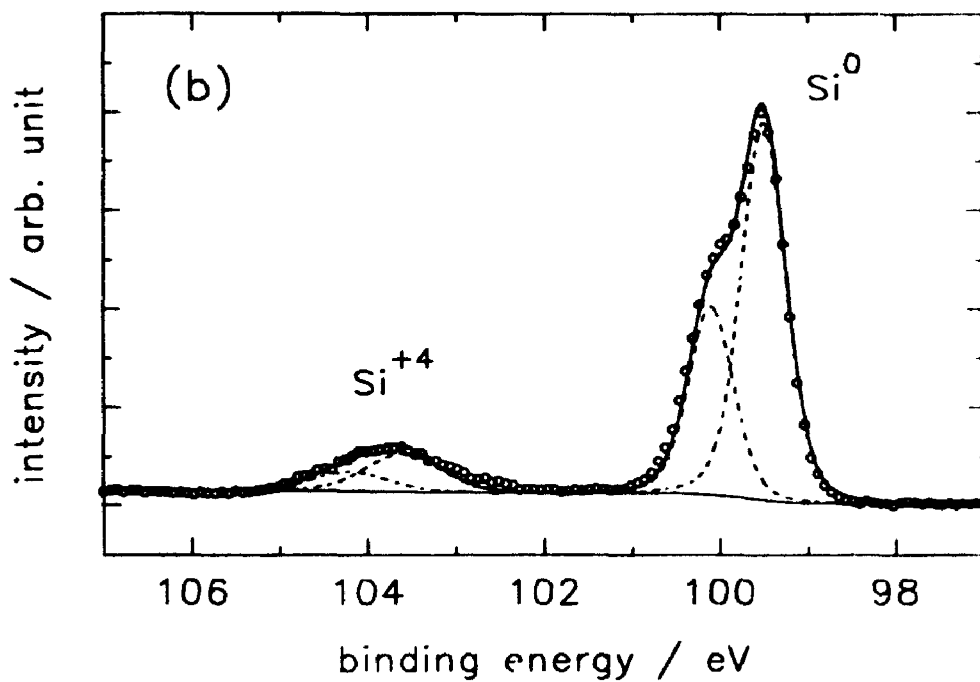
(b)
Si^0
Si^+4
intensity / arb. unit
106
104
102
100
98
binding energy / eV

analysis of core-level electrons. Auger electrons are also detected by XPS because these electrons possess kinetic energies in the same range as the core-level photoelectrons. However, surface analysis by Auger electron spectroscopy (AES) was not considered in this thesis For treatments of AES, the reader is referred to texts found in the literature [3.17,23]. Figure 3.4a shows an example of the elements identified from core-level and plasmon loss peaks [3.17] from a semiconductor silicon wafer after a wet HF solution etch to remove surface native oxide and contaminants.

3.5.3 Chemical state information

The binding energy of the core electron is defined as the energy difference between the Fermi level and the ground state of the core-level electron [3.24] (see Figure 3.3) Binding energies of core electrons are very sensitive to the chemical environment of the elemental atoms under consideration, and the chemical state (oxidation state) for the surface elements may be determined from the "chemical shift" of the photoelectron binding energies [3.25]. The chemical shift arises because a rearrangement of the valence electrons changes the potential felt by the core electrons, and the difference in chemical states is manifested by a change in binding energy for the core-level electron of an atom. Hence, an increase in oxidation state corresponding to electron charge transfer is manifested as a shift of the core-level peak towards higher binding energy than the atom in its elemental or 0 oxidation state.

Since the XPS core-level spectral profile is dependent on the photoelectron binding energy and chemical state of the surface element, the final spectrum represents a convolution of all the separate photoelectron peaks. Peak-fitting programs are routinely

used to deconvolute the peak profile in order to obtain information about surface chemical states. Figure 3.4b shows an example of a thin surface silicon dioxide (SiO_2) layer present on silicon. The +4 oxidation state of silicon as SiO_2 is "chemically shifted" in binding energy from the elemental silicon in the 0 oxidation state. Judicious assignment of peaks characteristic of different chemical environments requires comparisons with tabulated literature values as well as insight into the particular material surface under investigation.

3.5.4 Non-destructive shallow depth-profiling

The surface analysis depth in XPS varies with the photoelectron kinetic energies under consideration. The intensity of electrons, I, emitted from a depth, d, is given by the Beer-Lambert relationship [3.26]:

$$I = I_o \exp \{ -d / (\lambda \cos\theta) \}$$

where I_o is the electron intensity from an infinitely thick and clean substrate, θ is the polar angle of photoelectron emission with respect to the sample normal. The decay constant λ represents a characteristic length such that the intensity ratio I/I_o is attenuated by $1/e$. This λ is called the inelastic mean free path (IMFP) of the photoelectrons. The IMFP of the electrons varies with the kinetic energy. Figure 3.5 shows the "universal curve" of the electron kinetic energy dependence on λ [3.27]. The IMFP in monolayers represents approximately 1 to 3nm depths from the solid surface, hence the high surface sensitivity of this technique.

The Beer-Lambert equation can be used to provide non-destructive shallow depth-

Figure 3.5 The "universal curve" dependence of IMFP on electron kinetic energy (due to Seah and Dench [3.27]).

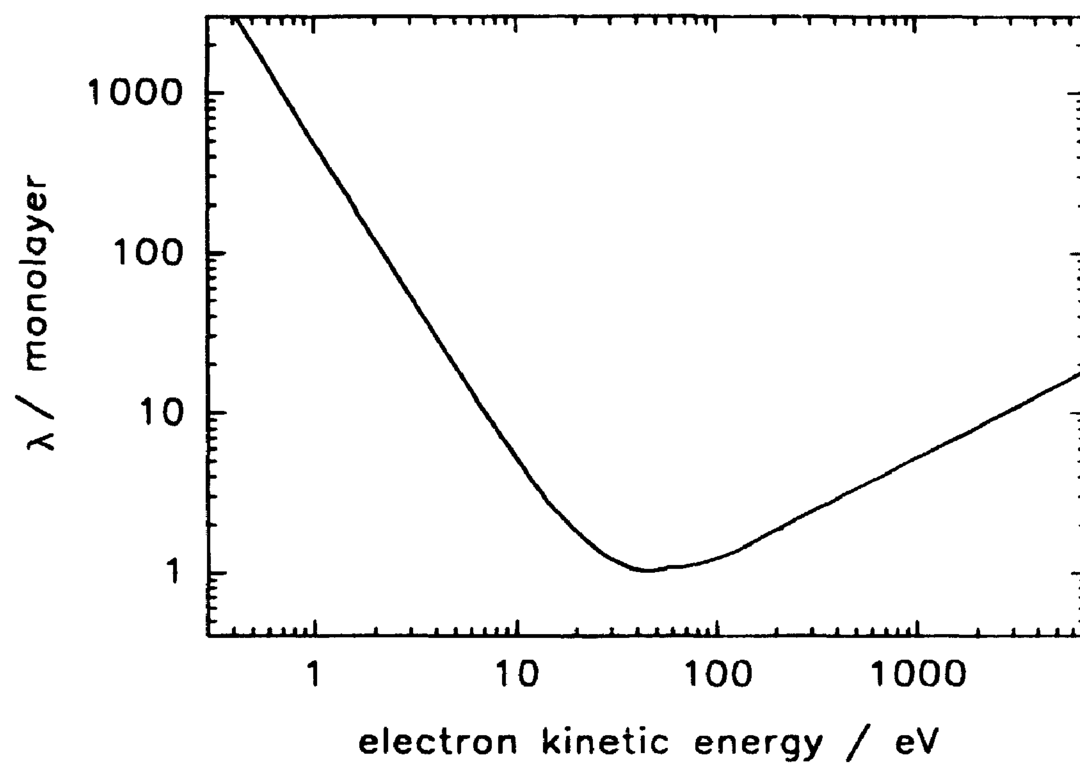
1000
100
10
1
λ / monolayer
1
10
100
1000
electron kinetic energy / eV

profile information about the surface under investigation. It can be shown [3.26] that by analyzing the intensity of photoelectrons emerging at $\theta=0°$ (i.e. emission normal to the sample plane), 63% of the XPS signal will emerge from a depth of λ, and the majority of the signal at 86% will emanate from a depth of 2λ. Therefore, an estimation of the sampling depth is given by

$$d = 2\,\lambda \cos\theta$$

Values for λ have been calculated [3.27-30] to be approximately 0.5 to 4nm, and as values of λ are near 3nm for a material such as silicon [3.29], the effective maximum sampling depth is only 5 to 6nm.

Under typical XPS analysis conditions in this thesis, the data collection is carried out at only one photoelectron polar angle of 55° and the surface composition is assumed to be uniform throughout the sampling depth (see section 3.5.8). However, in angle-dependent or angle-resolved XPS (ARXPS), spectra are acquired as the polar angle is varied. Figure 3.6 shows the geometry in ARXPS. By changing the polar angle, the effective sampling depth increases or decreases and information is gained from both the elemental concentration and chemical species depth-profile. This non-destructive depth analysis [3.17,27] can be used to characterize thin films, to enhance surface sensitivity of analyses for very thin layers, and to distinguish between thin surface overlayer homogeneity or island distribution of surface films.

Attempts have been made to deconvolve the ARXPS data into elemental and chemical species depth distributions with several mathematical algorithms [3.27,31,32].

Figure 3.6 Variation in XPS surface analysis depth with changes in the polar angle of photoelectron detection.

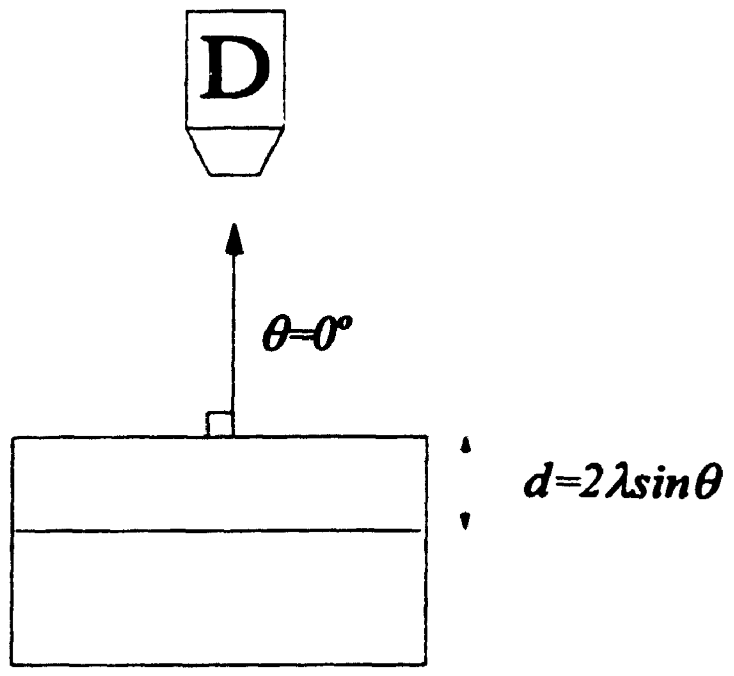
D
θ=0°
d=2λsinθ

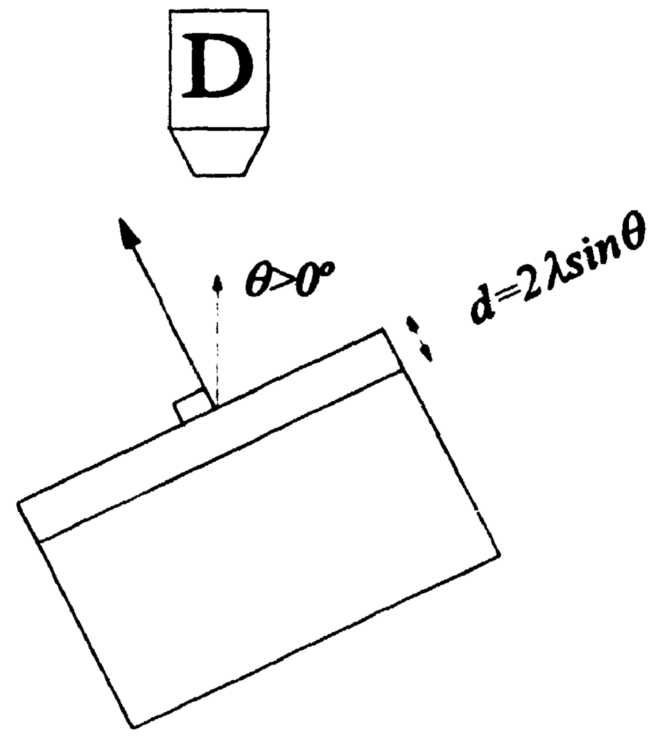
D
θ>0°
d=2λsinθ

The deconvolution approach due to Bussing and Holloway [3.33] was used in this work to simulate the depth distribution of Si-containing surface species (see Chapter 6, section 6.3.2.). High resolution XPS spectra were collected for the Si2p, C1s, O1s and F1s core-levels at pass energies of 150eV for quantitation and at 50eV for high spectral discrimination of the different chemical species present. The data were collected at various photoelectron takeoff angles with respect to the sample normal (i.e. polar angle, θ). The IMFP for all core lines under consideration are needed for the simulation and can be obtained from the literature [3.27-30]. The deconvolution model was available on a personal computer and required the input of the data collected at specified polar angles along with the IMFP values. For the determination of Si-containing species a constant IMFP of 3.0nm was used [3.29] because the kinetic energies of the photoelectrons were all derived from the Si2p core-level.

An alternative method of obtaining non-destructive shallow depth information is by studying the photoelectrons emitted from different core-levels of the same atom. Since the IMFP varies with electron kinetic energy (Figure 3.5), by selecting a pair of electron transitions accessible to XPS but also widely separated in kinetic energy, it is possible to obtain a degree of depth selectivity [3.26]. In the case of the fluorine atom which is present after low energy F^+ ion bombardment, the F1s core-level (from the "universal curve" [3.27], electron K.E ≈800eV, $\lambda \approx 2.7$nm) and F2s level (electron K.E ≈1450eV $\lambda \approx 3.7$nm) can be used to evaluate the depth of fluorine penetration into the surface of silicon.

3.5.5 Destructive ultra-shallow depth-profiling

The erosion of surface layers to perform depth-profiling analysis has been traditionally accomplished by energetic (1 to 10keV) argon ion (Ar^+) bombardment [3.17,34]. In this approach, the surface is physically sputtered for a controlled duration and, after the sputtering is terminated, surface analysis by XPS or AES is performed. After the analysis of this surface, the sputtering followed by surface analysis is repeated in order to obtain the depth-profile. High resolution mass analysis of ions sputtered at subsequent depths constitutes the technique of secondary ion mass spectrometry (SIMS) [3.34]. These forms of depth-profiling analyses require the physical sputtering of surface atoms with energetic positive ions. Such ion bombardment produces artefacts such as preferential sputtering of different surface elements at different rates. This effect results in a distortion of the concentration depth-profile at greater depths. Another artefact induced by the bombardment process is the physical damage to the surface in form of the crystal disorder and both direct and recoil implantation of surface species. This then sets a lower limit to the depth resolution achievable in the profiling [3.35]. The ion mixing depth is larger than 0.5nm at an ion sputtering energy of 1keV [3.35].

A new approach to depth-profiling silicon has been recently developed [3.36] in which controlled thicknesses of silicon are removed with a depth resolution of 0.5nm followed by surface analysis by XPS. The erosion process was accomplished by ozone oxidation of the silicon to consume known amounts of silicon followed by removal of the oxide by a wet hydrofluoric acid (HF) etch treatment. This erosion process avoids some of the major artefacts induced by traditional ion sputter depth-profiling. The oxidation kinetics of Si are well-studied [3.37,38] and the SiO_2-Si interface is atomically abrupt [3.39]. Therefore, the SiO_2 / Si system is an ideal system for this depth-profiling

procedure. In addition, the wet HF treatment results in a hydrogen-terminated Si surface with a flatband condition [3.1,2,40,41] which is passive or resistant to oxidation within the time it takes to load the sample into the XPS (typically 2min).

The Si sample is loaded into a small ultraviolet ozone reactor [3.36] which is purged with oxygen gas (O_2) bubbled through deionized water. A low pressure mercury (Hg) lamp was used to generate the ozone from the O_2 present in the reactor. The sample is exposed to ozone for a fixed duration, and this exposure results in a thin, reproducible oxide layer. The thickness of the oxide was determined by XPS from measuring the Si2p intensities due to the oxide and substrate Si components using the following equation [3.36]:

$$t_o = \lambda_o \cos\theta \ln [(I_o / I_s) (\rho_s / \rho_o) (\lambda_s / \lambda_o) + 1]$$

where λ_s and λ_o are the respective IMFP of the Si2p photoelectrons in silicon and silicon dioxide; ρ_s and ρ_o are the respective atom density of silicon in silicon ($5 \times 10^{22}/cm^3$) and silicon dioxide ($2.2 \times 10^{22}/cm^3$); and θ is the polar angle (55°) used for the analysis. By assuming that the IMFP of the Si2p photoelectrons in Si and SiO_2 are both 3.0nm [3.29,30], the average oxide thickness of 0.8 ± 0.2nm is obtained. The thickness of Si consumed in the oxide is approximately 0.45 times the oxide thickness. Hence, the amount or thickness of Si removed by oxidation step is approximately 0.4 ± 0.1nm. In this depth profiling procedure, the oxide layer was removed by a wet 5% HF in deionized water etch for 60s and rinsed with deionized water for 1min.

After the removal of each thin 0.5nm layer of Si, the sample surface was analyzed by XPS to determine the presence of different chemical species. This removal of ultra-shallow Si layers plus XPS analysis constitutes the destructive, depth-profiling technique. In addition, the samples can be analyzed with the oxide layer intact. For this surface condition, low energy flooding electrons are used to charge the sample negatively within the XPS analytical chamber. Spectra are acquired before and after the sample is charged negatively. This surface charging technique is discussed in the next section.

3.5.6 Surface charging spectroscopy

A new technique has been recently developed to study the quality of thin dielectric-semiconductor structures [3.42-44]. This technique requires an XPS spectrometer with high energy resolution and a controlled low energy electron floodgun to charge the specimen surface negatively. The information available from the surface charging spectroscopy (SCS) include Fermi level (FL) "pinning" of the semiconductor at the dielectric-semiconductor interface and the insulating properties of the dielectric [3.42,43]. A further application of SCS is the quantification of the degree of Fermi level pinning, i.e. the measurement of interface state densities within the semiconductor bandgap [3.46]. The sample structure is typically a thin dielectric overlayer on a semiconductor. The overlayer must be thin enough in order to allow detection of core-level photoelectrons from the underlying semiconductor substrate. This sets an upper limit of approximately 10nm for the overlayer thickness based upon the effective sampling depth achievable from XPS (see section 3.5.4). This technique is used in this thesis only to evaluate qualitatively the surface Fermi level pinning phenomenon using a constant

electron floodgun energy of 2eV (see Chapter 4, section 4.3.3)

The negative charging of the dielectric surface produces an upward surface band-bending condition for an ideal dielectric-semiconductor interface. This is manifested as a shift (of less than 1eV) in the core-level peaks towards lower binding energy compared to the case of no surface charging. If there is an appreciable density of electrically active defect states at the interface, this then contributes to a number of states present within the bandgap and are sometimes termed gap states [3.45]. The external charge from an applied voltage (in this case the low energy flooding electrons) may be consumed by filling or emptying these gap states instead of being used to influence the occupancy of the valence and conduction bands of the semiconductor. As a result, the semiconductor surface no longer responds to the negative charging and the core-level peaks do not shift after negative charging, i.e. the Fermi level is "pinned".

The Si specimens with a back ohmic contact were mounted onto stainless steel holders which are in contact with the spectrometer. This ensured that proper electrical contact was maintained. High resolution spectra are acquired of the Si2p core-level before and after charging the sample surface. The specimen consists of the thin approximately 1nm thick SiO_2 overlayer grown by ozone oxidation on the semiconductor Si substrate (see section 3.5.5). The Si2p core-line is peak-fitted in order to determine the shifts of peak positions induced by SCS. The difference in binding energy values before and after negative surface charging is used to evaluate surface FL pinning. The XPS analysis chamber has a small light to illuminate and locate the sample region for analysis. However, for all samples analyzed in this thesis, the illumination to the sample is turned off in order to avoid photocurrent effects.

3.5.8 Instrumentation

Surface analysis was carried out in a Surface Science Laboratories (SSL) Model SSX-100 X-ray photoelectron spectrometer [3.46] which was incorporated into a custom-designed/built ultra high vacuum system [3.47]. Figure 3.7 shows a general schematic of the system. Features of this system include a separate sample introduction chamber and an isolated sample preparation chamber for vacuum heating and ion-sputter cleaning of specimens, in addition to the main spectrometer analysis chamber. Both the sample preparation and analysis chambers are separately connected to the introduction chamber.

The spectrometer features a monochromatic Aluminum (Al) Kα X-ray source, ($h\upsilon$=1486.6eV) with variable source power operated between 10 and 200W at 10keV, selectable small spot sizes and variable resolution settings. The spectrometer functions are controlled by a Hewlett-Packard Model 9836 microcomputer. This microcomputer is also equipped with SSL software used for data analysis and manipulation, e.g. determination of surface atomic compositions and an iterative chi-squared peak-fitting program for analysis of high resolution spectra. The vacuum conditions in the analysis chamber were maintained by turbomolecular and ion pumps in a suitable configuration. The introduction chamber uses a turbomolecular pump which initially pumps down the chamber from ambient to pressures below 10^{-6}Torr, and at this point a gate valve separating the introduction and analysis chambers is opened. The specimen holder is transferred into the analysis chamber with a long feed through rod. The majority of samples were analyzed within a vacuum pressure range of 2 to 6×10^{-9}Torr.

The AlKα X-rays are generated by an electron beam bombarding an Al anode at 15kV. The $K\alpha_{1,2}$ doublet has a linewidth of approximately 0.85eV [3.3,17] and after

Figure 3.7 Schematic drawing of the custom-built UHV system incorporating the SSX-100 XPS spectrometer

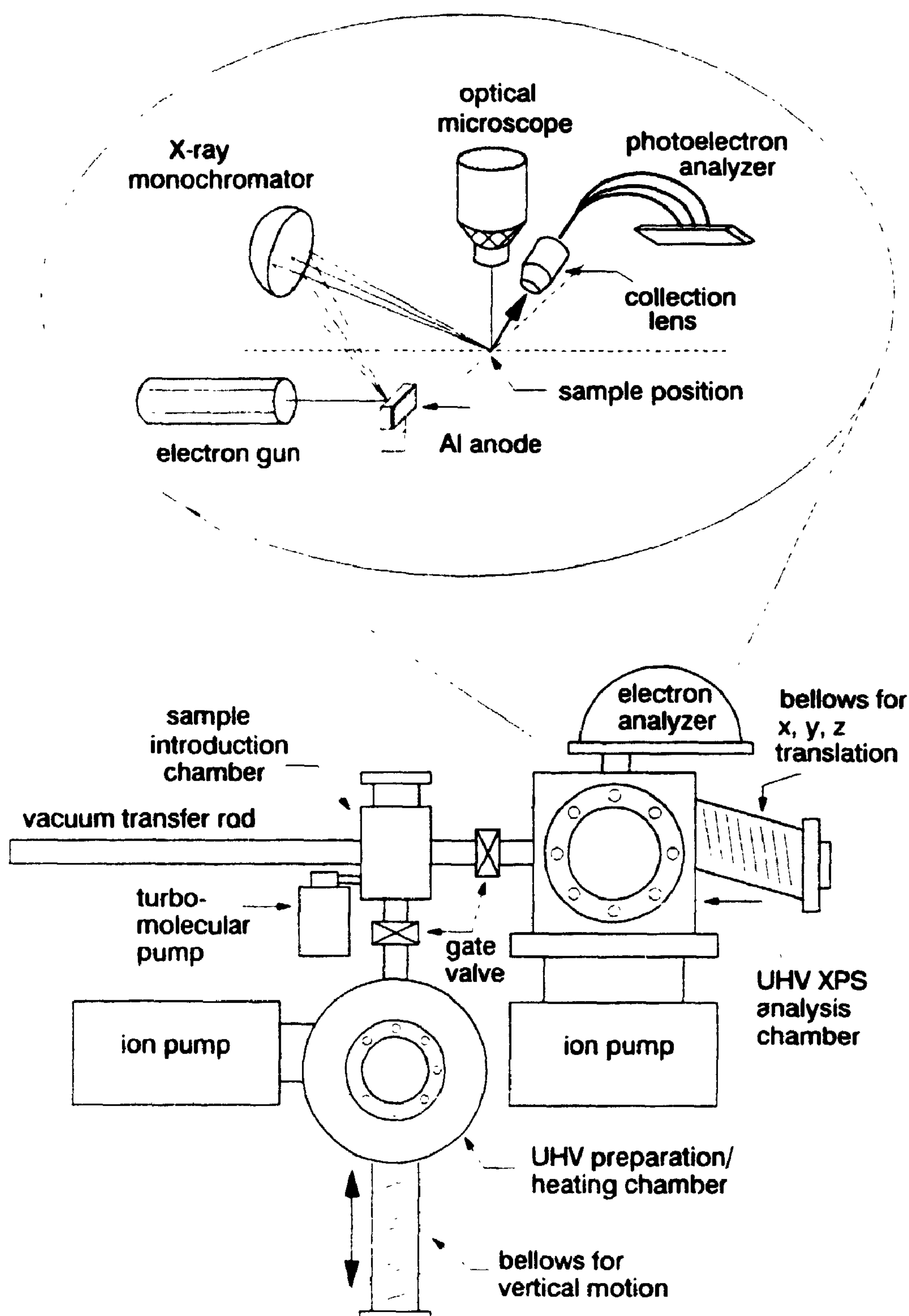
optical
microscope
X-ray
monochromator
photoelectron
analyzer
collection
lens
sample position
electron gun
Al anode
electron
analyzer
bellows for
x, y, z
translation
sample
introduction
chamber
vacuum transfer rod
turbo-
molecular
pump
gate
valve
UHV XPS
analysis
chamber
ion pump
ion pump
UHV preparation/
heating chamber
bellows for
vertical motion

monochromatization and final X-ray spot focussing with a Johansson bent quartz crystal [3.46], the diffracted Kα_1 line at 1486.6eV has a linewidth of 0.35eV [3.3,17]. The Al anode, quartz crystal and the specimen surface lie on a Rowland circle [3.17,46] to fulfill the proper X-ray diffraction conditions (see Figure 3.7). The final X-ray spot size at the sample surface is determined by changing the size of the electron beam at the anode. The present XPS instrument is capable of focussing AlKα_1 X-rays as a circular spot between 1000 and 150µm in diameter onto the sample surface. For all samples analyzed in this thesis, a spot size of 300µm in diameter was employed.

The specimen holder sits on a rotatable carousel sample holder stage which holds up to 5 holders in the analysis chamber. The carousel is capable of transition in the x,y,z directions. For specimen holders in the carousel centre position, rotational freedom in 360° is possible with a vertical axis of rotation. This rotational freedom is necessary for angle-dependent XPS analysis (see section 3.5.4). The sample surface is brought to the coincidence point of the spectrometer by vertical translation of the carousel stage under an optical microscope (Figure 3.7). The focal point of the microscope is matched with the focal point of the diffracted, monochromatized AlKα X-rays along the Rowland circle and the focal point of the electron transfer lens of the detector.

In the conventional horizontal sample position, the ejected photoelectrons from the sample surface are collected at a polar angle of 55° (or 35° with respect to the sample plane) by the electron transfer lens system. The collected photoelectrons are focussed and retarded to a constant kinetic energy before entering the analyzer (Figure 3.7). The analyzer is an energy-dispersive instrument using electrostatic field [3.17,23] called a concentric hemispherical analyzer (CHA). Two hemispherical sectors are placed

concentrically with a suitably applied potential between sectors. The energy of the photoelectron through the analyzer (pass energy) and the applied voltage produce a constant absolute analyzer resolution. The photoelectron kinetic energy is measured by varying the retarding potential of the electron lens system. Electrons of different energies follow different orbits within the CHA, and the range of energies are dispersed over the length of a position sensitive detector. An electron reaching the position sensitive detector strikes a channel plate electron multiplier and the position of the event is resolved by a resistive anode encoder. The distribution of stored events is converted into a conventional XPS binding energy spectrum.

3.5.8 Quantitative analysis

Quantitative XPS provides information on the surface atomic compositions over the area illuminated by the soft X-ray spot. It is generally possible to achieve accuracies within 10 to 20% for most elements of the periodic table [3.48]. The basic assumptions made in the quantification are that the surface is homogeneous over the sampling region, surface roughness is minimal, and that contamination layers of carbon (C) and oxygen (O) do not significantly contribute to the analysis. Discussions of quantitative analysis by XPS may be found in the literature [3.16,23,48].

The surface composition of an element i from a chosen core-level, C_i, is proportional to the core-level peak area, A_i, and to the probability for ejecting a photoelectron from a given atomic orbital (electron photoionization cross-section [3.17]), σ_i such that

$$A_i = C_i\ (\ SF_i\ )$$

$$SF_i = \sigma_i\ \{\ KE_i\ /\ KE_o\ \}^f$$

where SF_i is the instrumental sensitivity factor which is dependent on the specific element and the spectrometer instrument. KE_o is the kinetic energy of the carbon (C) 1s photoelectron reference element, and f is a spectrometer factor equal to 0 7 for the SSX-100 system. By determining relative compositions and normalizing the concentrations of elements to 100%, a surface atomic composition table is generated with

$$C_i\ /\ C_k = [\ A_i\ /\ SF_i\ ]\ x\ [\ SF_k\ /\ A_k\ ]$$

and

$$\Sigma C_i = 100\%$$

Quantification was performed from measured peak areas for all elements present in this work. All quantitative data collection was carried out with an X-ray spot size of 300μm in diameter at a constant analyzer pass energy of 150eV as specified by the SSX-100 spectrometer. For this pass energy, the spectrometer transmission function was assumed to be proportional to $KE^{0.7}$ Peak areas were determined using a linear background correction, and photoionization cross-sections were taken from the theoretical calculations by Scofield [3.49]. Table 3.1 lists the sensitivity factors for those elements considered in the quantitative analysis, along with an example case of surface atomic

Table 3.1 Surface compositions of elements present after wet HF etching of silicon and list of sensitivity factors used in the quantification of surface elements

Element	B.E.	SF_i	Atom %
Si2p	099.7eV	0.903	67.9
C1s	285.0eV	1.000	24.4
O1s	532.2eV	2.494	07.3
F1s	686.7eV	3.333	00.4

concentrations from a wet HF etched Si surface to remove the silicon dioxide overlayer The supplied SSX-100 computer software automatically calculated the surface atomic compositions and normalized the values to 100%

REFERENCES

3.1 K. Graf, M. Grundner, R. Schutz, J. Vac. Sci. Technol., A7, 808, 1989.

3.2 N. Hirashita, M. Kinoshita, I. Aikawa, T. Ajioka, Appl. Phys. Lett., 56, 451, 1990

3.3 J.C. Riviere, Surface Analysis Techniques, Monographs on the Physics and Chemistry of Materials, Clarendon Press, Oxford, 1990.

3.4 J.C. Riviere, in Practical Surface Analysis, Vol. 1, J. edited by D. Briggs, M.P. Seah, Wiley & Sons, Chichester, 1990.

3.5 L.G. Meiners, R.P. Pau, J.R. Sites, J. Vac. Sci. Technol., 4, 961, 1977.

3.6 Colutron Research Corporation, 2321 Yarmouth, Boulder, Colorado, 80301, USA.

3.7 J.H. Freeman, G. Sidenius, Second Int. Conf. Ion. Sources, Wien, 724, 1972.

3.8 R.G. Wilson, G.R. Brewer, Ion Beams, J. Wiley & Sons, New York, 1973.

3.9 Wien filter operation

3.10 K.K. Foo, M.Sc. thesis, University of Alberta, 1991.

3.11 K.K. Foo, R.P.W. Lawson, X. Feng, W.M. Lau, J. Vac. Sci. Technol., A9, 312, 1991

3.12 W.M. Lau, X. Feng, I. Bello, S. Sant, K.K. Foo, R.P.W. Lawson, Nucl. Instrum. Methods B, 59/60, 316, 1991.

3.13 P.F.A. Meharg, PhD thesis, University of British Columbia, 1992.

3.14 P.H. Dawson, N.R. Whetten, Dyn. Mass Spectrom., 2, 1, 1969.

3.15 J.W. Coburn, H.F. Winters, J. Vac. Sci. Technol., 16,391, 1979

3.16 I. Bello, W.H. Chang, X.H. Feng, W.M. Lau, Nucl. Instrum. Methods B,

80/81, 1002, 1993.

3.17 D Briggs, M.P Seah, Practical Surface Analysis, Vol 1, J Wiley and Sons, Chichester, 1983, and references therein

3.18 M. Prutton, Surface Physics, Clarendon Press, Oxford, 1983

3.19 L.G. Meiners, H.H Wieder, Mater Sci Rep., 3, 139, 1988

3.20 A. Einstein, Ann. Phys., 17, 132, 1905

3.21 K. Siegbahn, D.A. Allison, J.H Allison, Handbook of Spectroscopy, Vol 1, edited by J.W. Robinson, CRC Press, Cleveland, 1974

3.22 L.C. Feldman, J.W Mayer, Fundamentals of Surface and Thin Film Analysis, North-Holland, New York, 1986

3.23 T.A. Carlson, Photoelectron and Auger Spectroscopy, Plenum Press, New York, 1975

3.24 K. Siegbahn, C.N. Nordling, A. Fahlman, R Nordberg, K Hamrin, J Hedman, G. Johansson, T Bermark, S.E. Karlsson, I Lindgren, B Lindgren, ESCA Atomic, Molecular and Solid State Structure Studied by Means of Electron Spectroscopy, Almqvist and Wiksells, Uppsala, 1967

3.25 W F. Egelhoff Jr, Surf Sci Rep., 6, 253, 1987

3.26 J.F Watts, in An Introduction to Surface Analysis by Electron Spectroscopy Royal Microscopical Society Microscopy Handbook 22, edited by C H Hammond, Oxford University Press, Oxford, 1990

3.27 M.P. Seah, W.A Dench, Surf Interface Anal., 1(1) 2, 1979

3.28 S Tanuma, C J. Powell, D R Penn, Surf Interface Anal., 11 577, 1988

3.29 S Tanuma, C.J Powell, D R Penn, Surf Interface Anal., 17 911 1991

3.30 S. Tanuma, C.J Powell, D R Penn, Surf Interface Anal., 17, 927, 1991

3.31 R.W. Paynter, Surf. Interface Anal., 3, 186, 1981.

3.32 M.F. Ebel, J. Wernisch, Surf. Interface Anal., 3, 191, 1981

3.33 T.D. Bussing, P.H. Holloway, J. Vac. Sci. Technol., A3(5), 1973, 1985

3.34 D. Briggs, M.P. Seah, Practical Surface Analysis, Vol. 2, J. Wiley and Sons, Chichester, 1992, and references therein

3.35 C.W. Magee, R.E. Honig, Surf. Interface Anal., 4(2), 35, 1982, and references therein

3.36 W.M. Lau, L.J. Huang, W.H. Chang, M. Vos, I.V. Mitchell, Appl. Phys. Lett., 63(1), 78, 1993

3.37 B.E. Deal, A.S. Grove, J. Appl. Phys., 36, 3770, 1965

3.38 R.C. Jaeger, Introduction to Microelectronic Fabrication, Addison-Wesley, Reading, Massachussetts, 1988, and references therein

3.39 C.R. Helms, in The Si-SiO_2 System, edited by P. Balk, Elsevier, Amsterdam, 1988

3.40 L.J. Huang, W.M. Lau, Appl. Phys. Lett., 60, 1108, 1992

3.41 L.J. Huang, W.M. Lau, P.J. Simpson, P.J. Schultz, Phys. Rev. B, 46, 4086, 1992

3.42 W.M. Lau, Appl. Phys. Lett., 54(4), 338, 1989

3.43 W.M. Lau, J. Appl. Phys., 67(3), 1504, 1990

3.44 W.M. Lau, X.W. Wu, Surf. Sci., 245, 345, 1991

3.45 R.W. Kwok, PhD thesis, 1993, The University of Western Ontario

3.46 R.L. Chaney, Surf. Interface Anal., 10, 36, 1987

3.47 S. Ingrey, W.M. Lau, N.S. McIntyre, J. Vac. Sci. Technol., A4, 984, 1986

3.48 T.A. Carlson, Surf. Interface Anal., 4, 125, 1982

3.49 J.H. Scofield, J Electron Spectrosc Relat Phenom., 8, 129, 1976

CHAPTER 4.

RIE OF SILICON:

SURFACE CHARACTERIZATION

4.1 Introduction

Reactive ion etching of silicon dioxide (SiO_2) and silicon (Si) with fluorocarbon-based plasmas such as CF_4, CHF_3 and CCl_2F_2 results in selective etching. The selective etching of SiO_2 on Si substrates is believed to occur from reactive fluorocarbon species (such as ions, radicals and neutrals) forming gas phase volatile reaction products with the SiO_2 such as CO and CO_2 for the consumption of carbon in the dry etching system [4.1]. Once the oxide has been etched away, the reactive fluorocarbons are exposed to the underlying Si, but the reaction probability of volatile Si products is low because the depletion of oxygen slows down the carbon consumption pathway. Subsequently, the plasma fluorocarbon species possess a greater reaction probability for fluorocarbon film deposition. The selectivity is characteristic of the gas etch system, and the etching rate of Si is much less than that of SiO_2 for the CF_4/H_2 [4.2] and CHF_3 [4.3] systems. In comparison, the anisotropy (directional etching) in RIE is achieved via the energetic reactive ion bombardment of the sample at normal incidence with kinetic energies near 500eV [4.4].

Ion bombardment in the RIE process is known to play an important role in both

the formation and release of the etch products [4.5-9]. A common concern in RIE is the residual surface damage which develops in the surface region. This damage is induced by collisional cascades associated with the energetic, reactive ion bombardment [4.10]. It is known [4.4,4.11-14] that the residual damage on silicon (Si) induced by fluorocarbon-based RIE of silicon dioxide (SiO_2) through to the Si consists of a fluorocarbon overlayer which suppresses the etch rate once the SiO_2 layer is consumed, a few nanometres of defective silicon which is also contaminated with carbon (C), fluorine (F), and oxygen (O), and a few hundred nanometres of silicon which is doped with hydrogen from the RIE plasma. The composition and structure of the film has been characterized by a variety of analytical techniques including, XPS, AES, SIMS, TEM, RBS/Channelling, and Raman spectroscopy. The prevalent model for the RIE-induced modified structure or Si reaction layer at the film-substrate interface includes a silicon carbide (SiC)-containing region and a relatively deep (30nm) damage region [4.15]. Other workers [4.16] have also reported graphitization of the polymer film as a result of ion bombardment during RIE.

The fluorocarbon overlayer as well as the contaminated and damaged Si layer must still be removed prior to subsequent device fabrication. Ideally, the removal of the RIE residual damage should minimize the levels of contamination and defects. In addition, as device dimensions are shrinking continuously, uncontrolled and excessive etching of the substrate material for removing the residual damage becomes less acceptable. Hence, the development of new techniques for accurate measurement of the damage depth and precise control of residual damage removal are timely.

XPS was chosen as an appropriate surface analysis technique because it provides surface elemental identification and quantification as well as valuable information on the

chemical states of the surface species (see Chapter 3, section 3.5). This technique also allows nondestructive depth profiling to be carried out by changing the included angle between the direction of photoemission detection and the surface normal, i.e. the polar photoemission angle (see Chapter 3 section 3.5.4). In addition, the exposure of sample surfaces to such X-ray fluxes as used in this work has been shown [4.17] to negligibly affect the surface conditions. Recently, it has been shown [4.18,19] that the surface potential at a thin dielectric-semiconductor interface can be studied by XPS in conjunction with charging the sampling by a low energy electron floodgun. This surface charge spectroscopy (SCS) allows the evaluation of the degree of Fermi level pinning caused by defect states in the bandgap of the semiconductor (see Chapter 3 section 3.5.6 on SCS).

Ultrashallow depth-profiling by ozone oxidation + hydrofluoric acid (HF) wet etch cycling (Chapter 3, section 3.5.5) allows the determination of compositional profiling, and surface potential profiling. Briefly, the controlled removal of 0.5nm thin layers of Si was accomplished by ultraviolet ozone (UV/O_3) oxidation of the Si followed by a wet etch in an aqueous HF solution to remove the oxide formed [4.20]. The etch depth per oxidation/oxide etch cycle of 0.5nm for Si was calibrated by a Si(4nm)/Ge(0.5nm)/Si superlattice structure grown by molecular beam epitaxy. Sequential measurements of surface composition by a nondestructive surface analytical technique such as XPS will thus provide depth distributions of chemical phases. In addition, the wet HF etch also passivates the Si surface with hydrogen and removes any surface states in the Si bandgap which are associated with the Si surface dangling bonds [4.21,22]. As such, the profiling technique, when used in conjunction with SCS is also applicable for measuring depth distributions of defect states within the bandgap in the near surface region.

The advantages of this depth profiling technique over conventional sputter depth profiling include no atomic mixing effects, uniform and controlled erosion of the sample surface, and no introduction of lattice damage to the sample Atom mixing effects result from the energetic interaction of a primary ion with the sample lattice atoms The principal type of atom mixing effect is cascade mixing [4.23] This effect occurs when large impact parameter collisions result between the primary ion and sample atoms, atoms are displaced from equilibrium positions and in turn strike neighbouring atoms which are also displace . The depth resolution of any technique using ion sputtering by energetic particles is limited by the depth with which the primary ion collision cascade produces atomic displacements within the sample surface. Under ideal conditions[4 23,24] this resolution is no less than 1nm. Nonuniform sputter erosion of a sample surface also affects the depth resolution by exposing various depths to the analyzing ion beam Finally, surface lattice damage as a consequence of ion sputtering produces electrically active defects [4.20] in the semiconductor bandgap and causes surface Fermi level pinning. The removal of surface Si layers via ozone oxidation plus wet oxide etching eliminates these artefacts induced by the sputtering process

The purpose of this work was to characterize the extent of residual surface damage on p-type Si(100) induced by a commercial RIE process The precise processing parameters were such that the damage produced was indicative of RIE surface damage These processing parameters were not the emphasis of investigation The characterization involved: (i) identification of surface contaminants, (ii) the depth distribution of such contaminants, (iii) the effect of defects on surface Fermi level pinning, and (iv) the depth distribution of such defects A second purpose was to remove the residual damage in a

controlled manner by a suitable processing technique.

The residual surface damage region of p-type Si(100) after RIE processing in a CHF_3/O_2 plasma consisted of a deposited fluorocarbon, polymeric film layer which was uniform in composition over its thickness, a thin (0.5nm) silicon carbide region with a fluorosilyl species layer of approximately 1nm in depth from the surface below the fluorocarbon film, and a high density of electrical defects producing surface Fermi level pinning. This residual damage was removed by controlled ozone oxidation followed by oxide stripping with an aqueous HF solution. The ultrashallow depth-profiling in conjunction with XPS and SCS contributed information which refined the model physical structure [4.11] of residual surface damage of silicon induced by fluorocarbon plasma RIE, as well as provided new information on the distribution of defects causing surface Fermi level pinning.

4.2 Experimental

The Si samples used in this work were supplied from Northern Telecom Electronics Ltd (Ottawa, Ontario, Canada). The samples were from a device quality 15.24cm diameter Si(100) wafer. A 20nm oxide was initially grown on the wafer which was then ion implanted with boron at 16keV to a dose of $1.6X10^{15}$ /cm^2. This p-type specimen was subsequently rapid thermally annealed (RTA) at 1323K (1050°C) for 30s to activate the dopant. The oxide was completely removed by reactive ion etching (RIE)

in a commercial instrument and the exposed silicon was subjected to reactive ion etching. The wafer was subsequently removed from the RIE chamber and exposed to air ambient.

Surface analysis by XPS was performed on a custom-built UHV system incorporating a Surface Science Laboratories SSX-100 concentric hemispherical (CHA) spectrometer (Chapter 3, section 3.5.7). Monochromatized Al Kα X-rays were used to eject photoelectrons from the surface of sample material. Survey spectra (0 to 100eV binding energy range) were acquired with an analysis spot size of 300μm diameter and a pass energy of 150eV. Spectra with a 20eV binding energy window were also acquired at a pass energy of 150eV for the different elements present. Such core-level spectra were used for quantifying the surface elements. Surface compositions were calculated using the theoretical photoelectron ionization cross sections due to Scofield [4.25]. Finally, high resolution core-level spectra (10eV and 20eV binding energy ranges) were accumulated at a pass energy of 50eV for increased spectral resolution to ascertain the various chemical states present. An iterative chi-squared peak-fitting program was used for curve-fitting the high resolution spectra. All peak-fitted spectra used a Shirley background form [4.26]. The total time of accumulation for each sample surface analyzed was usually 2h. All binding energies were referenced to a Ar^+ sputter-cleaned gold foil which was always present in the analysis chamber. The reference binding energy for the Au $4f_{7/2}$ core-level was 83.93eV. Surface charge spectroscopy (Chapter 3, section 3.5.6) was conducted on Si samples covered with an approximately 1nm thick SiO_2 insulating layer. A low energy (2eV) electron floodgun was used to charge the sample negatively, and high resolution Si2p and C1s core-level spectra were acquired before and after charging the sample. During analysis, the pressure in the XPS analysis chamber was typically in the range of

2.7 to $8x10^{-7}$ Pa (or 2 to $6x10^{-9}$ Torr).

The ultraviolet ozone oxidation was performed in a small tube reactor purged with oxygen gas bubbled through deionized water. An ultraviolet lamp was positioned approximately 2cm above the sample. The sample was then exposed to ozone generated from the interaction of the UV light and oxygen for approximately 20min. After ozone oxidation, the sample was removed and exposed to ambient before either loading into the XPS instrument for SCS analysis, or subjected to a wet aqueous hydrofluoric acid (HF) solution etch to remove the oxide grown, then XPS analysis was performed. For the ultrashallow depth profiling by XPS-SCS, the oxidation + wet oxide etch steps were repeated or cycled in order to consume controlled decrements (0.5nm) of Si.

4.3 Results and discussion

4.3.1 Fluorocarbon film characterization

Initial XPS analysis of the thin fluorocarbon film on the Si substrate is shown in Figure 4.1. This survey scan indicated the presence of carbon (C), oxygen (O), fluorine (F), and silicon (Si) from the core-level photoemission peaks and fluorine Auger peak structures. The surface atomic concentrations of C and F were the most abundant at approximately 50% and 34% atomic percent, respectively (see Table 4.1) for photoelectrons collected at a polar angle of 56° which corresponds to a sampling depth of approximately 3nm (see Chapter 3, section 3.5.4). The Si photoelectron peak

Figure 4.1 XPS survey scan of the RIE-processed Si surface

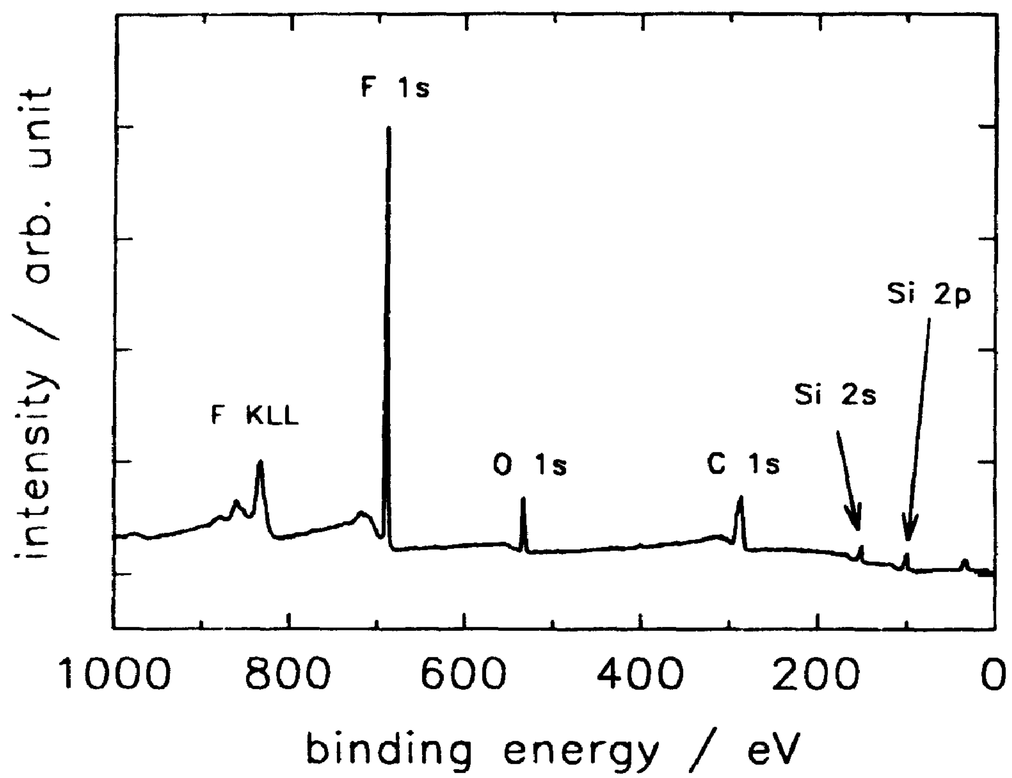
F 1s
F KLL
O 1s
C 1s
Si 2s
Si 2p
intensity / arb. unit
1000
800
600
400
200
0
binding energy / eV

Table 4.1 Surface compositions of Si after reactive ion etching in a CHF_3/O_2 plasma at various XPS polar angles corresponding to different sampling depths

Polar angle	Sampling depth	Surface atomic concentration			
		Silicon	Carbon	Oxygen	Fluorine
0°	6.0nm	18.2%	40.5%	12.3%	29.0%
16°	5.8nm	17.0%	41.0%	12.4%	29.5%
32°	5.1nm	13.9%	43.8%	11.7%	30.7%
48°	4.0nm	10.0%	46.7%	10.1%	33.3%
56°	3.4nm	07.0%	50.1%	09.0%	33.9%
63°	2.7nm	05.0%	50.6%	07.6%	36.8%

intensities due to the 2p and 2s core-levels were relatively weak compared to the C, O, and F spectral intensities (Figure 4.1). This indicates that there was sufficient residual contamination in the form of a deposited film overlayer to attenuate the Si substrate photoemission. From this initial surface analysis, it has been shown that the RIE process resulted in significant surface contaminants with very little Si detected at least in the top 3nm of the surface.

X-ray stimulated desorption of fluorine is known to occur [4.27] if the entire sample is exposed to intense X-rays. Hence, the effect of X-ray irradiation from the XPS instrument was examined. The change in surface composition of the fluorocarbon film on Si as a function of X-ray beam exposure time is shown in Figure 4.2. There were no significant reductions in the surface elements as a result of continuous X-ray beam irradiation up to a total of 7h at a polar photoemission angle of $\theta=55°$ (Figure 4.2). The system used for this work [4.17] incorporates a crystal monochromator producing a 300μm diameter X-ray spot at the sample surface. Such a system yields a low X-ray flux and minimal electron irradiation of the sample. This system was free from any excess radiation that might produce stimulated desorption, and the surface contaminants were stable over the XPS analysis time (typically 2h). Therefore, there was no instrumental influence on the analysis of the RIE-processed Si surface.

The high resolution C1s spectrum of Figure 4.3a shows the presence of at least 5 distinct peaks. This indicated that the surface carbon was in the form of hydrocarbons (CH), C-O groups on the C-C chain (COR) and fluorocarbon (CF_1, CF_2, and CF_3) species. These components were identified from signature spectra taken from the literature [4.12-14] and constitute a polymeric material. Because the Si peak intensities were attenuated

Figure 4.2 **Effect of 300μm diameter X-ray beam exposure of the surface contaminants on Si as a function of time (polar angle θ 55°)**

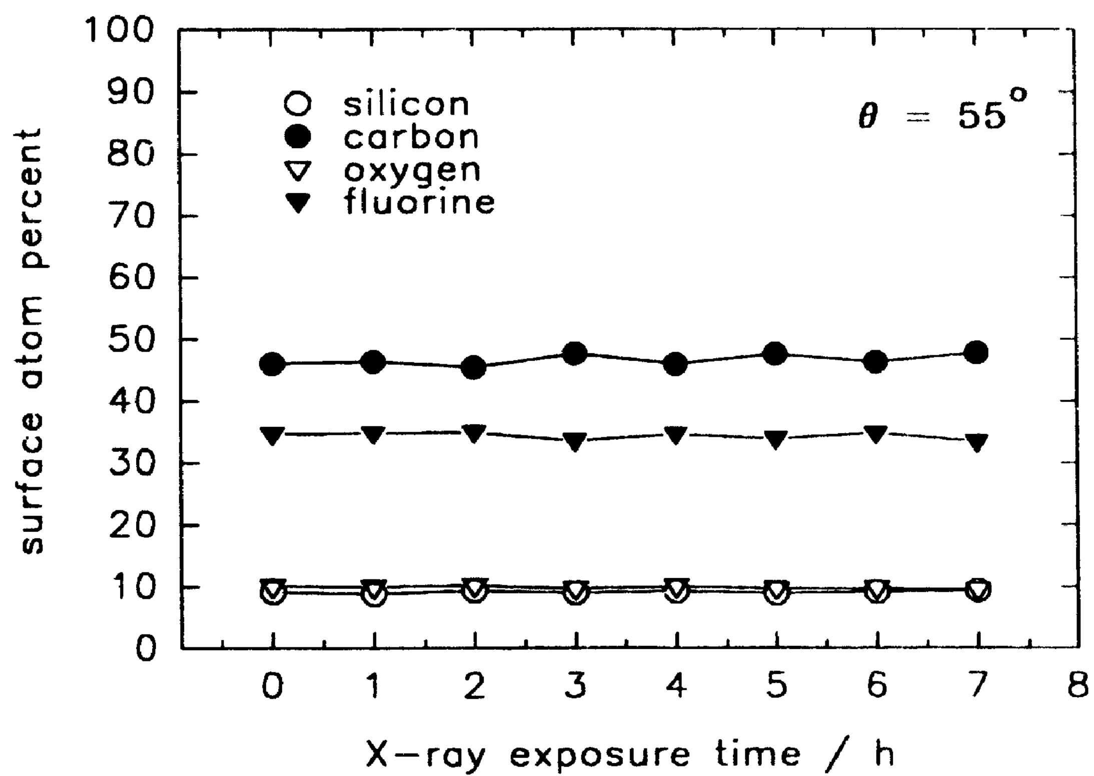

100
90
80
70
60
50
40
30
20
10
0
surface atom percent
silicon
carbon
oxygen
fluorine
θ = 55°
0
1
2
3
4
5
6
7
8
X-ray exposure time / h

Figure 4.3 XPS high resolution spectra corresponding to Figure 4.1; (a) C1s spectrum, and (b) Si2p spectrum (see Table 4.2 for actual binding energy positions for the Si-C,O,F species).

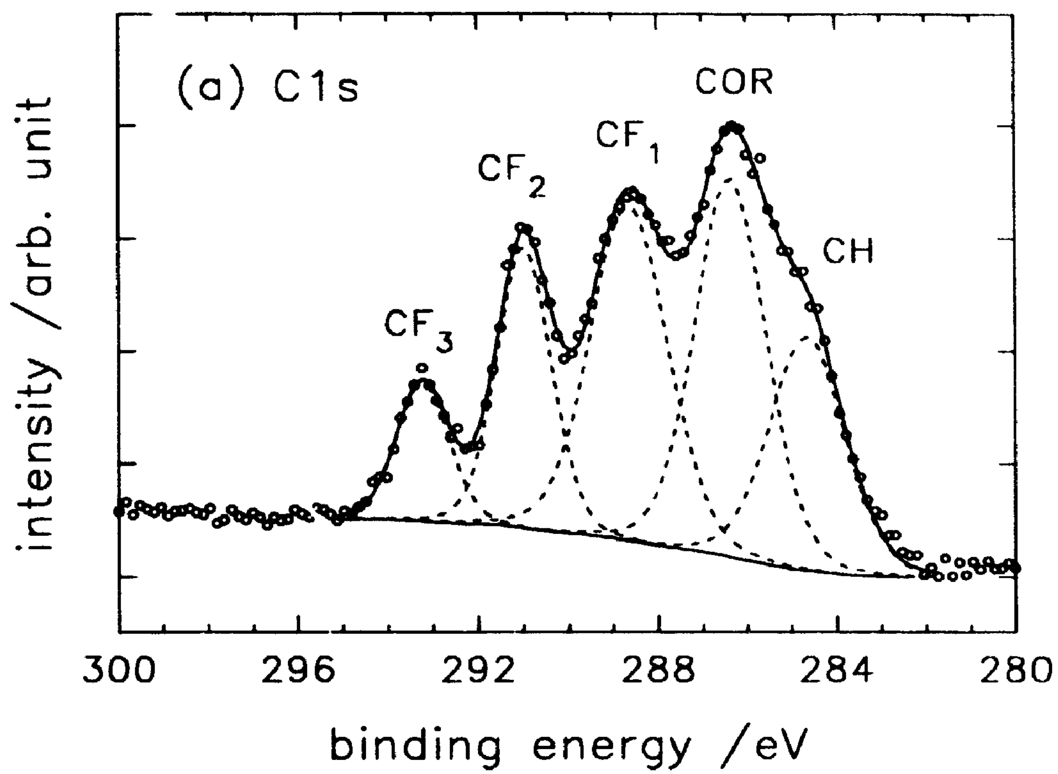
(a) C1s
COR
CF_1
CF_2
CF_3
CH
intensity /arb. unit
300
296
292
288
284
280
binding energy /eV

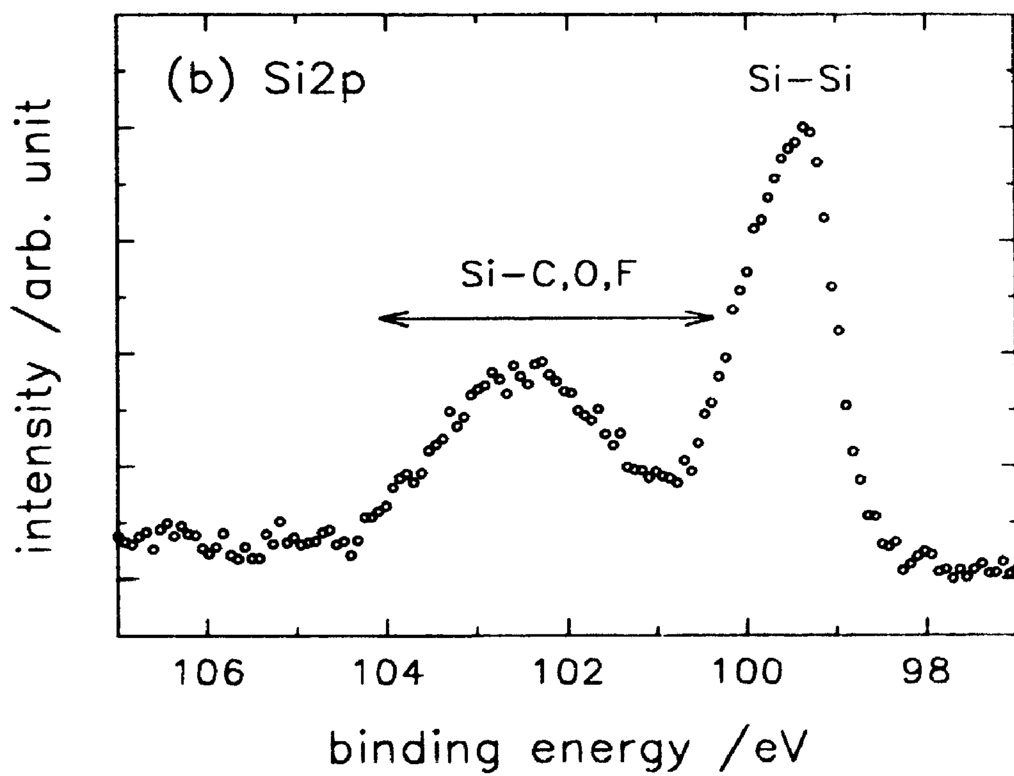
(b) Si2p
Si–Si
Si–C,O,F
intensity /arb. unit
106
104
102
100
98
binding energy /eV

appreciably (see Figure 4.1), the surface contaminants constituted a fluorocarbon layer deposited on the silicon.

The chemistry of the polymeric overlayer was more complex than common fluorocarbon polymers [4.29] such as polytetrafluoroethylene, which contains CF_2 groups, or polyvinylidene, which is comprised of CF_2 and CH_2 groups. This suggests a mixed fluorocarbon polymer composition for the deposited film. However, by varying the polar photoemission angle for angle-resolved XPS (see Chapter 3 section 3.5.4 on ARXPS), it was possible to describe qualitatively the overlayer chemical structure as a function of depth. The C1s and F1s spectra taken at a polar angle of 90° (greatest sampling depth of about 6.0nm) were almost identical to spectra acquired at 63° (shallower sampling depth of 2.7nm). Hence, the fluorocarbon film composition was quite uniform across its entire thickness, even though the film was chemically heterogenous.

The high resolution Si2p core-level spectrum (Figure 4.3b) shows the presence of the elemental Si peak near 99.3eV from the $2p_{3/2}$ and $2p_{1/2}$ spin-orbit pair, and a broad chemically shifted peak towards higher binding energy. The identity of this broad feature was assigned to a number of different silicon species. Table 4.2 lists the reported literature binding energies associated with the individual species. A fluorosilyl (SiF_n, n=1,2,3,4 species) reaction layer is present after RIE with fluorine-based feedgases [4.14-16,4.27,4.30] and the present results support this finding.

The presence of oxygen at the film-substrate interface was identified from the ARXPS analysis with the surface concentrations listed in Table 4.1. This interfacial oxygen pointed to SiO_2 and $Si\text{-}O_m$ ($m<2$) species (silicon suboxides) as probable components contributing to the broad peak seen in the Si2p spectrum. Because the

Table 4.2 Assignment of core-level binding energies for C1s, Si2p, O1s, and F1s

Core-level	Peak assignment	Binding energy position	
		experimental	literature
C1s	CF_3	293.1eV	293 4eV[a]
	CF_2	290 9eV	291 2eV[a]
	CF	288.6eV	288 8eV[a]
	COR	286.3eV	286 5eV[a]
	C-C,C-H	284.6eV	284 6eV[a]
	C-Si	283.5eV	283 5eV[a]
Si2p	Si-Si	_____	99 3eV[b]
	Si-C	_____	101 3eV[b]
	Si-F_1	_____	100 4eV[c]
	Si-F_2	_____	101 5eV[c]
	Si-F_3	_____	102 6eV[c]
	Si-F_4	_____	103 7eV[c]
	Si-O_x $(1<x<2)$	_____	102 8eV[b]
F1s	F-C	688.0eV	688 2eV[a]
	F-Si	686.4eV	686 6eV[d]
O1s	O-H	5·2.2eV	
	O-C	532.5eV	
	O-Si	534.5eV	532 7eV[a]

[a] C. Cardinaud, A. Rhounna, G Turban, B Grolleau, J. Electrochem. Soc., 135(6), 1472, 1988

[b] G.J. Coyle, G.S. Oehrlein, Appl. Phys. Lett., 47(6), 604, 1985

[c] F.R. McFeely, J.F. Morar, N.D. Shinn, G. Landgren, F J. Himpsel, Phys Rev B, 30, 764, 1984

[d] G.S. Oehrlein, J. Vac. Sci. Technol., A11(1), 34, 1993.

sample wafers were exposed to air after removal from the RIE instrument chamber, the inevitable oxidation of the substrate silicon occurred. This Si oxidation has been reported [4.11] to develop after only 20min of air exposure. Such substrate oxidation was believed to be caused by [4.11] oxygen permeation through the fluorocarbon film.

Silicon carbide (SiC) species are known to form in a silicon-containing compound layer below the fluorocarbon film [4.15] when a fluorocarbon feedgas is used for RIE. The binding energy peak position corresponding to assignment of SiC species is shown in Table 4.2. However, based solely on the Si2p spectrum, it was difficult to assign peaks unambiguously to fluorosilyl, oxide and carbide species because of the over-lapping binding energies of these peaks. The presence of these surface Si-C,O,F species is plausible because a CHF_3/O_2 plasma was used for RIE, and air oxidation was unavoidable. In addition, the XPS survey scan of Figure 4.1 shows the identification of these surface elements.

The F1s spectrum showed a single symmetric peak at about 688eV binding energy with a full-width-at-half-maximum (FWHM) of 1.9eV. The binding energy position was similar to that for fluorocarbons [4.29]. Hence, this single peak was assigned as fluorine bonded to carbon in agreement with the C1s spectrum. The F1s core-level spectrum appeared to be insensitive to chemical shifts associated with carbon either singly- or multiply-bonded to fluorine. This could be due to the mixture of C-F species (Figure 4.3a).

The O1s spectrum showed two component peaks. The lower binding energy peak at 532.3eV was due to hydrocarbon (CH) and COR species in agreement with the C1s spectrum, while the higher binding energy peak was assigned to Si-O chemical groups.

This latter assignment was also consistent with the Si2p spectrum The F1s and O1s spectra are discussed further in the section 4.3.2.

The thickness of this fluorocarbon deposited film layer is an important property of the overlayer in addition to its chemical composition. By varying the RIE process parameters, the measurement of film thickness may be a useful guide to minimizing the extent of residual surface damage. In order to estimate the thickness of the film, a uniform overlayer model [4.31] was assumed, i.e., a continuous and discrete overlayer exists with a constant composition throughout the overlayer By assuming that the photoelectron intensity is exponentially attenuated below the surface by inelastic scattering, and using a constant value of 3.0nm for the inelastic mean free path (IMFP) of the photoelectrons [4.32,4.33], the thickness of the fluorocarbon overlayer was calculated from the following expression [4.31]:

$$d\ (nm) = \lambda \cos\theta \left(\ln\{[C+O+F]/Si + 1\} \right)$$

where d is the film thickness, θ is the polar angle of photoemission, λ is the inelastic mean free path of the photoelectrons, and $[C+O+F]/Si$ is the composition ratio of carbon, oxygen and fluorine in the overlayer to silicon in the substrate, as determined by XPS (see Table 4.1). A plot of $\ln([C+O+F]/Si+1)$ versus $1/(\lambda\cos\theta)$ provided a slope corresponding to an approximate film thickness of d = 4.3nm (see Figure 4 4a)

Figure 4.5b shows a comparison between the uniform overlayer model and the experimental data points for a film thickness of 4.3nm There was reasonable agreement between the model and the data. The error associated with the polar angle was largely

Figure 4 4 The uniform overlayer model; (a) plot of $\ln([C+O+F]/[Si]+1)$ versus $1/(\lambda cos\theta)$, the slope corresponding to film thickness was determined by linear regression to be d=4.3nm, and (b) plot of $[C+O+F]/[Si]$ versus polar angle θ, comparison between experimental data and the uniform overlayer model.

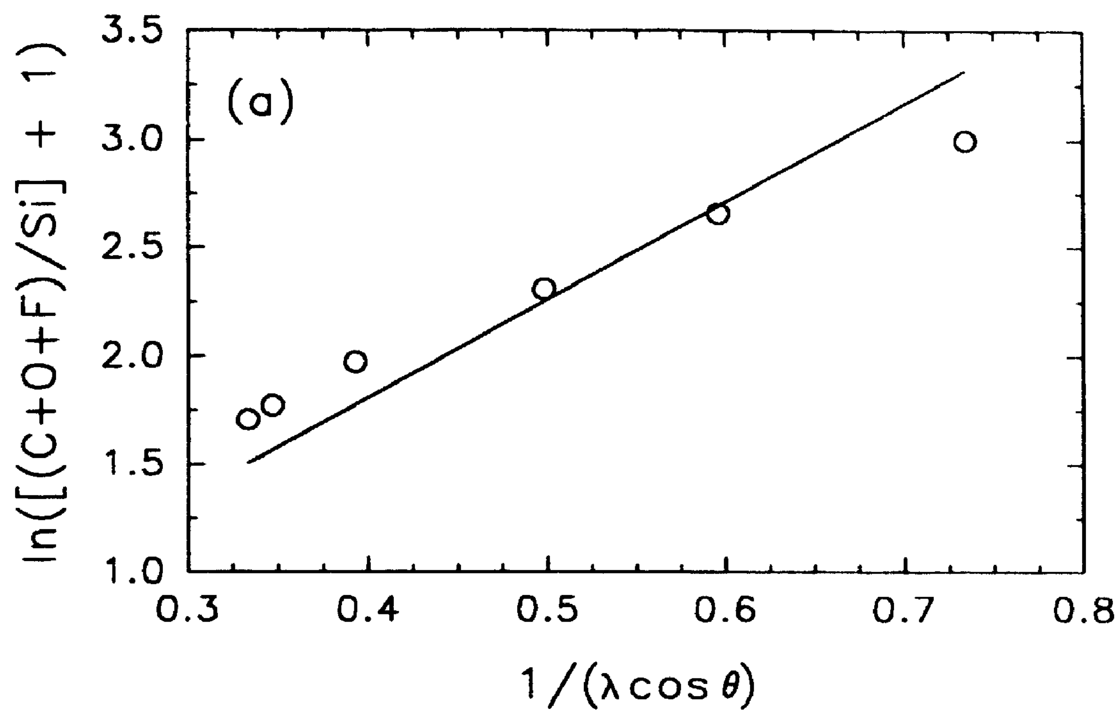
(a)
ln([(C+O+F)/Si] + 1)
1/(λ cos θ)

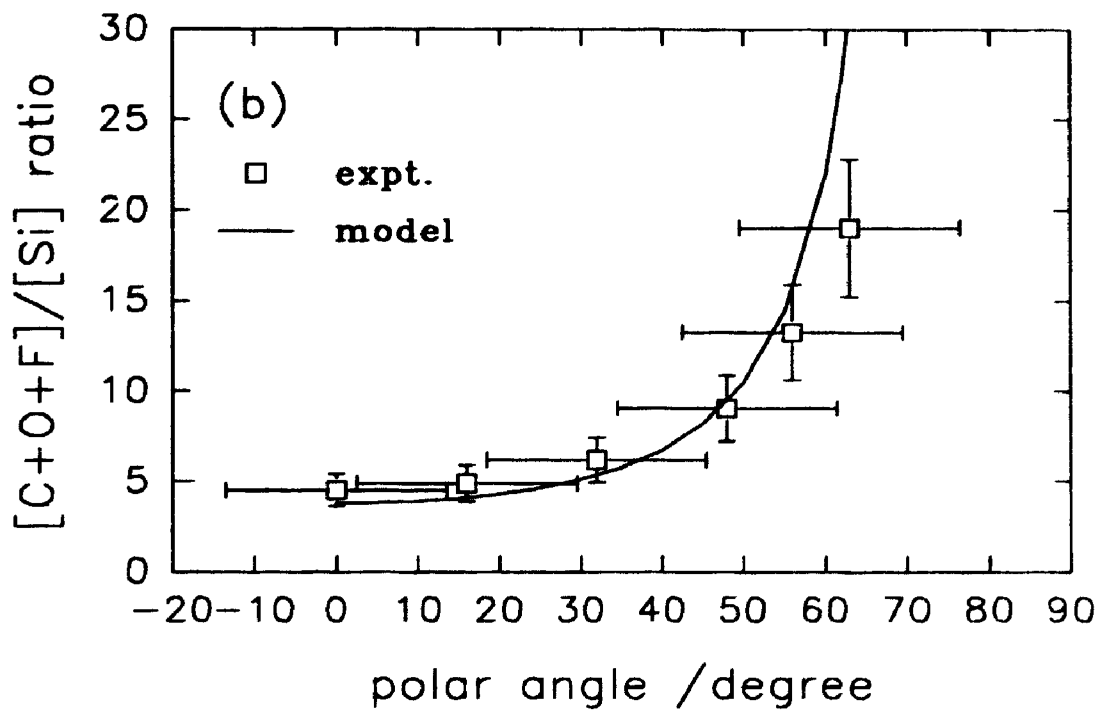
(b)
expt.
model
[C+O+F]/[Si] ratio
polar angle /degree

due to the solid acceptance angle of the detector of 27°, while the total uncertainty from the composition ratio was approximately 10% [4.34]. The value for the film thickness was dependent on the assumptions made in the model. The IMFP of the various photoelectrons are actually not all equal to 3.0nm. As well, the overlayer composition may also vary at the film-substrate interface as well as near the film surface. As discussed previously, angle-dependent analysis of the surface compositions indicated that the oxygen present was at the film-substrate interface due to the larger concentrations detected near 0° polar angle (Table 4.1).

4.3.2 Ulrashallow chemical species depth-profiling

The fluorocarbon overlayer was completely removed after the first treatment of UV/O_3 exposure (20min) and wet oxide etch (cycle 1 in Figure 4.5). This was shown by a drastic reduction in the amounts of surface C, F, and O relative to Si. In addition, the C1s spectrum of Figure 4.5 indicated the absence of fluorocarbon-type species associated with the overlayer. The dominant peak at 284.6eV binding energy was attributed to adventitious carbon present after air exposure of the samples following each wet HF etch treatment. The spectrum also revealed the presence of a second major component at approximately 283.5eV binding energy corresponding to silicon carbide [4.15]. Hence, below the fluorocarbon overlayer was a SiC-containing reaction layer induced by the RIE process. The C1s spectra also indicated two minor components after cycle 1 and 2 of ozone oxidation plus oxide stripping. These two C-O peaks towards higher binding energy were identified [4.29] as COR and carboxyl (COOH) species formed after the wet etch and deionized water rinse. It is also possible that the COR peak seen after cycle 1

Figure 4.5 C1s spectra of the fluorocarbon film on Si after ultra-shallow depth-profiling.

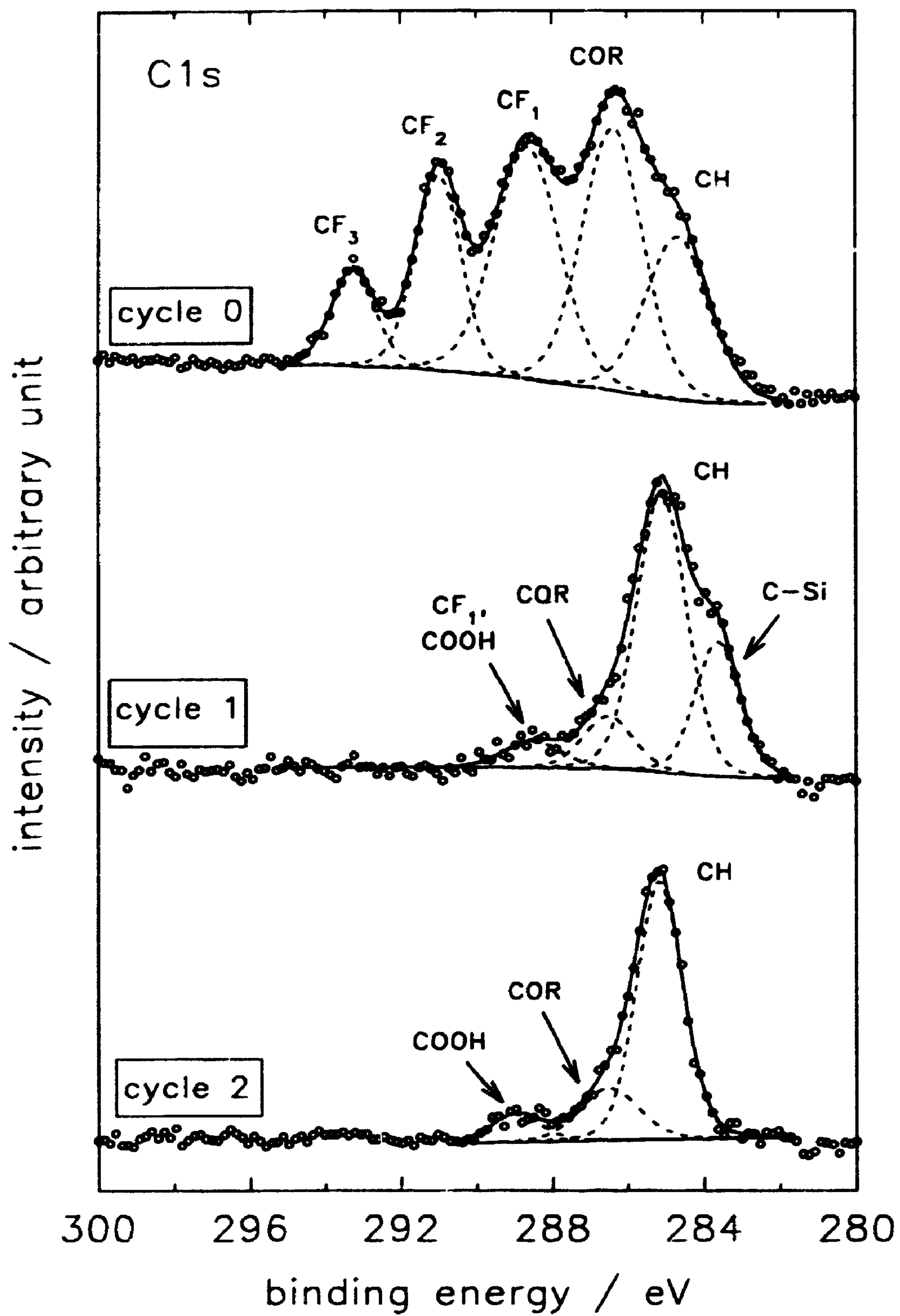
C1s
COR
CF_1
CF_2
CH
CF_3
cycle 0
CH
CF_1,
COOH
COR
C–Si
cycle 1
CH
COR
COOH
cycle 2
intensity / arbitrary unit
300
296
292
288
284
280
binding energy / eV

was due to some CF_1 species because of its binding energy position and also from the detection of a relatively small amount of fluorine on this surface

After the second treatment of oxidation and wet etching, the SiC species was not detected by XPS. This suggests that the carbide layer was confined to a depth of 0.5nm since this amount of Si was removed after each oxidation/wet etch cycle. Conventional depth-profiling with energetic (a few keV) ion sputtering causes [4.35] "ion mixing" and surface damage on a scale greater than 0.5nm because of the collisional cascades from the physical sputtering process. Such ion beam-induced artefacts alter the chemical structure during sputter depth-profiling with either XPS, Auger electron spectroscopy (AES) or secondary ion mass spectrometry (SIMS) and render the identification of the SiC species impossible. However, with this ultrashallow depth-profiling technique, the controlled erosion of 0.5nm Si was routinely accomplished

The Si2p spectrum taken prior to any depth-profiling was overlayed with spectra after the first two oxidation/wet etch cycles (Figure 4.6). The peak profile was partitioned into a major component due to elemental Si near 99.5eV and a broad, minor component towards higher binding energy from the various Si compounds in the reaction layer. The binding energy range for SiC, SiO, SiO_2, SiF, SiF_2, and SiF_3 are marked in the figure and listed in Table 4.2.

After the first two oxidation/HF etch cycles, the amounts of Si compounds were reduced. A comparison of the Si2p spectra allowed the estimation of the thickness of the Si reaction layer removed by the first oxidation/HF etch cycle. This thickness was about 1nm (or equivalent to 0.6nm of Si). This estimation assumed that the Si atom density in this contaminated Si layer was $3\times10^{22}/cm^3$ (c.f. $5\times10^{22}/cm^3$ Si, and $2.2\times10^{22}/cm^3$ in SiO_2

Figure 4 6 Si2p spectra of the fluorocarbon film on Si after ultra-shallow depth-profiling.

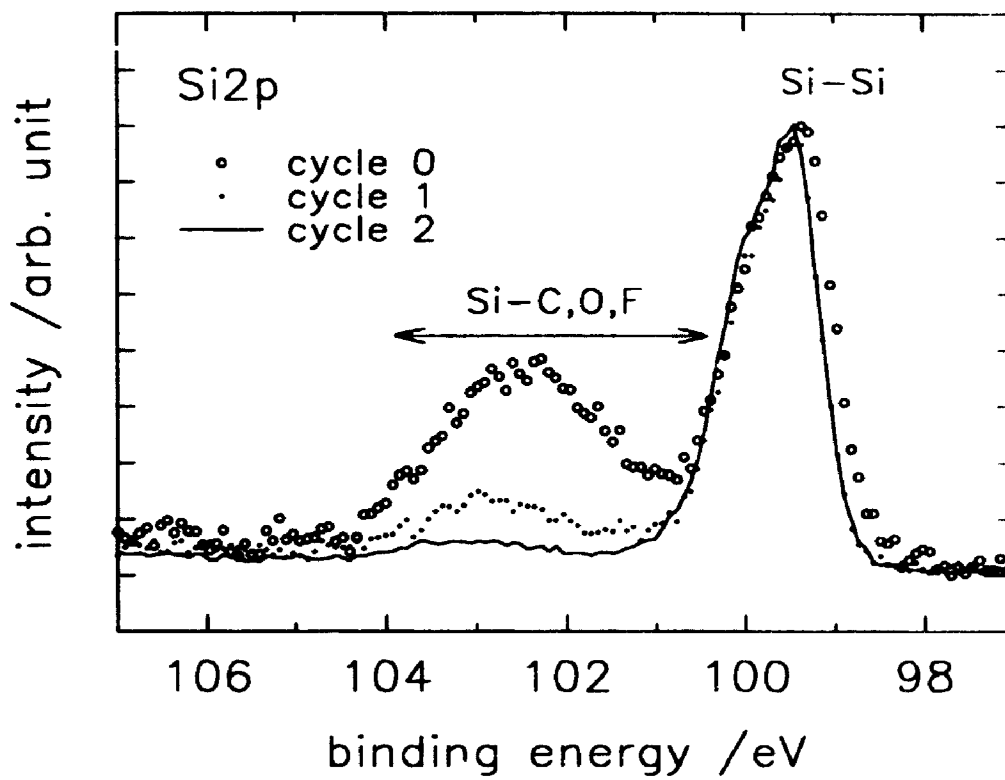
Si2p
Si–Si
cycle 0
cycle 1
cycle 2
Si–C,O,F
intensity /arb. unit
106
104
102
100
98
binding energy /eV

). Also, the Si2p photoelectron IMFP in the contaminated layer and bulk Si were assumed to be 3.7 and 3.2nm, respectively (data calculated for SiO_2 and Si with the Bethe equation parameterized by Tanuma et al [4.32,33]). Since the amounts of oxides/fluorides before the first oxidation/HF etch cycle were even greater than the amount of oxide formed by treating a clean Si surface with just one oxidation cycle, the contaminated Si removed in this first oxidation/HF etch cycle was likely due to the wet HF etching of the RIE formed oxides/fluorides instead of ozone oxidation.

The atomic concentration of F dropped from 41% to 6% with the application of the first oxidation/etching cycle. This clearly shows that the contaminations induced by RIE became minor components embedded in silicon within the remaining damaged region. Accordingly, the oxidation/etching rate of this remaining damaged region should be approaching that of pure Si, and the ultrashallow depth-profiling technique of removing 0.5nm of Si per cycle will apply well in the analysis of this modified Si region.

Figure 4.7 represents the F1s photoelectron spectra of the fluorocarbon-covered silicon induced by RIE (cycle 0) and after one cycle of ozone oxidation plus oxide stripping. The single peak profile at 688eV due to fluorine bonded to carbon from the deposited film (see Table 4.1) was shifted to lower binding energy after removal of the film. This lower binding energy peak at 686.4eV was assigned to a fluorine bonded to silicon environment [4.27]. Such peak assignments are listed in Table 4.1 and were in agreement with published data [4.13,27]. Subsequent cycles to remove successive layers (0.5nm) of silicon produced a significant reduction in spectral intensity which corresponded to the removal of the Si-F species. After 3 cycles, the Si-F species were not present within the detection limits of the XPS instrument. The corresponding Si2p

Figure 4.7 F1s spectra of the fluorocarbon film on Si after ultra-shallow depth-profiling.

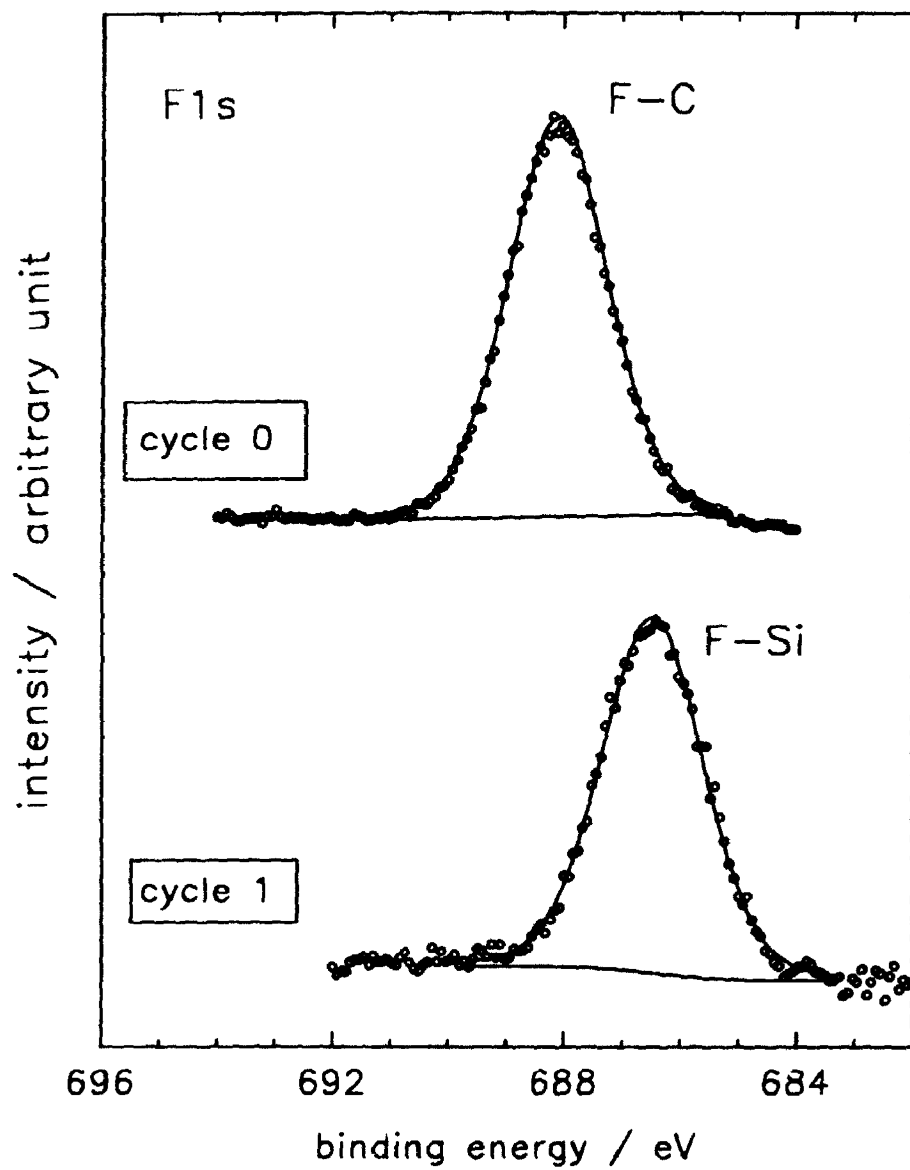
F1s
F-C
F-Si
cycle 0
cycle 1
intensity / arbitrary unit
696
692
688
684
binding energy / eV

spectra (Figure 4.6) was consistent with this observation of Si-F species removal This indicates that the extent of Si-F species depth distribution was approximately 1 5nm

The O1s spectra corresponding to Figure 4.7 is shown in Figure 4 8 Before ozone oxidation and oxide stripping, two peak components may be identified The peak at 532.2eV was tentatively assigned to oxygen bonded to carbon and oxygen bonded to hydrogen in agreement with the COR and CH species identified from the C1s spectrum of Figure 4.5. The minor peak component at approximately 534.5eV binding energy was assigned to oxygen bonded to silicon based on reference spectra of silicon dioxide This O-Si species identification was consistent with the interfacial oxygen found from angle-dependent XPS (Table 4.1) and from the oxidation of the Si substrate after air exposure For the case after one cycle of ozone oxidation plus oxide stripping, a single peak at 532.5eV was observed. This peak was assigned to oxygen bonded to hydrogen as well as oxygen bonded to carbon but not from the fluorocarbon film because this film was removed after one cycle. This O1s peak was from the deionized water rinse after wet HF chemical etching to remove the silicon dioxide leaving residual COR and hydroxyl species which was also seen from the C1s spectra of Figure 4.5.

4.3.3 Surface Fermi level pinning and damage removal

One main concern in the study of RIE-induced residual damage was how much Si had to be removed before the substrate can be used for subsequent fabrication For many fabrication requirements, the density of the residual defect states in the substrate has to be low enough so that a surface band bending condition can be induced by a small applied voltage [4.36]. It is in this context that the SCS analysis became useful In this

Figure 4.8 O1s spectra of the fluorocarbon film on Si after ultra-shallow depth-profiling.

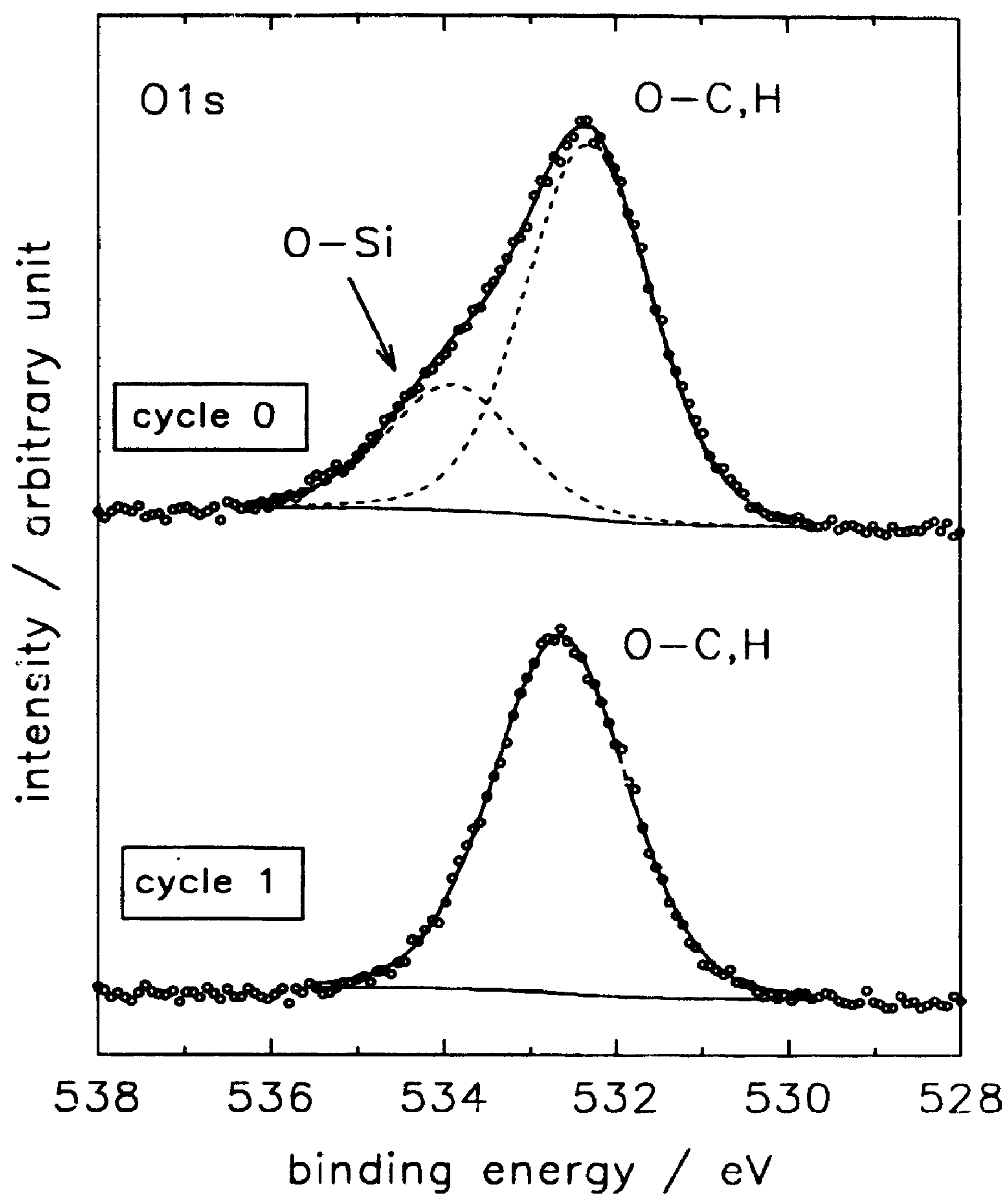
O1s
O–C,H
O–Si
cycle 0
O–C,H
cycle 1
intensity / arbitrary unit
538
536
534
532
530
528
binding energy / eV

SCS analysis [4.37], XPS was used to measure the surface potentials [4.38] of the SiO_2 on Si samples after each ozone oxidation treatment in the depth profile. This surface potential estimation involved the charging of the sample surface with a low energy electron flood gun unit within the XPS system (see Chapter 3). Since the oxide thickness and quality were reproduced at each oxidation cycle, a consistent change of the dielectric surface potential at 2eV could be applied to every SiO_2/Si sample. As such, the measurement of the corresponding change in the semiconductor surface potential after each oxidation/wet etch cycle gave some qualitative information on the density of residual defect states in the remaining Si near the SiO_2/Si interface.

The SCS results collected from the RIE processed sample in this manner are summarized in Figure 4.9. The sample after the first oxidation cycle showed a firmly pinned Fermi level, i.e. there was no detected change in surface potential, i.e. no changes in binding energy position (see Chapter 3, section 3.5.6) as a result of charging the sample negatively with low energy electrons. This suggests that the density of impurity states or defect states was still very high in the remaining Si surface. After each successive cycle, the change in semiconductor surface potential increased almost asymptotically to a value near 0.4eV. This points to the fact that the density of residual defect states near the oxide/semiconductor interface was being reduced with successive cycles. There is a correlation between the RIE-induced surface damage and electrical properties such as leakage current [4.39,40]. However, the removal of this surface damage by ultra-shallow depth-profiling and the monitoring of the electrical properties by SCS in this work is perhaps the most direct analysis.

Although the Fermi level was unpinned after 2nm of Si was removed, the surface

Figure 4.9 Change in semiconductor surface potential corresponding to changes in core-level binding energy as measured by surface charge spectroscopy at successive depths of 0.5nm.

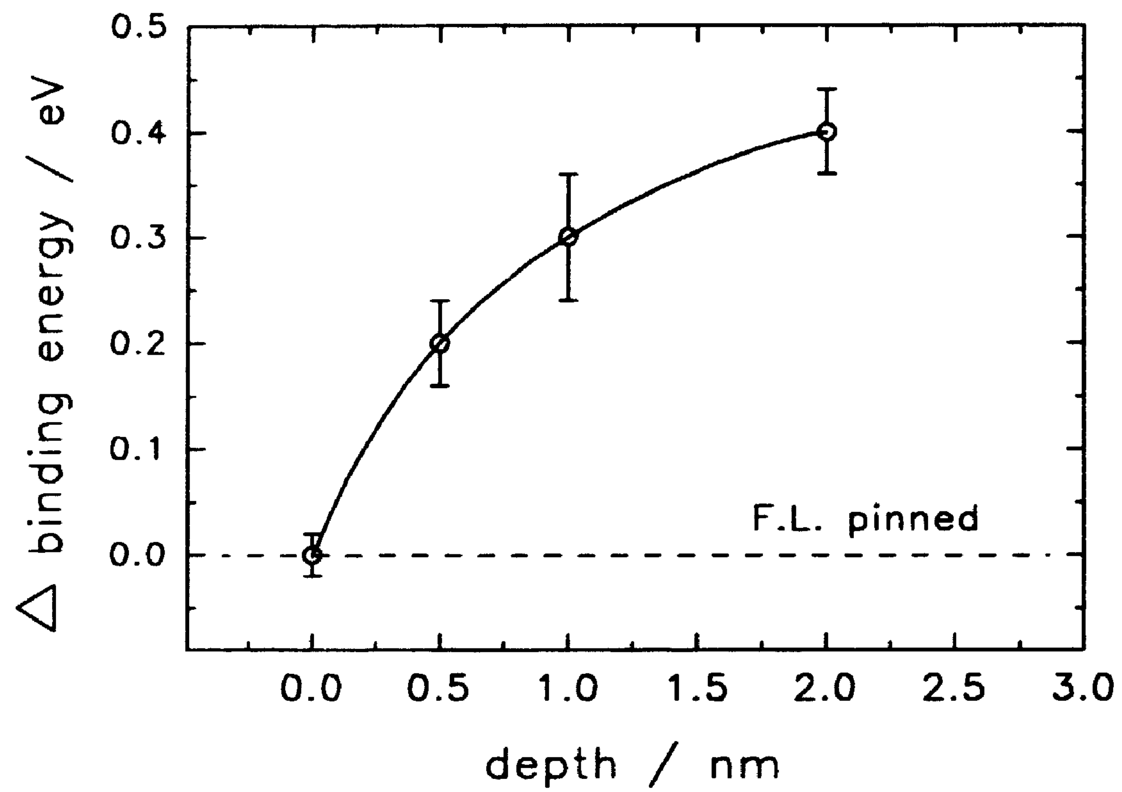

△ binding energy / eV
0.5
0.4
0.3
0.2
0.1
0.0
F.L. pinned
0.0
0.5
1.0
1.5
2.0
2.5
3.0
depth / nm

Fermi level position was found to be about 0.7eV above the valence band maximum which was greater than the expected value of less than 0.1 eV for heavily doped p-type Si(100). Previous data [4.41] on hydrogen incorporation into p-type Si suggests that hydrogen could have been driven into the near surface region of the RIE-processed Si and passivated the boron dopant. In fact, a previous SIMS depth-profiling study [4.42] shows the presence of hydrogen in the top 50nm of the Si after RIE. In addition, the wet HF etch treatment is known [4.43] to form a hydrogen-boron-silicon (H-B-Si) complex which deactivates the dopant. Fortunately, this boron passivated by hydrogen can be reactivated with a mild annealing at 200°C, a treatment which dissociates the H-B-Si complex and drives the hydrogen released either to the surface or to the bulk.

It is known that the RIE damage cannot be removed by thermal oxidation [4.40] because this oxidation process drives a significant degree of the damage into the bulk Si, i.e. thermal diffusion/migration of defects at the Si surface into the bulk. Because the present oxidation/etching procedure was performed at room temperature, process induced defect migration would be minimal. This means that the RIE-induced damage at the surface is removed during ozone oxidation. Hence, the UV/O_3 oxidation process is attractive as a damage removal technique because it does not enhance surface defect mobility into the bulk.

In summary, the results from this chapter can be used to provide improved and new knowledge of the model proposed by Oehrlein and coworkers [4.11] for the physical structure of the surface residual damage region induced by fluorocarbon plasma RIE processing of silicon. Figure 4.10 illustrates the model in the top half of the diagram, and the bottom diagram shows effectively the contribution of the work conducted in this

Figure 4.10 Schematic diagram of the model physical structure of silicon surface residual damage induced by fluorocarbon plasma RIE (from Oehrlein and Lee [4.11]), and the information provided from this thesis is shown in the lower diagram.

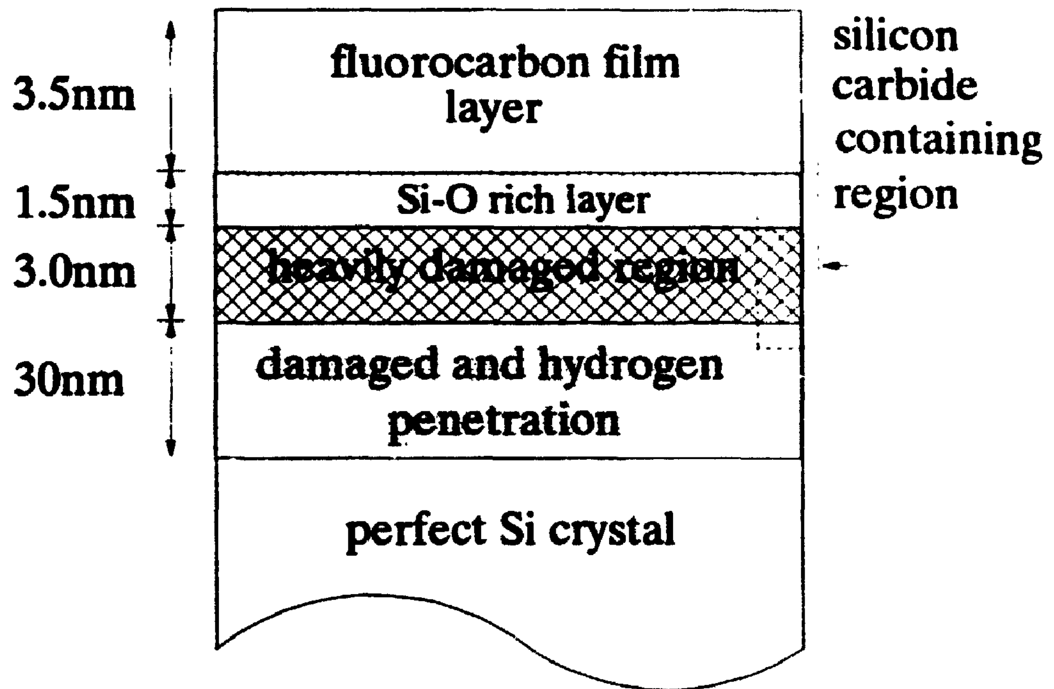
3.5nm
1.5nm
3.0nm
30nm
fluorocarbon film layer
Si-O rich layer
heavily damaged region
damaged and hydrogen penetration
perfect Si crystal
silicon carbide containing region

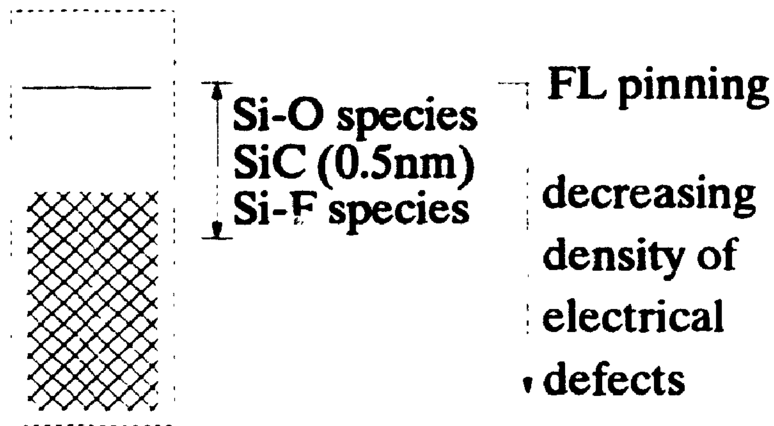
Si-O species
SiC (0.5nm)
Si-F species
FL pinning
decreasing density of electrical defects

thesis The actual depths labelled in the model structure are similar to this work, however it was not expected to be the same because of different fluorocarbon feedgas (CF_4/H_2 versus CHF_3/O_2 for this thesis) and processing parameters. Nevertheless, the model's different surface regions of damage resulting from RIE are consistent with the work discussed in this thesis. The fluorocarbon film covers a silicon bonded to oxygen layer with a heavily damaged region. SiC is present in the heavily damaged region, however, the depth distribution was not determined. The work in this thesis shows that the SiC species were confined to a shallow depth of 0.5nm with a Si-F reaction layer also present to a depth of 1.5nm. The identification of this Si-F layer (heavily damaged region in the model) from the ultrashallow depth-profiling was not seen in the model. In addition, the effect of defect states in the heavily damaged region on surface Fermi level pinning was not reported in the proposed model.

4.4 Conclusions

The fluorocarbon plasma reactive ion etching of p-type Si(100) induced residual surface damage in the form of a fluorocarbon deposited film layer approximately 4.3nm in thickness. This film was found to be uniform and discrete with little changes in chemical composition. Beneath this deposited film was a reaction layer containing silicon suboxides, silicon carbide and Si bonded to F (fluorosilyl) species. The SiC was found to be confined to a depth of 0.5nm while the fluorosilyl layer extended to approximately

1.5nm below the fluorocarbon film. The physically damaged Si substrate below the film was found to have a significant density of defect states which resulted in surface Fermi level pinning (when the sample was charged negatively by 2eV flooding electrons) The removal of approximately 2nm of this damaged silicon resulted in the release of the pinning. Hence, the density of defect states was reduced with the removal of the disordered surface. The ozone oxidation process provides a room temperature oxidation process which gives the removal of the fluorocarbon film and controlled erosion of silicon layers with a depth resolution of 0.5nm. Such a process is suitable as a post-RIE treatment to remove the residual surface damage because of its depth control and because there is no redistribution or introduction of defects.

REFERENCES

4.1 J.W. Coburn, H.F. Winters, J. Vac. Sci. Technol., 16, 391, 1979.

4.2 L. Ephrath, J. Electrochem. Soc., 126, 1419, 1979.

4.3 H.W Lehmann, R. Widmar, J. Vac. Sci. Technol., 15, 319, 1978.

4.4 G.S. Oehrlein, R.M. Tromp, J.C. Tsang, Y.H. Lee, E.J. Petrillo, J. Electrochem. Soc., 132(6), 1441, 1985.

4.5 S.J Fonash, Solid State Technol., 28(1), 150, 1985.

4.6 D. Bollinger, S. Ida, O. Matsumoto, Solid State Technol., 27(5), 111, 1984.

4.7 H.F Winters, J.W. Coburn, Surf. Sci. Rep., 14, 161, 1992.

4.8 P.A.F. Meharg, PhD. thesis, University of British Columbia, 1992.

4.9 G.S. Oehrlein, R.M. Tromp, Y.H. Lee, E.J. Petrillo, Appl. Phys. Lett., 45, 420, 1984.

4.10 K Wittmaack, in Practical Surface Analysis, Volume 2, edited by D. Briggs, and M.P. Seah, J. Wiley & Sons, Chichester, 105, 1992.

4.11 G.S Oehrlein, Y.H. Lee, J. Vac. Sci. Technol., A5(4), 1585,1987.

4.12 D.J Vitkavage, T.M. Mayer, J. Vac. Sci. Technol., B4(6), 1283, 1986.

4.13 C Cardinaud, A. Rhounna, G. Turban, B. Grolleau, J. Electrochem. Soc., 135(6), 1472, 1988.

4.14 G.E Potter, G.H. Morrison, P.K. Charvat, A.L. Ruoff, J. Vac. Sci. Technol., B10(6), 2398, 1992.

4.15 G.J Coyle, G.S. Oehrlein, Appl. Phys. Lett., 47(6), 604, 1985.

4.16 J.H Thomas III, X.C. Mu, S.J. Fonash, J. Electrochem. Soc., 134(12), 3122, 1987.

4.17 R.L. Chaney, Surf. Interface Anal., 10, 36, 1987.

4.18 W.M. Lau, Appl. Phys. Lett., 54, 338, 1989.

4.19 W.M. Lau, X-W Wu, Surf. Sci. 245, 345, 1991

4.20 W.M. Lau, L. Huang, W.H. Chang, M. Vos, I.V Mitchell, Appl Phys. Lett., 64(1), 1993.

4.21 L. Huang, W.M. Lau, Appl. Phys. Lett., 60, 1108, 1992

4.22 L. Huang, W.M. Lau, J. Vac. Sci. Technol., A10, 812, 1992

4.23 C.W. Magee, R.E. Honig, Surf. Interface Anal., 4(2), 35, 1982.

4.24 I.S.T. Tsong, J.R. Monkowski, D.W. Hoffman, Nucl. Instrum. Method., 182, 237, 1981.

4.25 J.H. Scofield, J. Electron Spectrosc. Relat. Phenom., 8, 129, 1976

4.26 D.A. Shirley, Phys. Rev. B, 5, 4709, 1972.

4.27 G.S Oehrlein, J. Vac. Sci. Technol., A11(1), 34, 1993.

428 G.S. Oehrlein, R.M. Tromp, J.C. Tsang, Y.H. Lee, E.J. Petrillo, J Electrochem Soc., 132, 1441, 1985.

4.29 A. Dilks, in Electron Spectroscopy: Theory, Techniques, and Applications, Volume 4, edited by A.D. Baker, C.R. Brundle, Academic Press, London, 277, 1981

4.30 F.R. McFeely, J.F. Morar, N.D. Shinn, G. Landgren, F J. Himpsel, Phys Rev B., 30, 764, 1984.

4.31 P.F.A. Meharg, E.A. Ogryzlo, I. Bello, W.M. Lau, J Vac Sci. Technol, A10(4), 1358, 1992.

4.32. S. Tanuma, C.J. Powell, D.R. Penn, Surf Interface Anal, 17, 911, 1991

4.33 S. Tanuma, C.J. Powell, D.R Penn, Surf. Interface Anal, 17, 927, 1991

4.34 T A. Carslon, Surf. Interface Anal., 4(4), 125, 1982.

4.35 S. Hofmann, in SIMS III, A. Benninghoven, edited by J. Giber, J. Laszlo, M. Riedel, H.W. Werner, Springer-Verlag, Berlin, 186, 1982.

4.36 S.M. Sze, Physics of Semiconductor Devices, Wiley-Interscience, New York, 1981.

4.37 W.M. Lau, Appl. Phys. Lett., 54(4), 338, 1987.

4.38 R.W. Grant, E.A. Kraut, S.P. Kowalczyk, J.R. Waldrop, J. Vac. Sci. Technol., B1 (2), 320, 1983.

4.39 I.H. Connick, A. Battacharyya, K.N. Ritz, W.L. Smith, J. Appl. Phys., 64(4), 2059, 1988.

4.40 R.G. Frieser, F.J. Montillo, N.B. Zingerman, W.K. Chu, S.R. Mader, J. Electrochem. Soc., 130(11), 2237, 1983.

4 41 S.J. Jeng, G.S. Oehrlein, G.J. Scilla, Appl. Phys. Lett., 53(18), 1735, 1988.

4 42 G.S. Oehrlein, G.J. Scilla, S.J. Jeng, Appl. Phys. Lett., 52(11), 907, 1988.

4.43 L.J. Huang, W.L. Lau, Appl. Phys. Lett., 60, 1108, 1992.

CHAPTER 5

SURFACE REACTIONS INDUCED BY F^+ ION BOMBARDMENT

5.1 Introduction

Dry etching of silicon (Si) by a fluorine-based plasma is one of the most important materials tailoring techniques in the fabrication of microelectronic devices [5.1-2] The fluorine (F) plasma produces a variety of energetic, reactive ions, neutrals and radicals which all simultaneously impinge on the Si material being etched. As a result, the etching mechanisms are extremely complicated with numerous models hypothesized [5.3-7]. A tremendous experimental and theoretical effort has been expended [5.3-33] in gaining an insight into the reactive F etching process, but a comprehensive understanding has been elusive. It is generally believed that atomic F is the primary reactive species in F-based plasma etching of Si [5.3-5,7], and the energies of the F^+ ions, radicals and neutrals are typically found from a few hundreds of electronvolts of kinetic energy down to almost zero energy [5.33]. The energetic reactive particles impinge upon the surface of the material to be etched and form chemical reaction species which are subsequently desorbed into the gas phase. The incorporation of the etched material elements as part of the gas phase volatile reaction products constituents the erosion process (dry reactive etching).

Over recent years, the reactions of XeF_2, F_2, and atomic F with the Si(100), Si(111), and amorphous Si have been studied as simulated model systems for the F-Si

interactions found in the actual plasma etching process [5.8-23]. The XeF_2 and F_2 dissociatively chemisorb on the Si surface, however the reaction kinetics for fluorine interactions with Si are different [5.9,10,13,15,21] for these two molecules as well as for atomic F. Surface analysis studies by X-ray photoelectron spectroscopy (XPS) of F and F_2 adsorption on Si(111) [5.14] suggest that F_2 acts like low-pressure XeF_2 exposure, while F atoms are similar to high-pressure XeF_2. The kinetic differences between these F-containing molecules has been due to the initial adsorption step as opposed to the F-Si reaction or desorption steps [5.12-14,21].

The surface reactions of F with Si produce [5.34] a room temperature stable fluorosilyl (SiF_n, n=1,2,3,4) reaction layer on the Si under vacuum conditions. The initial chemical adsorption (chemisorption) of F (by XeF_2) on Si(100)-2x1 has been studied by XPS [5.17] and low energy electron diffraction (LEED) [5.16]. The XPS spectra taken of the Si surface covered by approximately 2 monolayers (ML) of fluorine showed the major species to be SiF_1 (1.16ML) along with 0.39ML of SiF_2 and a small amount of SiF_3. The p(2x1) LEED pattern corresponding to the initial Si(100) surface became more diffuse upon F adsorption, which suggests that the SiF reaction layer was amorphous [5.16]. Under steady-state etching conditions of Si(111), this amorphous fluorosilyl layer is estimated to be 1 to 2nm thick [5.12,18,19] with SiF_3 as the dominant adspecies. This observation indicates that the formation of SiF_4 as the primary etch product [5.8,11,12,15] from SiF_3 may be the rate-limiting step [5.12,18,19]. However, the exposure of Si(100) to F_2 and atomic F beams showed [5.19,20] that only SiF_2 was adsorbed at low coverages, while at higher coverages a mixture of SiF_2 and SiF_4 was found. Such discrepancies illustrate the Si structure and fluorine reagent sensitivity to the initial reaction mechanism.

The effects of energetic particle bombardment present from reactive plasma etching of Si has been simulated by inert argon ion (Ar^+) in the presence of a fluorine-containing flux [5.34]. The etching characteristics have been described in terms of etch yield, specific etch products and surface fluorination as a function of the fluorine gas flux, but with respect to energetic reactive ion bombardment of the Si surface. A control of the reactive atom kinetic energy impinging on the Si surface has produced detailed characterization of the residual surface damage in the form of kinetic energy dependences on the degree of crystalline disorder [5.35-37] and reactive species surface incorporation [5.38]. In addition , the etch yield dependence on ion energy and reactive species has been reported [5.39]. This control of reactive F^+ particle energy is essential to the understanding of plasma-based reactive ion etching of Si because the energy range of technological interest (500 down to 0eV) has not been extensively studied [5.40]

The objective of this chapter was to study the residual surface damage of Si(100) induced by F^+ ion bombardment in the energy range of 20-100eV and for a range of doses indicative of initial development of surface reactions, i.e. less than one equivalent monolayer of F atom coverage ($3x10^{14}/cm^2$) to a few hundred monolayers ($1x10^{17}/cm^2$) delivered to the surface. The development of a surface Si-containing reaction layer and degree of fluorine surface incorporation was characterized. The effects of ion fluence on the surface band-bending was also investigated, and the thermal stability of the surface fluorine was evaluated by *in-situ* vacuum heating to temperatures up to 800°C

Surface modifications from conventional plasma etching of Si with reactive F^+ ions was simulated with a mass-separated low energy $^{19}F^+$ ion beam system The use of post-ion-beam-etch surface analysis has become highly relevant to the understanding of

plasma-surface interactions [5.41], and for this work the resulting surface exposed to the reactive ion beam was analyzed *in-situ* by X-ray photoelectron spectroscopy (XPS).

The (F/Si) surface composition ratio was monitored as a function of ion fluence in the range of $3\times10^{14}/cm^2$ to $1\times10^{17}/cm^2$ for a constant ion kinetic energy of 100eV. The Si2p core-level spectra indicated the development of a thin (<3nm) fluorosilyl (SiF_n, n=1,2,3) surface reaction layer with increasing ion dose. The results showed that the fluorine incorporation reached a saturation level when the ion dose was above $1\times10^{16}/cm^2$. This suggested that F^+ ion bombardment beyond an ion dose of $1\times10^{16}/cm^2$ at 100eV produces steady-state etching under the present configuration. The effects of ion kinetic energy were studied over the range of 20 to 100eV for a fixed dose of $3\times10^{16}/cm^2$. The thickness of the thin fluorosilyl layer formed at the different bombardment energies was approximately the same. The relative amount of surface fluorine was found to be increased by 25% from 100eV to 20eV. Therefore, the higher ion kinetic energy produced a lower sticking probability to the Si surface by increased sputtering. The effect of vacuum heating to ultimately 800°C for 30min resulted in a greater amount of fluorine thermal desorption at the lower ion bombardment energy (up to 54% for the 20eV case). This study showed that the amount of surface fluorine and the thermal stability of the fluorine was dependent on the ion kinetic energy.

5.2 Experimental procedure

The Si(100) samples used in studying the effects of ion fluence were boron

implanted at 16keV with a dose of $1.6x10^{15}$ atoms/cm^2 followed by rapid thermal annealling at 1050°C for 30s to electrically activate the dopant. For investigating the effects of ion bombardment energy, n-type Si(100) samples were used. All samples were wet etched in a dilute aqueous hydrofluoric acid (HF) solution for 30-45s and blown dry with nitrogen gas to remove the passivating oxide. The samples were then immediately loaded into the LEIB system for reactive F^+ ion bombardment.

$^{19}F^+$ ions were extracted from a CF_4 plasma confined within a hot dc filament Colutron ion source. The LEIB system is described in Chapter 3. In this study, the ion beam delivered mass-separated F^+ ions at normal incident to the Si(100) surface for a range of ion kinetic energies between 20-100eV and a range of ion doses from $3x10^{14}$ to $1x10^{17}/cm^2$. All ion bombardment experiments were conducted at room temperature Once samples were exposed to the ions, the specimens were transferred under vacuum ($P<1x10^{-6}$Torr) to an XPS system for surface analysis.

The XPS spectrometer was an SSX-100 small X-ray spot system (see Chapter 3) Spectra were collected at pass energies of 100eV for quantification and 20eV for high resolution. The X-ray spot size at the sample surface was approximately 300μm in diameter. All spectra were acquired at a constant photoemission polar angle of 55° with respect to the sample normal. Surface atomic concentrations were calculated (see Chapter 3) and binding energy positions were determined using an iterative chi-squared minimization peak-fitting program with a Gaussian-Lorentzian profile All peak positions were referenced to the $Au4f_{7/2}$ core-level peak position at 83.93eV from an Ar^+ sputter-cleaned gold foil always present under UHV conditions

Vacuum heating of the ion bombarded specimens was carried out in a separate

UHV ($1x10^{-8}$Torr) preparation chamber coupled to the XPS instrument (see Chapter 3). Sample holders were heated with a resistive heating coil positioned at the base of the holder. A K-type thermocouple was attached to the sample holder rod. Samples were heated gradually to the desired temperature with special attention to minimize overshooting the target temperature. Once the required temperature was achieved, the sample was held at that value for 30min. The temperature fluctuations at a constant temperature were less than 5°C. The heating temperature studied was 800°C. After vacuum heating was completed, the sample was allowed to cool under UHV to just above room temperature (30°C) and then transferred under vacuum ($<1x10^{-6}$Torr) back into the XPS system for surface analysis.

5.3 Results and discussion

5.3.1 Effect of ion dose at 100eV

The effects of F^+ ion dose at a constant kinetic energy of 100eV on the surface residual damage of p-type Si(100) were identified from the surface analysis. Figure 5.1 shows the surface atom concentration ratio of F/Si as a function of ion fluence. The F/Si composition ratio values increased monotonically to a dose of $1x10^{16}/cm^2$. Above this dose of $1x10^{16}/cm^2$, a saturation level of surface fluorine was observed. This dose dependence is similar to the amorphization-ion fluence behaviour seen for Cl^+ bombardment of Si(100) at 300eV [5.35]. This latter halide ion induces greater Si surface

Figure 5.1 **XPS surface compostion ratio of F/Si (at a photoemission polar angle of 55° v.ıth respect to the sample surface normal) as a function of F^+ ion dose at a constant kinetic energy of 100eV**

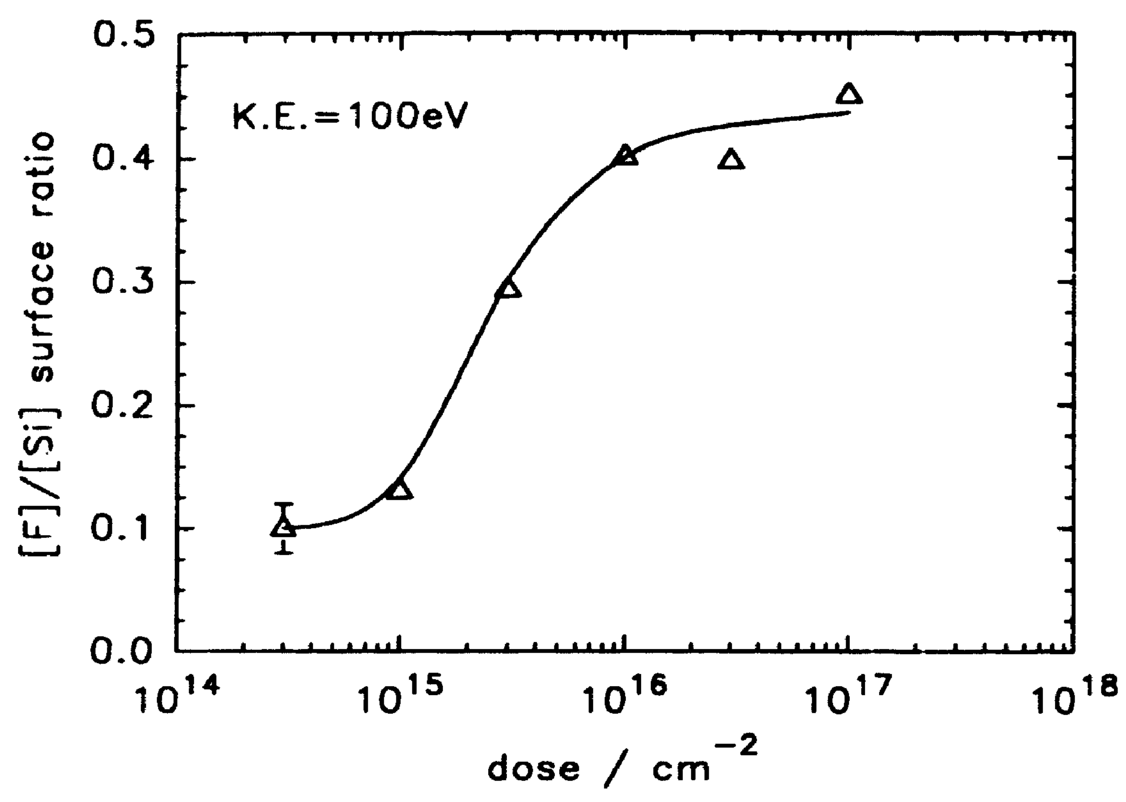
K.E.=100eV
[F]/[Si] surface ratio
dose / cm^{-2}
0.0
0.1
0.2
0.3
0.4
0.5
10^{14}
10^{15}
10^{16}
10^{17}
10^{18}

disorder with increasing ion dose in the range of $1x10^{13}$ to $1x10^{16}/cm^2$ Such disorder was ascribed to physical damage effects by the energetic ion bombardment because of the similar behaviour caused by Ar^+ bombardment [5.35] Also, the depth of residual damage induced by Cl^+ and Ar^+ bombardment of Si was found to be similar at 110eV for a dose of $3x10^{16}/cm^2$ [5.37]. If surface amorphization was taking place with increased ion dose, and it has been shown that F tends to getter in the region of residual damage [5.42,43], then it is proposed that the Si(100) surface was becoming more disordered as the level of F^+ ion surface incorporation increased with dose.

This surface disorder may be due to chemical as well as physical effects because the F-Si chemical affinity produces spontaneous etching of Si [5.44] At 100eV, the F^+ ions possessed sufficient energy to disrupt the Si surface and cause physical sputtering as well as shallow ion implantation. It is known [5.34] that a stable fluorosilyl (SiF_n, n=1,2,3) surface species layer is associated with Si etching SiF_4 is believed to be a principal volatile etch product from room temperature etching studies [5.34]

Figure 5.2 shows the effect of F^+ ion fluence at 100eV on Si surface compound production. The Si2p core-level spectra corresponding to surfaces receiving doses of $3x10^{14}$, $3x10^{16}$ and $1x10^{17}/cm^2$ were overlayed. The major peak near 99.5eV binding energy was due to the semiconducting Si in the 0 oxidation state For the dose of $3x10^{14}/cm^2$, the core-level spectrum was similar to an unbombarded Si(100) surface Figure 5.1 shows that for this dose the surface F/Si ratio was at 0.10 It is likely that this very small ion dose produced some fluorosilyl surface species on the silicon, but the XPS instrument was insensitive to the detection of this small amount

At doses of $3x10^{16}$ and $1x10^{17}/cm^2$, a broad, low intensity spectral component

Figure 5.2 XPS high resolution Si2p spectra for p-type Si(100) after 100eV F^+ ion bombardment at doses of $3x10^{14}$, $3x10^{16}$ and $1x10^{17}$ions/cm^2; (a) spectra scaled and overlayed to the same peak height, and (b) spectra overlayed with each spectrum normalized to total area under each peak profile.

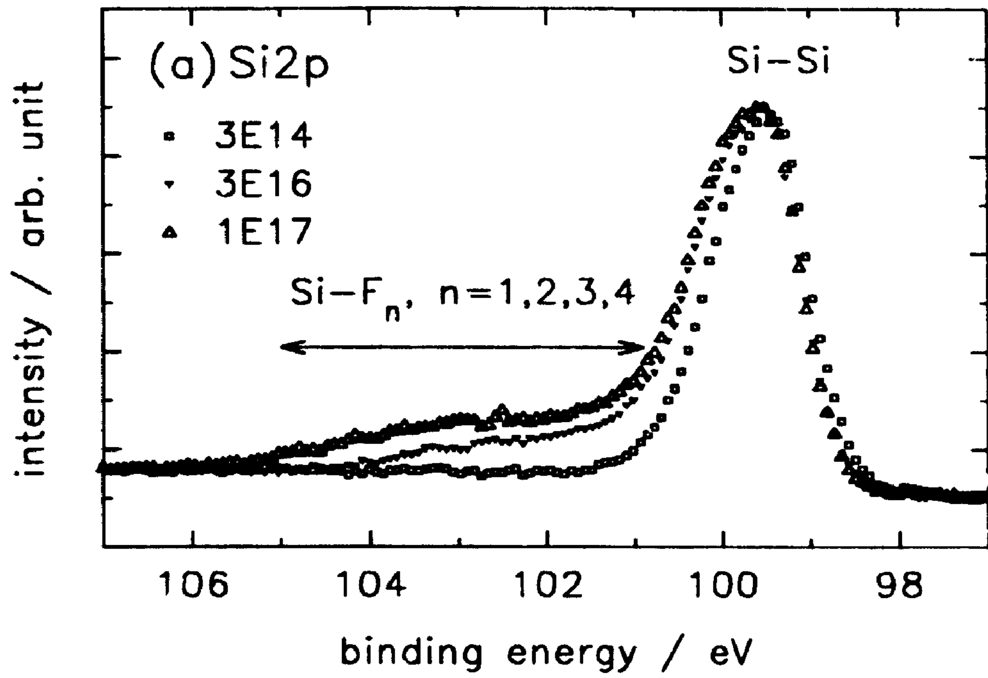

(a) Si2p
Si–Si
3E14
3E16
1E17
Si–F$_n$, n=1,2,3,4
intensity / arb. unit
106
104
102
100
98
binding energy / eV

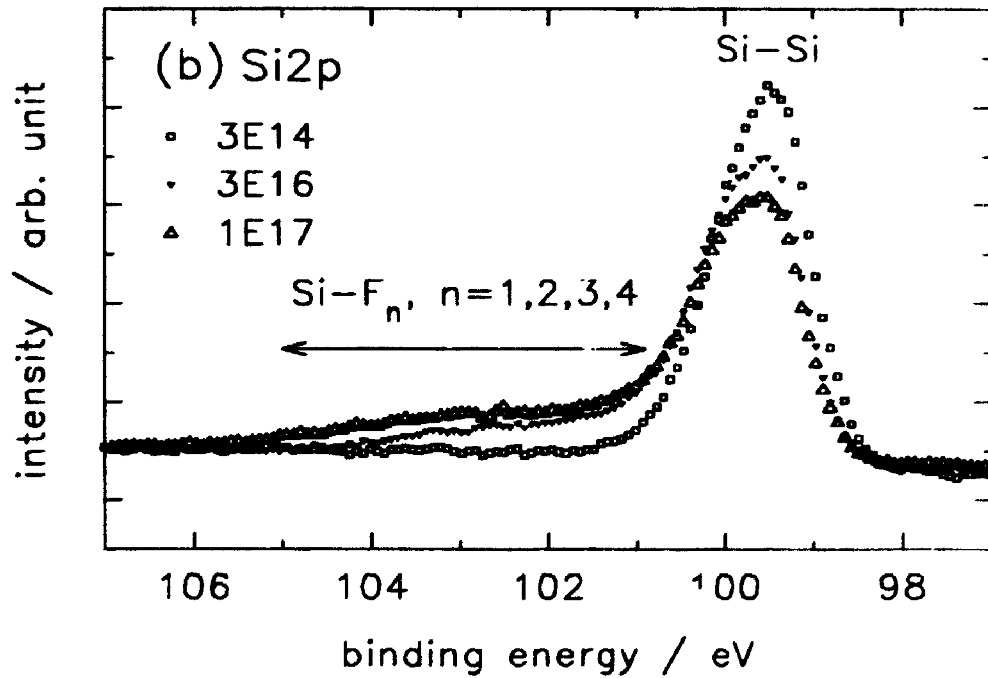

(b) Si2p
Si–Si
3E14
3E16
1E17
Si–F$_n$, n=1,2,3,4
intensity / arb. unit
106
104
102
100
98
binding energy / eV

extending to higher binding energy than the Si-Si peak indicated Si species with oxidation states ranging from +1 to +4. This broad component was assigned to the development of a fluorosilyl species reaction layer [5.34]. The binding energy positions representing these SiF species were tabulated in Chapter 4 (Table 4.2) with mono-, di, and tri-fluorosilyl species appearing in order of increasing binding energy from the semiconducting Si peak near 99.5eV. The change in binding energy for each Si-F species is approximately 1.1eV [5.34] for each increase in oxidation state corresponding to greater fluorination of Si. However, due to the overlapping of peak-fitted components from the $2p_{3/2}$ and $2p_{1/2}$ doublets for each SiF_n (n=1,2,3,4) component, these peaks were omitted from Figure 5.2 to avoid confusion. The increased intensity from this broad component in Figure 5.2 corresponded to the development of this Si-F compound layer as a consequence of greater ion exposures.

For the Si surface receiving $1x10^{17}/cm^2$ dose, Figure 5.2 indicates the detection of a low intensity component above the background level near 104eV binding energy which can be attributed to SiF_4 species (e.g +4.4eV from the Si-Si peak at 99.5eV). This volatile fluorosilyl component is believed to be trapped within the reaction layer [5.34]. From studies utilizing molecular beams of F_2 exposed to Si(100) [5.21], F saturation surface coverages were achieved with F exposures greater than 200 monolayers. Since one monolayer of F surface coverage on the Si(100)-2x1 surface is approximately equal to $6.86x10^{14}$atoms/cm^2 [5.17], a dose of $1x10^{17}/cm^2$ approximately corresponded to 146 monolayers delivered to the surface. Thus, it was reasonable to presume that etching was developing at such an ion fluence. As well, the influence of energetic ion bombardment at this dose more than likely induced chemically-enhanced physical sputtering and/or

chemical sputtering [5.8]. The existence of SiF_4 trapped species (which is a principle etch product [5.34]) supports this claim of Si etching with 100eV F^+ ions

Under conditions of steady-state etching for Si(111) exposed to XeF_2 and 500eV Ar^+ ion bombardment, it has been shown [5.18] that the SiF_3 species were the major components of the fluorosilyl layer. It has been proposed [5.45] that as the exposure increases, the SiF_3 concentration at the surface increases and subsequently buries a relatively constant concentration of SiF_2 and SiF_1 species which are found nearer to the Si substrate. In contrast, Figure 5.2 shows that the formation of this layer was greatest for SiF_1 followed by SiF_2 then SiF_3 as the ion fluence increased. This difference may be due to the presence of a large neutral flux in the previous studies [5.18,45] enhancing the Si-F reaction. Also, the 500eV Ar^+ bombardment [5.18] will induce a larger degree of physical damage than the 100eV F^+ ions because of its heavier projectile mass and greater kinetic energy. Also, this would give rise to greater implantation of fluorine atoms leading to Si-F species and perhaps greater SiF_3 formation.

Figure 5.2 also shows the broadening of the elemental Si peak at 99.5eV binding energy with increasing ion dose. This broadening effect was caused by greater disordering of the Si crystalline surface [5.46]. At the lowest dose of $3 \times 10^{14}/cm^2$, there was minimal widening in the full-width-half-maximum (FWHM) of the Si-Si peak and no surface Si-F reaction products. As the dose increased, the Si-Si peak FWHM increased and there was an accompanying increase in fluorosilyl surface products. Therefore, the accommodation of F into the Si(100) surface with increasing ion fluence at 100eV was via F penetration and concomitant growth of a disordered lattice along with the fluorosilyl reaction layer.

The F1s core-level spectra for all the samples analyzed by XPS showed a single symmetric photoemission peak centred at approximately 686.4eV binding energy with a FWHM of 1.9eV. This peak was assigned to a F-Si environment. These values for peak position and FWHM were in agreement with XPS studies on the surfaces of Si(100) after RIE in CF_4 and SF_6 glow discharges [5.41] in which it was reported that the F1s core-level peak from the fluorinated Si surface was at approximately 686.6eV binding energy with a FWHM of 2.0eV. There appeared to be no detectable chemical shifts for the fluorine atom either singly-, doubly-, or triply-bonded to the silicon atom. This group VII element is so electronegative that it does not tend to share electrons in various chemical combinations and usually is found in the -1 oxidation state [5.46]. The chemical shifts for F bonded to other elements such as carbon are distinguishable [5.46], but in this F-Si system, the chemical shifts from the F1s core-level were small.

Therefore, the extent of residual surface damage as a result of 100eV F^+ ion bombardment was seen as an increase in F incorporation in the form of both implanted ions and fluorosilyl reaction species with greater ion dose. The results from Figure 5.2 show that the effects of surface damage and fluorosilyl development were interrelated. A recent study [5.41] has established that the surface damage due to energetic ion bombardment precedes the fluorosilyl species formation (speciation). Model calculations have been reported [5.28] in which the reaction mechanism for F etching of Si involves Si-Si bond breaking and F-atom attachment. The reaction for F-atoms to attach to Si dangling bonds is calculated to be exothermic by approximately 6eV [5.28,47], and the generation of ruptured Si bonds from the ion bombardment process is predicted [5.28] to enhance the production of SiF_4 etch species via an attack of SiF_3 species bonded to Si.

Such predictions may suggest that the surface crystalline damage enhances fluorosilyl speciation, and these results support this idea.

The effect of the increased ion fluence on the p-type Si(100) surface Fermi level position was studied by XPS surface analysis. The surface Fermi level positions were determined from the $Si2p_{3/2}$ core-level peak from the semiconductor Si. The references for the Fermi level measurements were obtained from a large set of binding energy values for p-type Si(100) samples which showed [5.48] that the $Si2p_{3/2}$ peak should be at 98.7eV binding energy when the Si possessed a Fermi level at the valence band maximum (VBM). The accuracy of the surface Fermi level measurement was estimated to be ±0.05eV [5.49,50]. Hence, the surface Fermi level position was determined by subtracting 98.7eV from the $Si2p_{3/2}$ binding energy positions for the samples receiving various F^+ ion fluences and the VBM level was set to 0.0eV.

Figure 5.3 shows the dependence of surface Fermi level position with ion dose at 100eV. At the low dose of $3x10^{14}/cm^2$, the Si surface was no longer p-type because the Fermi level position was just above the midgap. As the ion dose was increased at 100eV, the Fermi level position gradually shifted toward the conduction band minimum (CBM). This indicates that as a consequence of low energy F^+ ion irradiation, the p-type Si surface was type-inverted.

Fluorinated amorphous Si has received considerable interest because of its light illumination properties [5.51,52]. F^+ implantation into amorphous Si films was found to have desirable semiconducting properties such as a reduced density of bandgap states [5.53]. Because of the energetic ion bombardment process, the surface amorphization of Si by F^+ implantation at high dose can be controlled [5.54]. It has been shown [5.54]

Figure 5.3 Effect of ion dose on surface Fermi level position as a result of F^+ ion bombardment at 100eV.

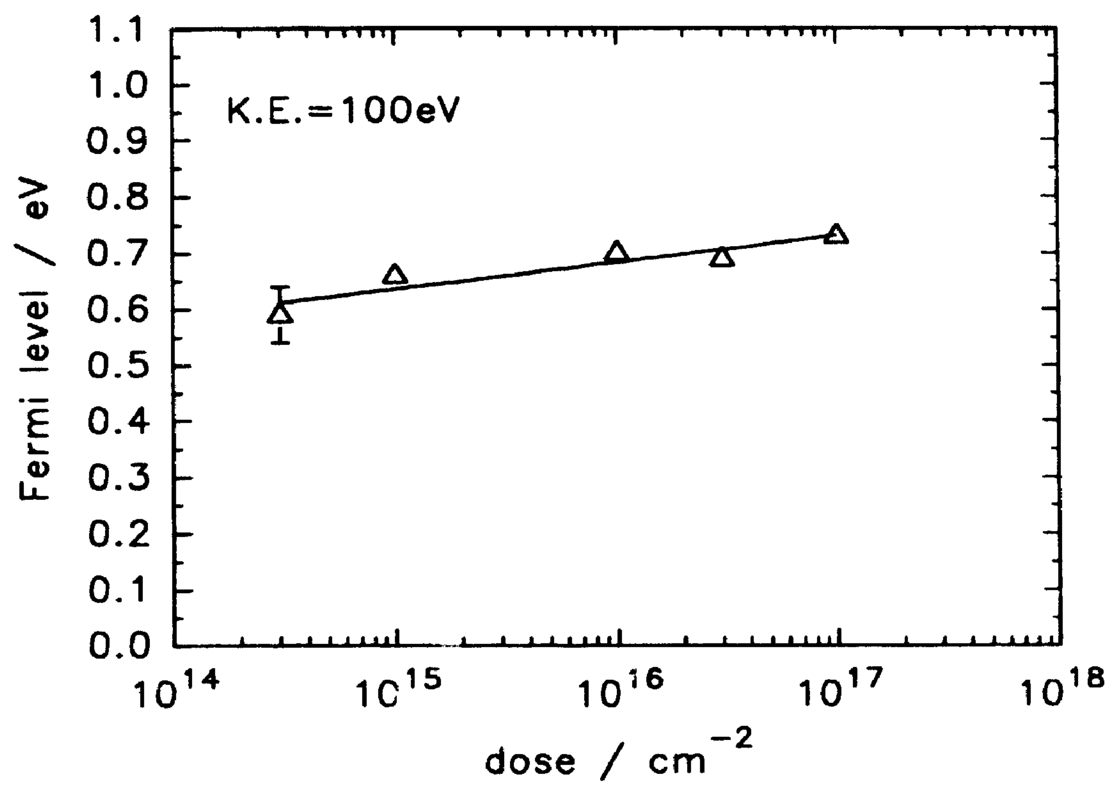
K.E.=100eV
Fermi level / eV
dose / cm^{-2}
1.1
1.0
0.9
0.8
0.7
0.6
0.5
0.4
0.3
0.2
0.1
0.0
10^{14}
10^{15}
10^{16}
10^{17}
10^{18}

that the photovoltage is negative for room temperature F^+ implanted at 90keV and dose of $3x10^{16}/cm^2$ into p-type Si. This shows that electrons accumulate on the surface and it was concluded that this amorphous layer was n-type. The results for low energy F^+ bombardment at 100eV support this conclusion. The accommodation of F into the p-type Si surface may have resulted in an increase of conduction electrons provided by the F atoms causing type-inversion of the surface.

5.3.2 Effect of ion kinetic energy at $3x10^{16}/cm^2$

Figure 5.4 represents the F incorporation dependence on incident ion kinetic energy for the range of 20-100eV and a constant dose of $3x10^{16}/cm^2$. The surface F/Si ratio was approximately 0.27 after 100eV F^+ bombardment. This ratio increased asymptotically towards a value of 0.35 as the F^+ bombardment energy was reduced. This observed energy dependence on the F surface concentration is similar to a generalized plot of incident particle sticking probability versus ion kinetic energy [5.55] at kinetic energies below 1000eV.

The spontaneous reaction between F and Si has been well established experimentally [5.34,44], and the sticking probability for near thermal atomic fluorine on the Si(100) surface has been calculated to be near unity [5.56]. Hence a decrease of the bombardment energy towards the thermal energy limit is expected to bring the surface incorporation probability, at least for the first monolayer arrival, to unity.

As the kinetic energy increased above 40 to 100eV, the amount of surface F was being reduced and so the surface incorporation probability was less. This reduction could have been due to the dissipation of excess energy which prevents the F^+ ions from being

Figure 5.4 XPS surface composition ratio of F/Si (at a polar photoemission angle of 55° with respect to the sample surface normal) as a function of F^+ ion kinetic energy with a constant dose of $3x10^{16}$ions/cm^2 for room temperature bombardment conditions.

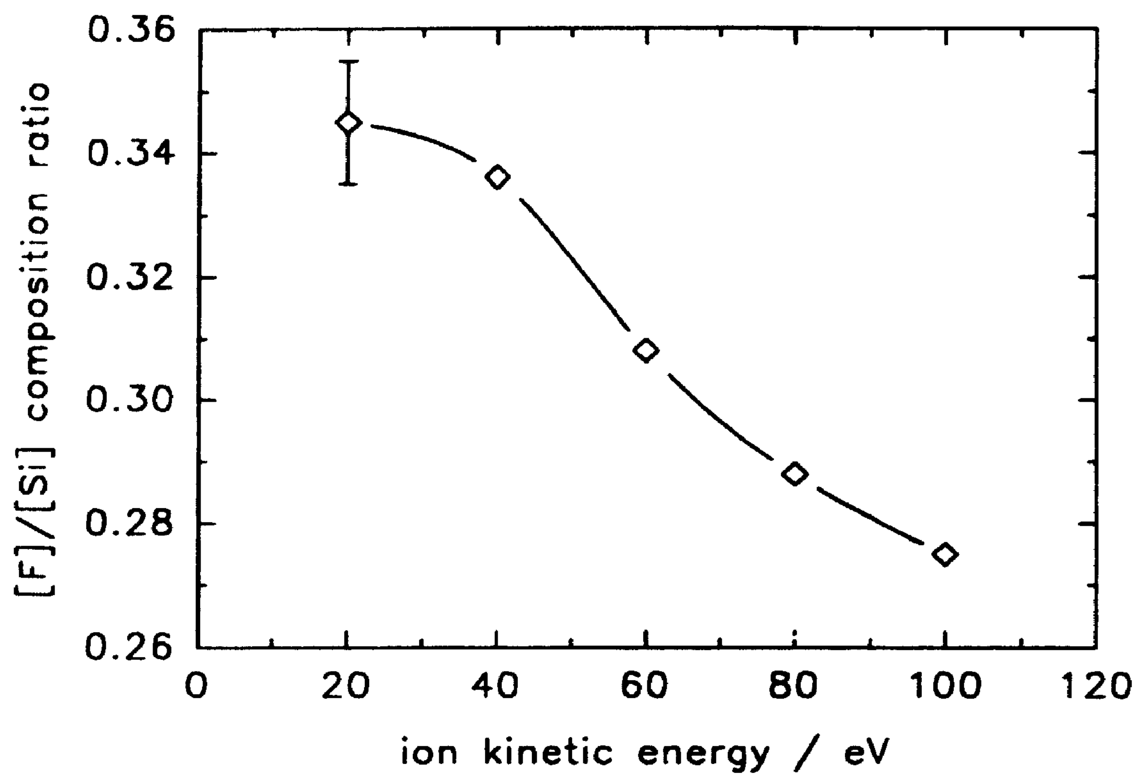

0.36
0.34
0.32
0.30
0.28
0.26
[F]/[Si] composition ratio
0
20
40
60
80
100
120
ion kinetic energy / eV

trapped into a surface product potential well [5.55], and thereby enhances the re-emission of F from the surface. Another process in which the surface concentration of fluorine may have been minimized was by physical sputtering. The physical sputtering threshold energy has been calculated to be as low as 20eV [5.57,58], and this sputtering process may have contributed to the ejection of surface F atoms (fluorine self-sputtering) as well as Si atoms via collisional cascades and/or local energy spikes within the solid surface

In addition, weakly adsorbed Si-F reaction products can be desorbed from the surface as a result of momentum transfer from incoming F^+ ions and recoiling atoms (chemically-enhanced physical sputtering [5.59]) or simply from the fact that these reaction species have low enough surface binding energies to desorb into the gas phase (chemical sputtering [5.8]). The chemically-enhanced physical sputtering and chemical sputtering effects are believed to occur generally in the ion kinetic range from 100's of electronvolt energies down to 10eV [5.59]. The experimentally measured chemical sputtering yield for the F^+/Si system has been reported [5.39] in the ion energy range of 100 to 1000eV. This yield decreases linearly with a positive slope from 500 down to 100eV, and is linearly extrapolated down to 10eV [5.39]. If this assumption were valid, then the extent of chemical sputtering would increase from 10 to 100eV Hence, the reduction in surface F incorporation from 20 to 100eV ion energy was perhaps caused by an increase in chemical sputtering as well as chemically-enhanced physical sputtering effects, in addition to the effects of backscattering and physical sputtering

Figure 5.4 shows that the amount of surface F incorporation was increased by approximately 25% from 100eV down to 20eV (F/Si=0.28 at 100eV, and F/Si=0.35 at 20eV). The barrier for F penetration from the Si top layer to the second layer is

calculated to be relatively low at 1eV [5.24], and this is why even thermal F atoms can break the back-bone Si-Si bonds and etch silicon. However, fluorine bombardment at a high energy results in a larger penetration depth, and the 20eV F^+ ions were not believed to have physically penetrated to depths greater than the 100eV case. Since XPS is a surface sensitive technique, it will give a lower fluorine surface concentration if the same amount of fluorine is distributed more deeply. Hence the decrease in surface fluorine from 20 to 100eV may also be due to a lack of XPS detection sensitivity for the more deeply distributed fluorine at the higher bombardment energies.

In Figure 5.5, the effect of ion kinetic energy on surface Si reaction was represented by overlays of the Si2p spectra for samples bombarded by 20 and 100eV F^+. The development of a relatively thin SiF_n, n=1,2,3,4 layer was seen as a low intensity broad component towards higher binding energy from the Si-Si peak. Figure 5.5a shows the overlayed spectra scaled to the maximum peak height. The spectra for the 100eV ion bombardment case was slightly greater in intensity than for the 20eV case at the binding energies between 101 and 102eV. However, Figure 5.5b shows that when the spectral overlays were normalized to total peak area, the fluorosilyl species component intensities were very similar. Therefore, the variation in incident ion energy (in the range of 20 to 100eV) did not appear to promote selective reactions of one SiF stable surface product over any of the others at room temperature.

At the dose of $3x10^{16}/cm^2$, approximately 44 equivalent monolayers of F atoms had impinged onto the surface. Such a dose was likely sufficient to initiate the fluorosilyl species formation, and produce steady-state etching of the Si. Therefore, this work indicates that the initial fluorosilyl layer thickness was not dependent to a large extent on

Figure 5.5 High resolution XPS spectra of the Si2p core-level for Si(100) surfaces receiving 20 and 100eV F^+ at $3x10^{16}$ions/cm^2 for room temperature conditions; and the control spectrum represented an unbombarded surface region of the Si(100) sample, (a) spectra scaled and overlayed to the same peak height, and (b) spectra overlayed with each spectrum normalized to total area under each peak profile.

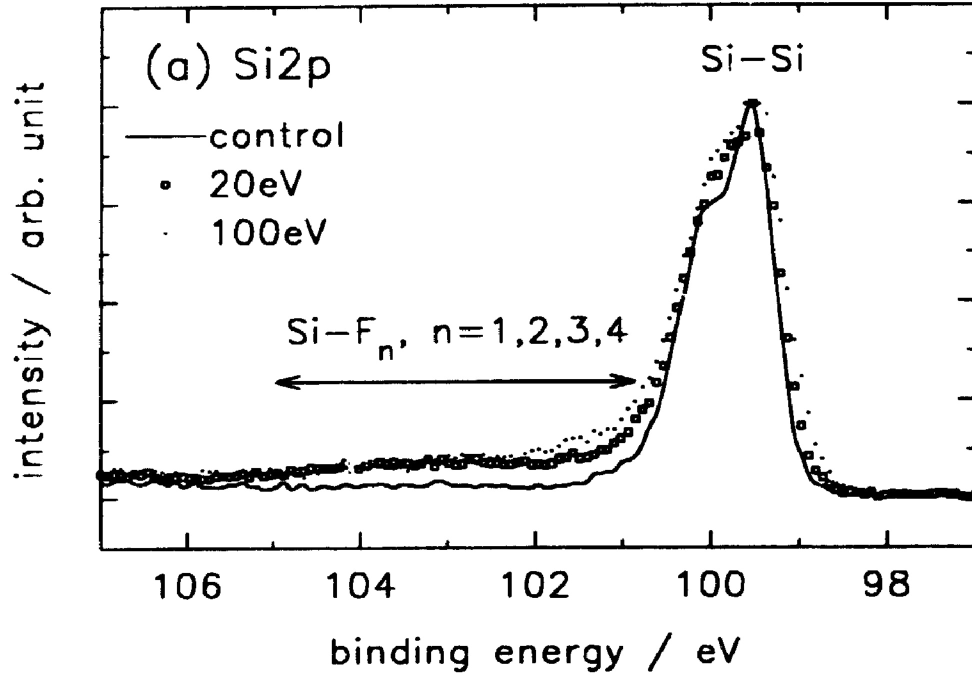
(a) Si2p
Si–Si
control
20eV
100eV
Si–F_n, n=1,2,3,4
intensity / arb. unit
106
104
102
100
98
binding energy / eV

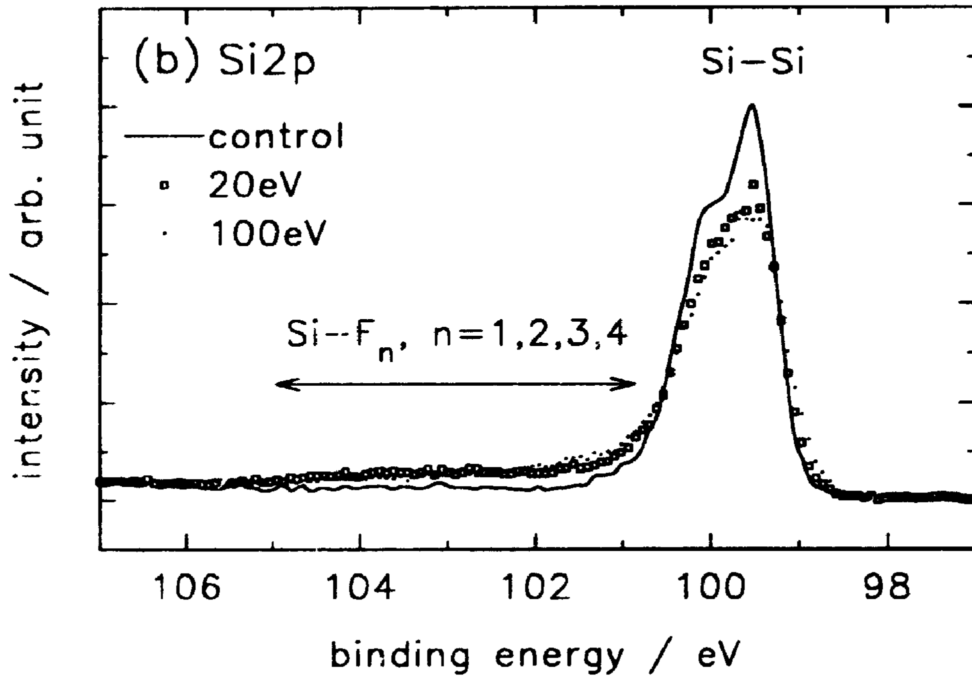
(b) Si2p
Si–Si
control
20eV
100eV
Si–F_n, n=1,2,3,4
intensity / arb. unit
106
104
102
100
98
binding energy / eV

the F^+ kinetic energy in the range between 20 and 100eV, and at a constant dose of $3x10^{16}/cm^2$.

A close examination of the Si-Si peak FWHM from Figure 5.5a indicated a detectable broadening as a result of bombardment at different ion energies. This broadening was apparent when compared to the overlayed control spectrum for an unbombarded region of the Si(100) surface. A recent first-principles-derived dynamical calculation of fluorine etching of Si(100) has been reported [5.60] in which it was concluded that disorder of the fluorinated surface was necessary for the buildup of the fluorosilyl layer. This work shows that both surface crystalline disorder and fluorosilyl species formation occur as a consequence of F^+ ion bombardment between 20 and 100eV.

A very recent investigation by Oehrlein [5.41] on the effects of ion kinetic energy on the steady-state reactive ion etching of Si in glow discharges of CF_4 and SF_6 concluded that the SiF_x layer thickness was less at lower ion bombardment energy. The ion bombardment energy was not directly measured in that reported work [5.41] but inferred from the pressures used to generate the reactive plasma (250 to 25mTorr). The number of ion-neutral collisions within the plasma environment increases with greater pressure, and the energy of bombarding ions impinging on the Si surface is lowered [5.61,62]. In addition, a large spread of ion energies exists ranging from a maximum estimated value related to the plasma self-bias potential down to almost no energy due to the collisional processes in the plasma sheath region [5.33]. Since the intensity due to the fluorosilyl layer in that reported work [5.41] was very similar to that seen in this work for F^+ ions between 20 and 100eV at a dose of $3x10^{16}/cm^2$, it was believed that this ion energy range represented the same low energy ions seen by Oehrlein using CF_4 at 250mTorr. However

it should be noted that the dose used in this work was much less than for the above study.

Oehrlein also reported [5.41] that the SiF layer thickness was much greater at the higher ion bombardment energies with SiF_3 having the highest intensity. In the present work, the stable surface fluorosilyl species formed between 20 and 100eV F^+ and dose of $3x10^{16}/cm^2$ had a reduced intensity compared to the work by Oehrlein [5.41]. This difference is believed to be attributed to the different depth of surface analysis (polar angle of 55° in this case versus 75° for Oehrlein's work) and to the higher doses used in Oehrlein's reported investigation.

The extent of F penetration depth can be studied from an analysis of the intensity ratio between the F1s and F2s core-level signals. The photoemission of electrons from the F1s core-level has an inelastic mean free path (IMFP) of 2.7nm through the Si surface region which is less than that of the F2s photoelectrons which has a IMFP value of 3.7nm (see chapter 3). This essentially means that the effective sampling depth is shallower for F1s level electrons than for the F2s case. Hence, from monitoring the (F1s/F2s) signal ratio it is possible to qualitatively evaluate the extent of the F distribution in depth from the surface [5.63]

Figure 5.6 represents the dependence of the surface (F1s/F2s) intensity ratio on F^+ kinetic energy. The decrease in this ratio from 20 to 80eV clearly demonstrates that the incident F^+ ions were being implanted below the surface at greater depths as a result of increased ion energy. This occurred because the higher energy ion bombardment resulted in increased penetration below the Si surface. This hypothesis was consistent with the lowest energy F^+ impingement resulting in the shallowest depth distribution of fluorine atoms into the silicon.

Figure 5.6 Variation of (F1s/F2s) peak area ratio with F^+ ion kinetic energy at a constant dose $3x10^{16}$ions/cm^2 for room temperature conditions.

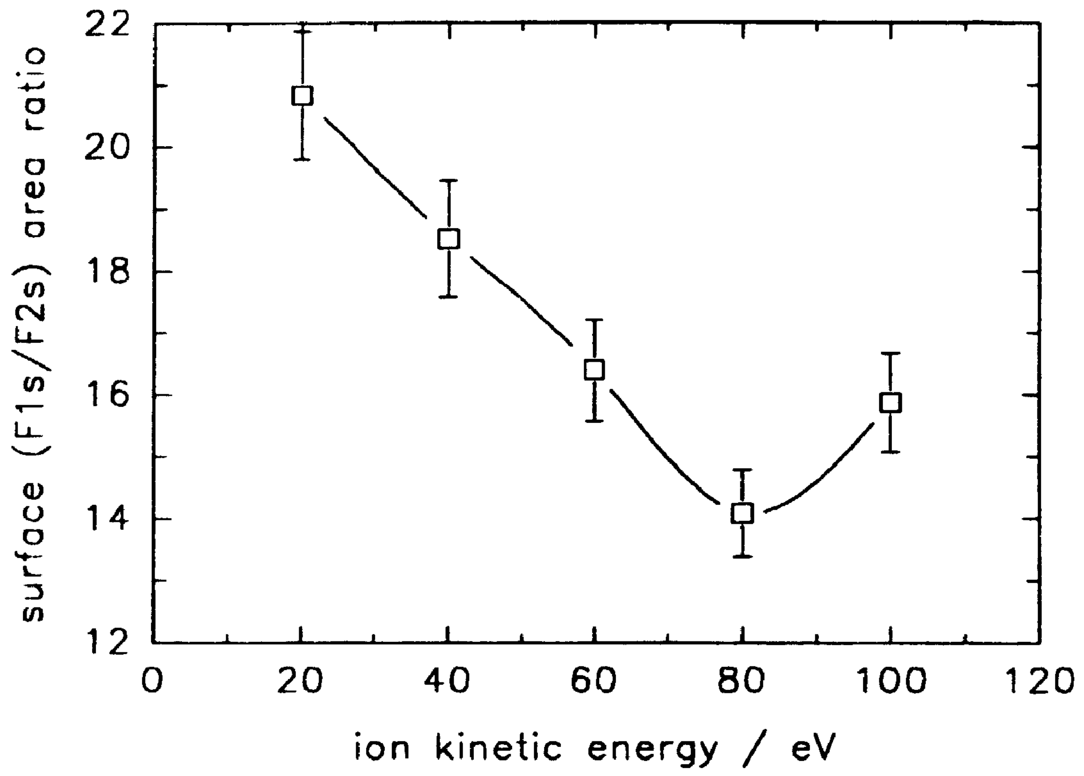
surface (F1s/F2s) area ratio
22
20
18
16
14
12
0
20
40
60
80
100
120
ion kinetic energy / eV

However, the F^+ bombardment at 100eV produced a F1s/F2s ratio that was higher than the 80eV case by almost 13%. This meant that there was a shallower depth distribution of F atoms at the surface for the 100eV bombarded Si compared to 80eV ions even though there was a smaller surface concentration of F at 100eV (see Figure 5.4). This anomalous increase in the (F1s/F2s) ratio between 80 and 100eV was believed to be caused by a higher sputtering (both physical and physico-chemical) probability of F (i.e. greater F self-sputtering) and its fluorosilyl species from the surface over the probability for ion implantation or penetration compared to the lower fluorine ion energies. Such a sputtering process may have given the lower F surface concentration at the higher energies (Figure 5.4) as well as a shallower depth distribution (Figure 5.6).

The valence band photoemission spectra are shown in Figure 5.7 for the Si(100) surface receiving 20 and 100eV ion bombardment at a constant dose of $3x10^{16}/cm^2$. The spectrum corresponding to the control surface represented a region of the Si(100) surface not exposed to the energetic F^+ ion bombardment. This spectrum shows three distinguishable wide peaks near 3, 8 and 10eV binding energies. Such bands represent the molecular orbitals of the Si3s and Si3p valence electrons [5.64] and are due to crystalline Si(100) terminated at the surface by hydrogen bonds [5.65]. After 20eV F^+, these bands were broadened to an appreciable extent with the first two bands at 3 and 8eV also reduced in intensity. Following 100eV ion bombardment, the second band near 8eV binding energy was altogether indistinguishable from the broad diffuse band at 10eV. Since the degree of Si fluorination was seen to be approximately the same at all ion energies between 20 and 100eV (see Figure 5.5), the changes in the valence band spectra at the different energies attributed to surface fluorosilyl speciation were considered to be

Figure 5 7 Valence band photoemission spectra corresponding to Figure 5.5

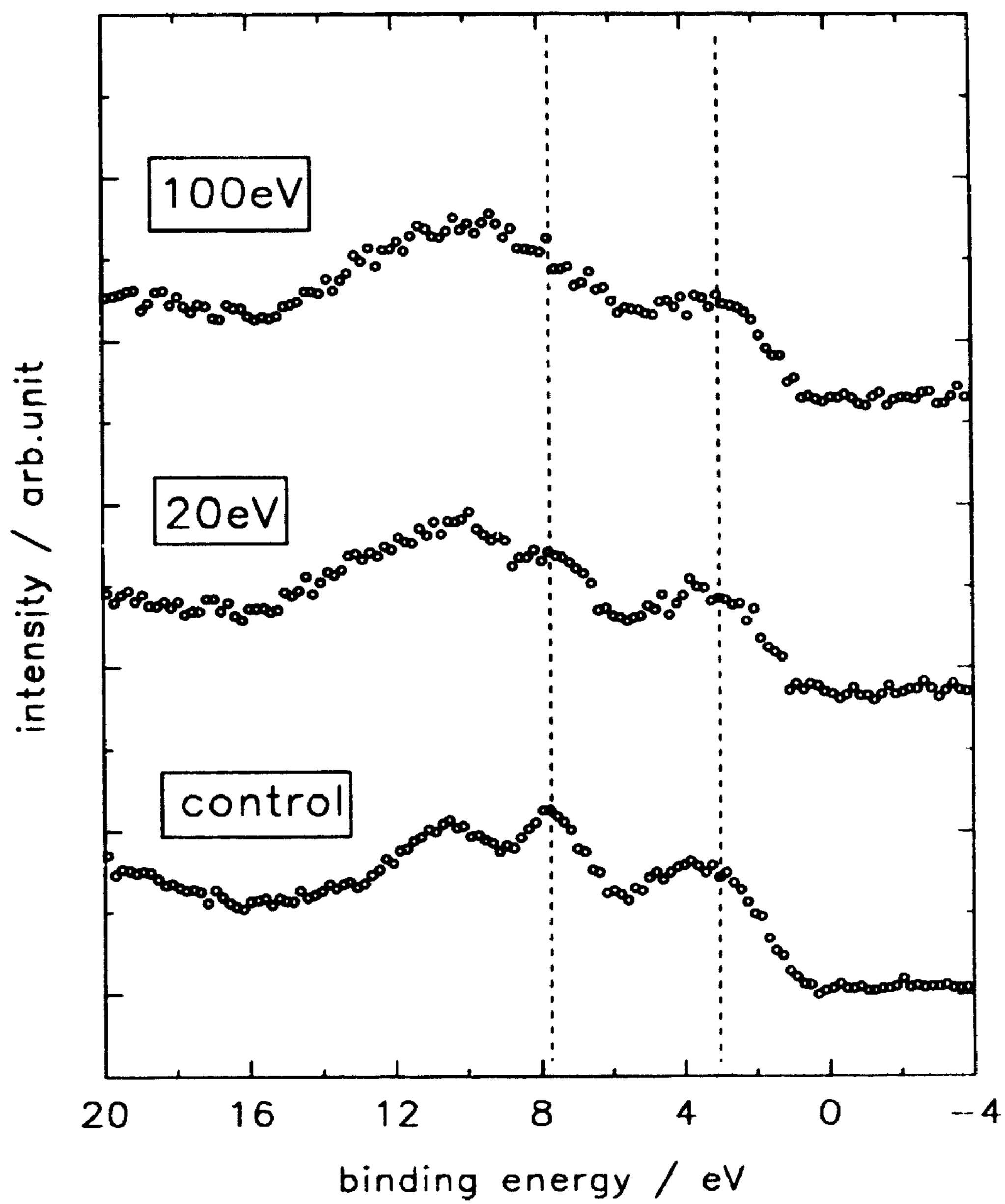
100eV
20eV
control
intensity / arb.unit
20
16
12
8
4
0
−4
binding energy / eV

constant Therefore, the changes in the valence band characterize the major effects of surface crystalline damage.

5.3.3 Effect of vacuum heating to 800°C

Figure 5.8 shows the effects of heating the samples from Figure 5.4 bombarded with F^+ at 20 to 100eV and constant dose of $3x10^{16}/cm^2$. The surface F/Si ratio was reduced after vacuum heating at 800°C for 30min with a 54% decrease at 20eV and 33% decrease at 100eV relative to the room temperature values. Although there was a detectable reduction of surface fluorine after the samples were heated, there did not appear to be a clear dependence in surface F/Si ratio with ion bombardment energy because of the relatively large scatter in the data. The results suggest that the surface F was not stable thermally at these low energies investigated.

The diffusion of F implanted into Si(100) at 30keV at low doses of $1x10^{12}$ and $1x10^{13}/cm^2$ has been reported [5.66] to display an anomalous out-diffusion behaviour with F depletion in Si at temperatures above 500°C. This suggests that preferential thermally-activated diffusion to the Si surface occurs at a greater rate than diffusion into the bulk at higher temperatures. While the driving force for such a behaviour has not been identified [5.66], electric field effects due to the presence of the electronegative F atoms were not considered to be a dominant mechanism. It is however plausible that the defect migration towards the surface promotes the surface segregation of fluorine [5.67]. This surface segregation is then manifested as a reduction in fluorine after heating to 800°C.

Figure 5.8 Effect of vacuum heating to 800°C on surface F/Si composion ratio for the ion kinetic energy range of 20 to 100eV at a constant dose of $3x10^{16}$ions/cm^2.

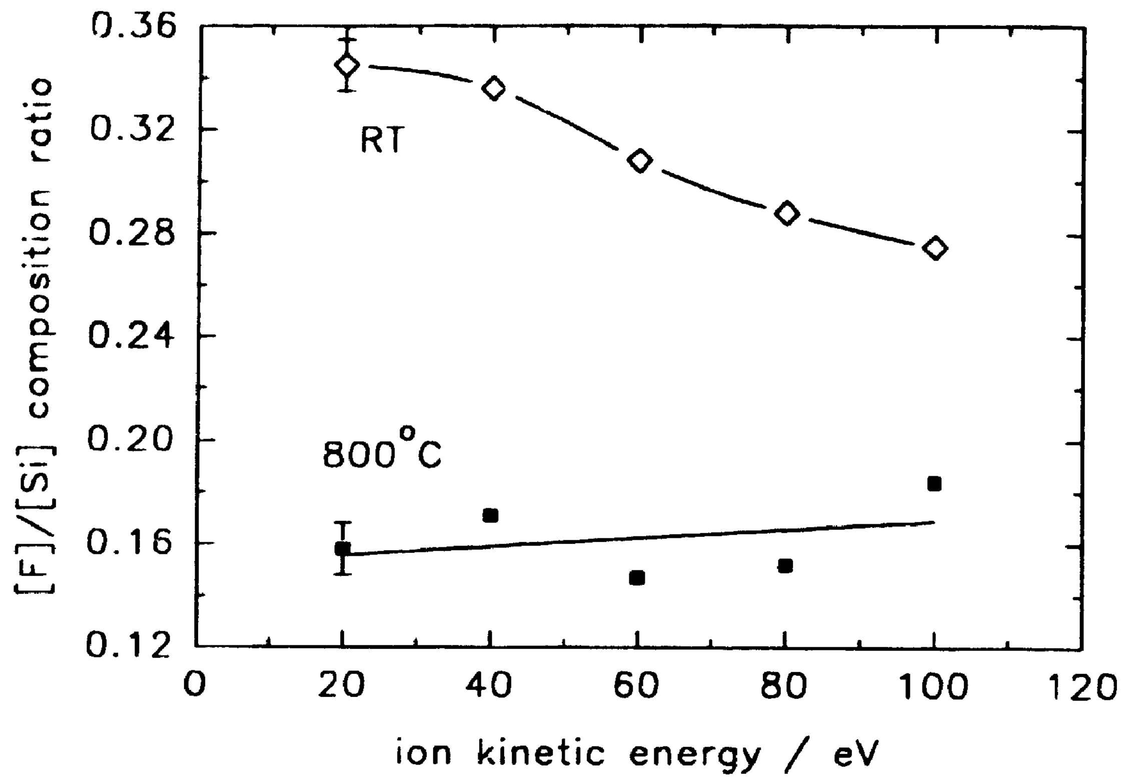
[F]/[Si] composition ratio
0.36
0.32
0.28
0.24
0.20
0.16
0.12
RT
800°C
0
20
40
60
80
100
120
ion kinetic energy / eV

5.4 Conclusions

The development of a fluorosilyl (SiF_n, n=1 - 4) species surface layer and silicon surface crystalline disorder were observed for increasing ion doses at a constant F^+ ion kinetic energy of 100eV. The fluorine ion bombardment was also seen to induce type-inversion of the p-type silicon likely from an increase in conduction electrons provided from the fluorine atoms. These results also showed that the effects of F^+ ion bombardment energy between 20 and 100eV (dose of $3x10^{16}/cm^2$) on the surface residual damage induced on Si(100) were manifested as greater F incorporation and Si surface disorder, the development of a thin fluorosilyl layer, and the thermal instability of the incorporated fluorine was observed in this energy range. These distinct surface properties serve to illustrate the surface residual damage induced by reactive F^+ ion bombardment of Si(100).

REFERENCES

5.1 S.K. Ghandhi, VLSI Fabrication Principles, J. Wiley & Sons, New York, 1983

5.2 R.C. Jaeger, Introduction to Microelectronic Fabrication, Modular Series on Solid State Devices, Vol. 5, edited by G.W. Neudeck, R.F. Pierret, Addison-Wesley, Reading, 1988.

5.3 J.L. Mauer, J.S. Logan, L.B. Zielinski, G.C. Schwartz, J. Vac. Sci. Technol., 15, 1734, 1978.

5.4 J.W. Coburn, H.F. Winters, J. Vac. Sci. Technol., 16, 391, 1979.

5.5 J.W. Coburn, Plasma Chem. Plasma Proc., 2, 1, 1982.

5.6 J.W. Coburn, H.F. Winters, Annu. Rev. Mater. Sci., 13, 91, 1983.

5.7 H.F. Winters, J.W. Coburn, T.J. Chuang, J. Vac. Sci. Technol., B1, 469, 1983.

5.8 Y.Y. Tu, T.J. Chuang, H.F. Winters, Phys. Rev. B, 23, 823, 1981.

5.9 D.L. Flamm, V.M. Donnelly, J.A. Mucha, J. Appl. Phys., 52, 3633, 1981

5.10 J.A. Mucha, V.M. Donnelly, D.L. Flamm, L.M. Webb, J. Phys. Chem., 85, 3529, 1981

5.11 M.J. Vasile, F.A. Stevie, J. Appl. Phys., 53, 3799, 1982.

5.12 H.F. Winters, F.A. Houle, J. Appl. Phys., 54, 1218, 1983.

5.13 D.E. Ibbotson, D.L. Flamm, J.A. Mucha, V.M. Donnelly, Appl. Phys. Lett., 44, 1129, 1984

5.14 C.D. Stinespring, A. Freedman, Appl. Phys. Lett., 48, 718, 1986.

5.15 F.A. Houle, J. Appl. Phys., 60, 3018, 1986.

5.16 N.D. Shinn, J.F. Morar, F.R. McFeely, J. Vac. Sci. Technol., A2, 1593, 1984.

5.17 F.R. McFeely, J.F. Morar, N.D. Shinn, G. Landgren, F.J. Himpsel, Phys. Rev.

B, 30, 764, 1984.

5.18 F.R. McFeely, J.F. Morar, F.J. Himpsel, Surf Sci., 165, 277, 1986

5.19 F.R. McFeely, B.D. Sullivan, J.A. Yarmoff, U O Karlsson, in Proc Eighth Int Symp. on Plasma Chemistry, edited by K Akashi, A Kinbara, International Union of Pure and Applied Chemistry, Tokyo, 927, 1987

5.20 J.R. Engstrom, M.M. Nelson, T. Engel, Phys. Rev B, 37, 6563, 1988

5.21 J.R. Engstrom, M.M. Nelson, T. Engel, Surf. Sci., 215, 437, 1989

5.22 M.J. Bozack, M.J. Dresser, W.J. Choyke, P.A. Taylor, J T Yates, Surf Sci., 184, L332, 1987.

5.23 A.L. Johnson, M.M. Walczak, T.E. Madey, Langmuir, 4, 277, 1988

5.24 M. Seel, P.S. Bagus, Phys. Rev B, 28, 2023, 1983

5.25 P.S. Bagus, in Plasma Synthesis and Etching of Electronic Materials, edited by R.P.H.Chang, B. Abeles, MRS Symposia Proceedings No 38, Materials Research Society, Pittsburgh, 179, 1985.

5.26 F. Illas, J. Rubio, J.M. Ricart, Phys. Rev B, 31, 8068, 1985

5.27 S.M. Mohapatra, B.N. Dev, K.C Mishra, N Sahoo, W M Gibson, T P Das, Phys. Rev. B, 38, 12556, 1988.

5.28 B.J Garrison, W.A. Goddard III, Phys Rev B, 36, 9805, 1987

5.29 P.J. van den Hoek, W. Ravene, E J Baerends, Phys Rev B, 38, 12508, 1988

5.30 C.G. van de Walle, Y. Bar-Yam, F R McFeely, S T Pantelides, J Vac Sci Technol., A6, 1973, 1988.

5.31 C G. van de Walle, Y. Bar-Yam, F R McFeely, S T Pantelides, Phys Rev Lett., 61, 1867, 1988.

5.32 B I Craig, P V Smith, Surf Sci, 239, 36, 1990

5.33 G.S. Oehrlein, R.M. Tromp, J.C. Tsang, Y.H. Lee, E.J. Petrillo, J. Electrochem Soc., 132(6), 1441, 1985

5.34 H.F. Winters, J.W. Coburn, Surf. Sci. Rep., 14, 161, 1992 and references therein

5.35 S. Kostic, D.G. Armour, G. Carter, in Materials Modifications by High-fluence Ion Beams, edited by R. Kelly, M. Fernanda da Silva, Kluwer Academic Publishers, Dordrecht, 237, 1989.

5.36 A.H. Al-Bayati, K.G. Orrman-Rossiter, R. Badheka, D.G. Armour, Surf. Sci., 237, 213 (1990)

5.37 A.H. Al-Bayati, K.G. Orrman-Rossiter, D.G. Armour, Surf. Sci., 249, 293, 1991

5.38 P.K. Charvat, E.E. Krueger, A.L. Ruoff, J. Vac. Sci. Technol., B4(4), 812, 1986

5.39 S. Tachi, S. Okudaira, J. Vac. Sci. Technol., B4(2), 459, 1986

5.40 J.W. Coburn, private communication

5.41 G.S. Oehrlein, J. Vac. Sci. Technol., A11(1), 34, 1993

5.42 M.Y. Tsai, D.S. Day, B.G. Streetman, P. Williams, C.A. Evans, J. Appl. Phys., 50, 188, 1979

5.43 R.G. Wilson, J. Appl. Phys., 54, 6879, 1983

5.44 H.F. Winters, I.C. Plumb, J. Vac. Sci. Technol., B9,197, 1991

5.45 C.W. Lo, D.K. Shuh, V. Chakarian, K.A. Germain, J.A. Yarmoff, in Proc. 1990 Symp. on Dry Process, Tokyo, 1990

5.46 T.A. Carlson, Photoelectron and Auger Spectroscopy, Plenum Press, New York, 1975

5.47 B.J. Garrison, W.A. Goddard III, J Chem. Phys., 87, 1307, 1987

5.48 W.M. Lau, J Appl Phys., 67(3), 1504, 1990

5.49 L J. Huang, W.M. Lau, Appl Phys Lett, 60(9), 1108, 1992

5.50 L.J. Huang, W.M. Lau, J. Vac. Sci. Technol, A10(4), 812, 1992

5.51 H. Matsumura, Y. Nakagome, S Furukawa, J Appl Phys., 52, 291, 1981

5.52 A. Madan, in Hydrogenated Amorphous Silicon, Topics in Applied Physics, Vol.5, edited by J.D Joannopoulous, G Lucovsky, Springer, Berlin, 1984

5.53 J. Ishikawa, I.H. Wilson, J Non-Cryst Solids, 45, 271, 1981

5.54 S.P. Wong, I.H. Wilson, W.Y Cheung, W.K Mok, S K Hark, Nucl Instr Meth B, 67, 481, 1992

5.55 S.R. Kasi, H. Kang, C.S. Sass, J W Rabalais, Surf Sci Rep, 10, 1, 1989

5.56 T.A. Schoolcraft, B.J. Garrison, J Vac Sci Technol, A8(4), 3496, 1990

5.57 P. Sigmund, Phys. Rev, 184, 383, 1969

5.58 P. Sigmund, Phys. Rev, 187, 768, 1969

5.59 J Roth, in Sputtering by Particle Bombadment II, Topics in Applied Physics, Vol.52, edited by R. Behrisch, Springer, Berlin, 1983

5.60 P C Weakliem, C J. Wu, E.A Carter, Phys Rev Lett, 69,(1), 200, 1992

5.61 C W Wild, P Koidl, Appl Phys Lett., 54, 505, 1989

5.62 A Manenschijn, W J Goedheer, J Appl Phys, 69, 2923, 1991

5.63 A Dilks, in Electron Spectroscopy Theory, Techniques and Applications, Vol 4, Academic Press, London, 278, 1981

5.64 T.J Chuang, H F Winters, J W Coburn, Appl Surf Sci, 2, 514, 1978

5.65 M Niwano, Y Takeda, K Kurita, N Miyamoto, J Appl Phys, 72(6), 1992

5.66 S P Jeng, T P Ma, R Canteri, M Anderle, G W Rubloff, Appl Phys Lett

61(11), 1310, 1992.

5.67 B. Yu, N. Konuma, E. Arai, Y. Ohji, Y. Nishioka, J. Appl. Phys., 70, 2408, 1991

CHAPTER 6.

SURFACE REACTIONS INDUCED BY CF^+ ION BOMBARDMENT

6.1 Introduction

In fluorocarbon reactive ion etching of silicon, the residual damage is dominated by the ion bombardment because reactions with the radicals of the plasma are normally confined to the surface, but ion bombardment leads to sub-surface reactions. Such sub-surface physical damage and impurity incorporation have been clearly shown, e.g. in previous work by Oehrlein and coworkers [6.1-3]. In these previous studies, the effects of all reactive species contributing to the plasma etching of silicon were examined. However, the individual contributions of fluorocarbon ions were not identified because the plasma RIE process is not conducive to ion mass-separation. It is of both fundamental as well as technological interest to understand the role of ion bombardment in RIE [6.4]. With this interest in mind, there have been a number of recent studies using ion beam methods to understand the etching mechanisms present from fluorocarbon reactive ion etching of silicon. Tu and coworkers [6.5] have studied the effects of Ar^+ and a CF_3^+ ion beam (which was not mass separated) bombardment at 500eV on Si and SiO_2 in the presence of a flux of XeF_2. From the AES results, it was concluded that CF_3^+ ion bombardment at 500eV produced significant amounts of surface carbon and fluorine. However, the chemical nature of the surface species was not identified. Chuang and coworkers [6.6] have studied the surface modifications of Si induced by CF_3^+ ion beam

bombardment at 500eV and 2000eV by XPS and AES. The results show the development of silicon carbide, fluorinated graphite and Si-F species as a function of relative ion fluence at 500eV However, the ion doses were not stated. As the ion dose increases, a fluorocarbon layer begins to form. In their study, the XPS instrument resolution was not sufficiently sensitive to resolve the different surface carbon chemical species. Tachi and coworkers [6 7,8] have studied the surface deposition and etching of sputter-deposited Si by mass-separated CF^+ ion beam bombardment between 100eV and 3000eV. They reported that carbon and carbonaceous polymer deposition occurs in the range of 100eV to 700eV Above 700eV, etching takes place principally via physical sputtering processes The chemical reaction probability was found to be of the order of 10^{-1}. However, the ion kinetic energy range below 100eV was not investigated. Gray and coworkers [6 9] have studied the synergistic effects of energetic Ar^+ ion bombardment along with CF_2 radical and atomic F fluxes on the etching/deposition properties of fluorocarbon species with polysilicon The effects of F and CF_2 radical-to-ion flux ratio on fluorocarbon film formation and etching yields were ascertained. Their results show that the CF_2 radical possesses a high sticking probability on polycrystalline Si, and this results in the formation of a deposited film. This direct sticking of CF_2 results in a reduction of Ar^+ sputter rates by almost 70% below the physical sputtering rate. Such work focussed on the etching yields, and the surface residual damage was not characterized The effects of CF radical exposure are expected to behave similarly, however no published studies have been found during the course of this thesis

In this chapter, the effects of reactive CF^+ ion interaction with single crystal silicon at low ion kinetic energies were studied in terms of the surface modifications induced by

the bombardment. The ion energy range of interest was 2eV to 100eV. In current generation RIE processing with fluorocarbon glow discharges, collisional processes in the plasma sheath region can lower the maximum kinetic energy (a few hundred electronvolts) of the reactive species [6.1]. Therefore, reactive ions and neutrals possessing a spread of energies ranging from the maximum energy down to almost no kinetic energy (i.e. 500eV down to 0eV) bombard the sample surface. In addition, it has been reported [6.10] that ion energies near and below 100eV may be adopted in future dry etching schemes because of inherently less damage to the Si induced by energetic reactive ion exposure. Hence, it is of both fundamental and technological interest to study the surface reactions induced by low energy molecular fluorocarbon ion bombardment of Si and to characterize the residual damage layer (this includes any deposited films, Si compound formation and depth distribution of compounds).

Due to the complexity of the composition of the etching plasma, the contributions of the different reactive ions to the residual damage, as well as to the etching mechanisms, are not known. In order to generate more fundamental understanding of the RIE process, various research groups have recently resorted to the use of mass-separated low energy reactive ion beams [6.8,11-15] to isolate the various reactive ion species, and to the monitoring of the associated surface reactions with a variety of analytical techniques including *in situ* analyses [6.13-15]. This work incorporated the use of a mass-separated low energy ion beam UHV system to generate pure CF^+ ions. The Si surfaces were analyzed *in-vacuo* by XPS before and after ion beam bombardment at known kinetic energies and doses.

The effects of ion kinetic energy were characterized in terms of the various surface

chemical states induced by the bombardment. The results showed that with an ion kinetic energy of 2eV, which was much lower than the C-F bond energy of about 5eV, molecular adsorption took place At a bombardment energy of 10eV, dissociative chemisorption was observed but the reaction was confined to the top surface with disproportionation of CF as the main route and little fluorination of silicon. With an ion energy of 100eV, the atomic fragments generated by the CF dissociation possessed enough energy to penetrate below the silicon surface. It was found that silicon carbide and fluorosilyl species comprised the modified surface region and that the fluorosiiyl layer was situated closer to the surface than the carbide layer. This work shows that distinct surface reactions may be chemically switched between the CF^+ ion and the silicon surface as a function of the ion kinetic energy.

6.2 Experimental procedure

Samples were prepared from device quality p-type Si(100) wafers implanted with boron at 16keV and a dose of $1.6 \times 10^{15}/cm^2$ followed by rapid thermal annealing at 1050°C for 30s The samples were wet-etched in a dilute hydrofluoric acid (HF) and deionized water solution for 30s to 45s and blown dry with N_2 gas for 60s before loading into the LEIB system No further surface cleaning procedure was applied prior to or after ion beam bombardment

A mass-separated low energy ion beam of CF^+ ions was produced using a CF_4 plasma in the LEIB ion source A detailed description of the LEIB system has been

reported in Chapter 3, section 3.4. The pure CF^+ ion beam was directed at normal incidence onto the Si sample surface at an ion kinetic energy of 100eV. A positive bias was applied to the sample holder in order to offset the energy of the impinging positive, molecular ions down to between 100eV and 2eV. The ion dose was $1\times10^{16}/cm^2$ for the 2eV and 10eV cases, while the ion energies between 20eV and 100eV were delivered onto the sample with a constant dose of $3\times10^{16}/cm^2$. Since the areal atom density in silicon is approximately $2\times10^{15}/cm^2$, these doses were considered to be sufficient to produce near steady-state surface modifications or residual damage production. All ion bombardment experiments were conducted at room temperature. Once the sample was exposed to the ion beam, it was transferred under vacuum (pressure less than 1×10^{-7} torr) to a separate UHV system containing the XPS spectrometer for surface analysis.

XPS analysis (see Chapter 3, section 3.5) was initially performed with the detector placed at a polar photoemission angle of 55° after vacuum transfer. Subsequent angle - dependent XPS (see Chapter 3, section 3.5.4) was carried out by first transferring the sample to a specially constructed holder suitable for ARXPS. This procedure resulted in the samples being exposed to air for less than 1min.

6.3 Results and discussion

6.3.1 Effect of CF^+ ion kinetic energy

The effects of CF^+ ion kinetic energy can be seen from the surface [CF] to [Si]

ratio, in Figure 6 1a Below 40eV ion energy, there was a fluorocarbon to Si ratio near 5 As the ion energy increased between 40eV and 60eV, there was appreciable fluorocarbon deposition At 80eV and 100eV, the surface [CF]/[Si] ratio was lower than initially seen at 20eV Assuming a uniform overlayer model (see Chapter 4), the fluorocarbon film thickness was determined and displayed as a function of ion kinetic energy in Figure 6.1b. Thus there appeared to be three distinct regimes of surface modification associated with changes in ion kinetic energy over the range of 20eV to 100eV

The effects of CF^+ ion exposure at the very low kinetic energies of 2eV and 10eV can be seen from the C1s and Si2p core-level spectra in Figure 6.2 and 6.3. At 2eV, the C1s results indicated the presence of a CF_1-type surface species at about 286.8eV binding energy in addition to the adventitious hydrocarbon surface contamination at a binding energy of 284 6eV The C-F bond energy has been reported to be approximately 5eV [6 16] In this case, the kinetic energy of the molecular ion is insufficient to cause dissociation upon impact with the Si surface. There were no other stable fluorocarbon species detected as a result of this molecule adsorbing onto the Si surface. The surface chemistry of this system is not known, however it is plausible that the ion kinetic energy of 2eV is insufficient in promoting the formation of any reaction intermediates leading to the dissociation of CF on the surface.

For CF^+ ions at 2eV and dose of 1×10^{16} /cm^2, approximately 10 monolayers were delivered onto the surface Under the experimental conditions of this study, an HF-etched silicon surface always has surface adventitious carbon amounting to about 30%, or about 2 monolayers equivalent Most of this surface carbon desorbs with heating between 200

Figure 6.1 Effect of ion kinetic energy on (a) [CF]/[Si] surface composition ratio, (b) estimated fluorocarbon film thickness

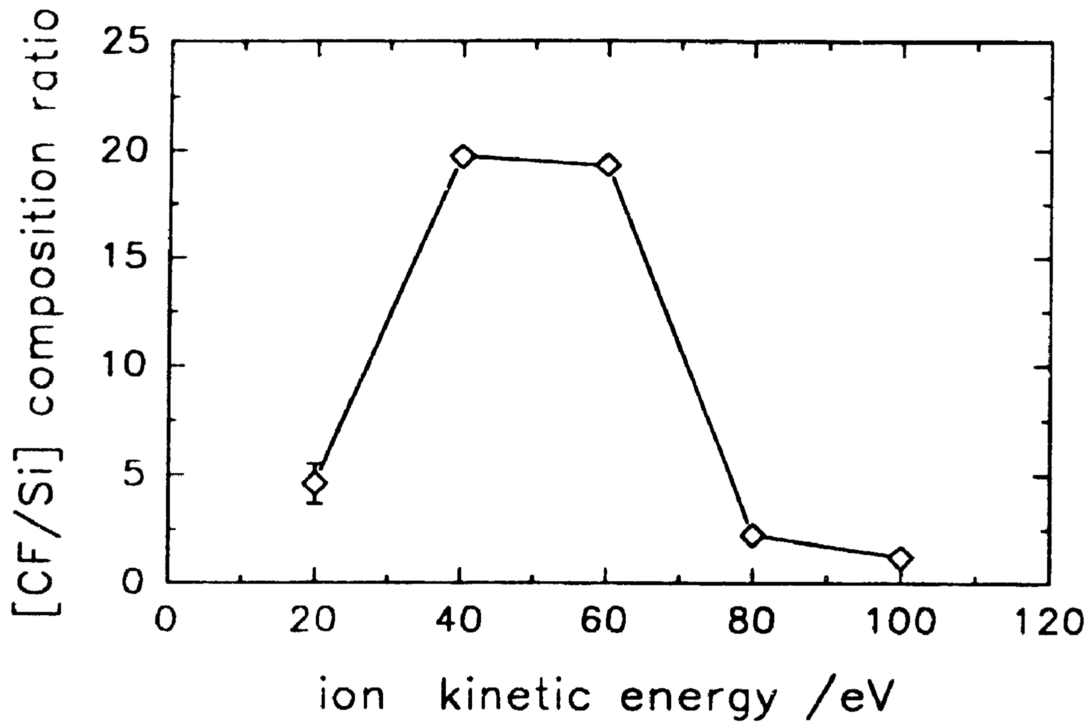
[CF/Si] composition ratio
25
20
15
10
5
0
0
20
40
60
80
100
120
ion kinetic energy /eV

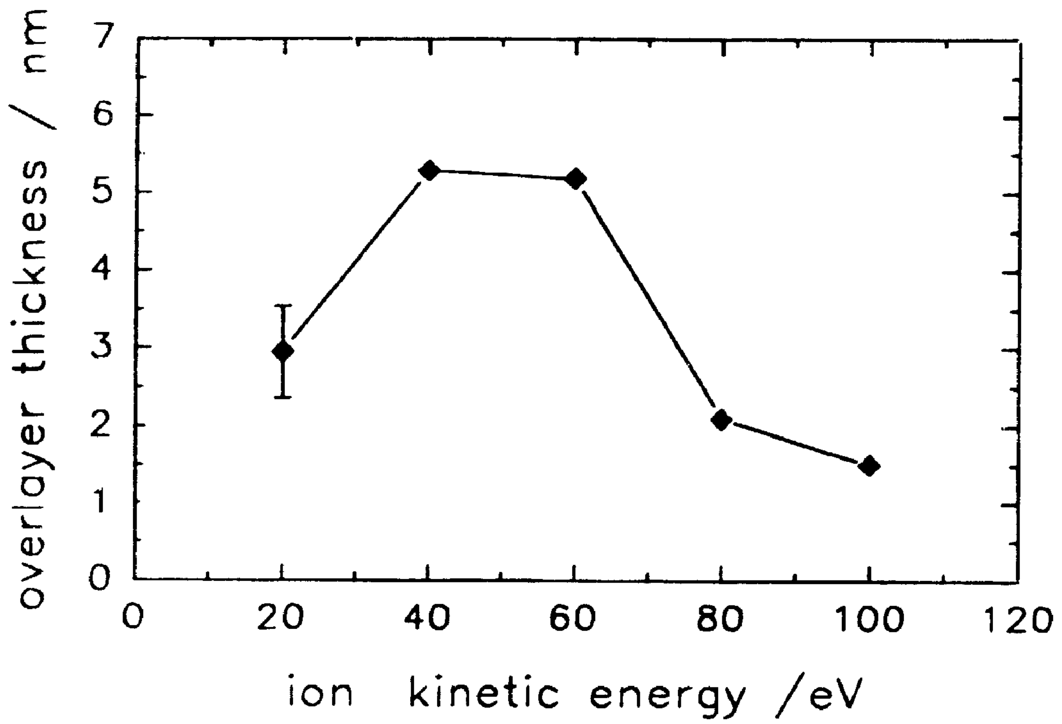
overlayer thickness / nm
7
6
5
4
3
2
1
0
0
20
40
60
80
100
120
ion kinetic energy /eV

Figure 6.2 High resolution C1s core-level spectra of the Si surfaces bombarded by 2eV and 10eV CF^+ ions at a dose of $1 \times 10^{16}/cm^2$

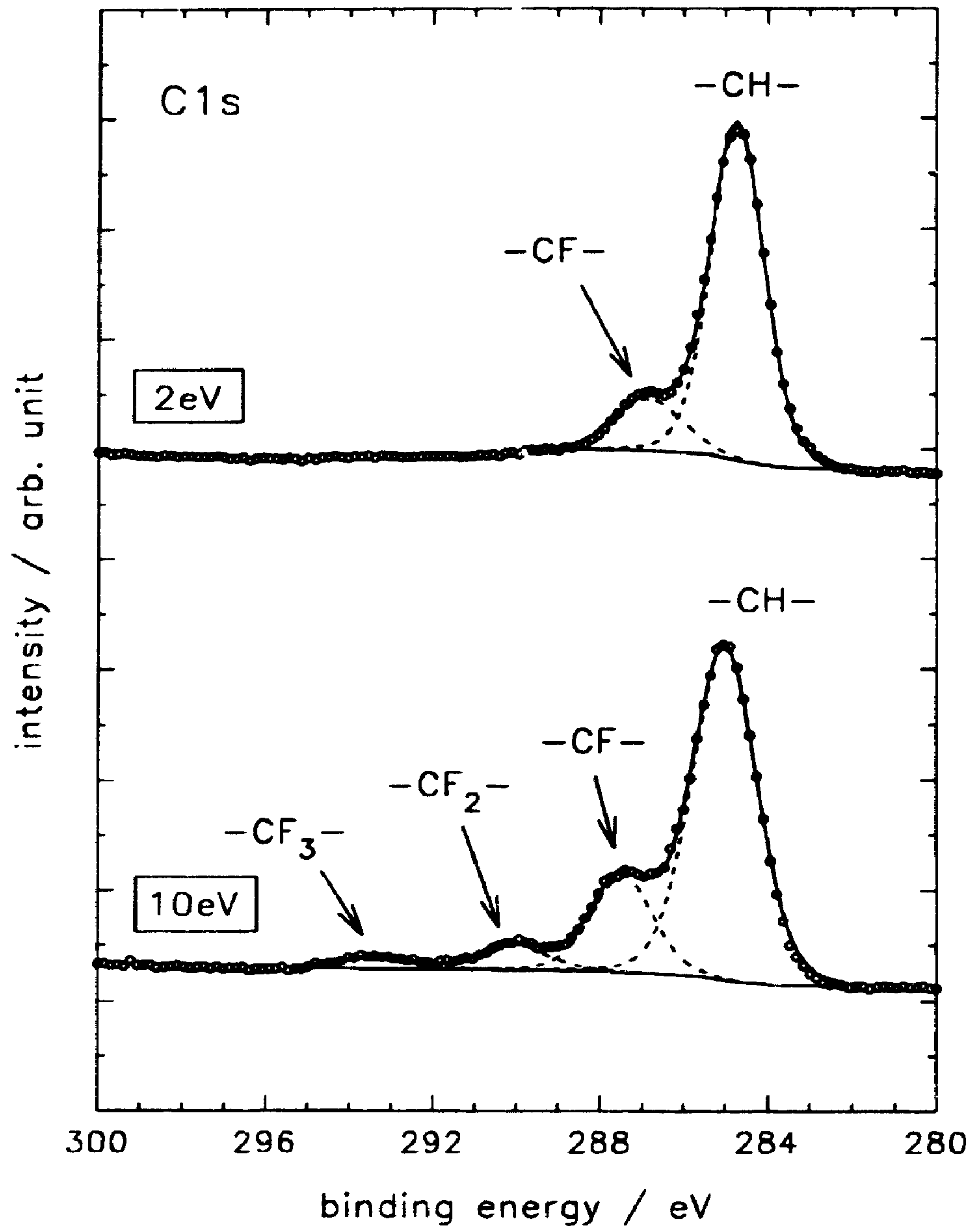
C1s
-CH-
-CF-
2eV
-CH-
-CF-
$-CF_2-$
$-CF_3-$
10eV
intensity / arb. unit
300
296
292
288
284
280
binding energy / eV

Figure 6.3 **High resolution Si2p core-level spectra corresponding to Figure 6.2.**

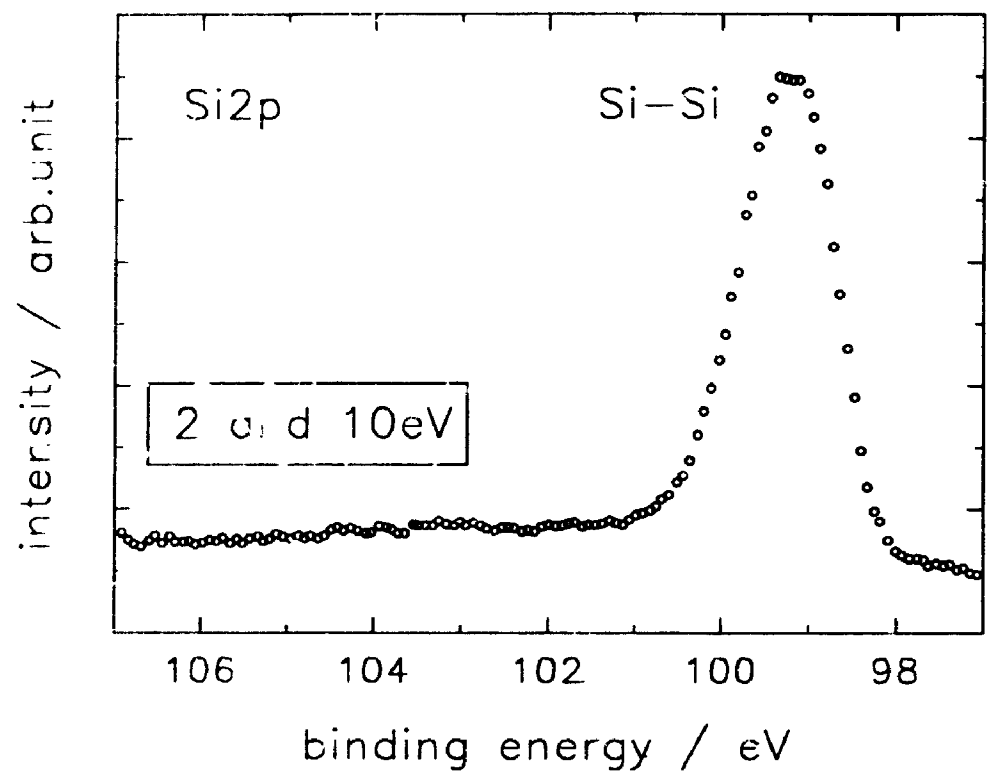
Si2p
Si–Si
intensity / arb.unit
106
104
102
100
98
binding energy / eV

and 300°C. Hence, this adventitious contamination is only weakly bound to the silicon surface. It was thus assumed that the original surface contamination desorbed during the early stages of CF^+ ion bombardment. Subsequently, the adsorption of CF took place onto the silicon surface, and after the ion bombardment was terminated, some surface adventitious carbon was accumulated back on top of the adsorbed CF layer. With such an assumption, chemical composition calculations showed that a CF layer approximately 1.4nm in thickness (or 3-4 equivalent monolayers) developed from the ion bombardment. These results suggest that after surface neutralization, some of the incoming CF species were adsorbed as molecules (i.e. molecular adsorption) on the silicon surface, and some CF species were scattered from the silicon. A fluorosilyl layer on the Si surface has been associated with reactive etching by fluorine atoms [6.17]. In this study there were no appreciable fluorosilyl species identified from the Si2p spectral results (Figure 6.3). Hence, the CF^+ exposure at 2eV does not etch silicon but leads to fluorocarbon film deposition.

For the case of CF^+ ions with a kinetic energy of 10eV, the C1s core-level spectrum shows peaks identified with CF_3-, CF_2- and CF_1-type species on the surface [6.18]. It is postulated that the ion kinetic energy of 10eV was high enough to promote the fragmentation of the incoming molecular species into carbon and fluorine atoms. This phenomena is consistent with previously reported work [6.19-21] of energetic (~10eV) molecular ions striking a solid surface and dissociating upon impact. The fluorine atoms generated by the CF dissociation can then react with the adsorbed CF or carbon atoms for the production of CF_2 and CF_3.

Although fluorination of silicon is also a conceivable reaction pathway, the

corresponding Si2p core-level spectrum (Figure 6.3) indicates that there was little, if any, chemical interaction with the Si surface. The negligible reaction with silicon is attributed to the fact that the surface Si atoms are terminated with hydrogen after the HF-etch (see Chapter 3, section 3.2) and that the atomic fragments carried insufficient energy to penetrate below the silicon surface. The confinement of the reaction to the top surface thus leads to more fluorine-flucrocarbon than fluorine-silicon interactions. In addition, the 10eV energy from the ion bombardment may not be enough to cause displacement of Si atoms from equilibrium lattice positions since this energy is about 15eV [6.22] for bulk silicon. With Si atom displacement, bond breaking is likely to occur and these Si dangling bonds may then react with the carbon and fluorine. The results indicate that CF^+ bombardment at 10eV, not unlike the radical-surface reactions in a CF_4/H_2 plasma where CF radicals are abundant [6.17], contributes to fluorocarbon polymer formation. This formation is part of the residual damage developed.

From Figure 6.3, the Si2p core-level corresponding to 2eV and 10eV CF^+ ion beam exposure were practically identical with that of an unbombarded silicon surface. Any chemical reactions with Si would cause a change in the oxidation state and this change would be manifested as peak components towards higher binding energy from the elemental Si peak. The absence of any such features towards higher binding energy in Figure 6.3 supports the idea that no surface chemical reactions occur between the CF^+ molecular ion and the Si substrate. Therefore, the interaction between this molecular ion and the hydrogen-terminated Si surface at such low energies was confined to the top surface layer with little subsurface penetration and reaction with the Si.

At an ion kinetic energy of 20eV and dose of $3x10^{16}/cm^2$, the C1s spectrum was

similar to the 10eV case (Figure 6.2) with the relative abundances of $C\text{-}F_n$ (n=1,2,3) species decreasing with increasing F bonds to C. The Si2p spectrum was also identical to the 10eV case. As the ion kinetic energy was increased from 20 to 40 to 60eV with the same constant dose of $3x10^{16}/cm^2$, the relative amounts of surface C and F increased significantly (Figure 6.1). However, the C1s spectra remained the same. This indicates that the type and relative abundances of surface fluorocarbon species were insensitive to the incoming ion energy in the range of 20eV to 60eV. Hence, fluorocarbon deposition was the dominant form of residual damage at these energies.

In this same energy range, the Si2p spectra for the 40eV and 60eV cases showed the development of a weak, broad component towards higher binding energy than the elemental Si peak. This suggests that there was a limited interaction with the Si surface. If it is assumed that the C and F fragments carry energy equal to their respective mass fractions, then the C and F atoms would possess 40% and 60% of the total energy, respectively. In the 40eV molecular ion case, the F atom would in principle deliver 24eV energy to the surface. This energy is possibly sufficient for some of the F atoms to penetrate the fluorocarbon layer and the silicon surface, thereby enhancing the F-Si reaction probability. Such an ideal fluorosilyl reaction would result in an observed broad component in the Si2p spectrum. However, the formation of a fluorocarbon film layer was greatest at these ion kinetic energies with limited silicon-fluorine species development because of very little intensity detected from the Si2p spectrum corresponding to SiF components.

The dramatic increase in surface fluorocarbon species between 20eV and 40eV ion energy (Figure 6.1) was likely due to different surface phenomena. At 40eV (and also

60eV), there was optimal fluorocarbon film deposition on the Si surface. This indicates that at these energies, the reaction probability for film deposition was increased. For the 20eV case, deposition does occur, but to a lesser extent. A large contribution of the CF^+ molecules impinging on the surface may have scattered off the surface. This surface scattering phenomena has been reported [6.23] for BF^+ ion scattering below 100eV. Therefore, at these low energies (20eV to 40eV) there was a competition between the two different reaction pathways of molecular ion surface scattering and fluorocarbon film deposition.

For CF^+ ions with kinetic energies of 80eV and 100eV, Figure 6.4 shows the C1s spectra. Ion dissociation has taken place. However, the surface carbon species were in general different than those present at ion kinetic energies between 10eV and 60eV. The Si surface after 80eV CF^+ ion bombardment had less fluorocarbons in comparison to the 40eV and 60eV cases (Figure 6.1), as well as less fluorinated carbons (for example Figure 6.2 the 10eV case). The detection of peaks assigned to species of CF_1 and $(C_1F_x)_n$ with $x<1$ does suggest that some fluorocarbon deposition was still taking place, however, this deposition was not as great as previously discussed. The presence of silicon carbide (C-Si) species at a binding energy of 283.5eV was identified from the C1s core-level spectrum. This peak assignment is consistent with previously reported signature spectra for silicon carbide [6.24]. Therefore, reaction with the underlying Si was beginning to occur at this ion energy.

At an ion kinetic energy of 100eV, the C1s spectrum shows the presence of only C-Si at 283.5eV binding energy. The peak at a binding energy of 284.6eV is likely from amorphous carbon present on the surface due to the dissociation of the incoming CF^+ ions

Figure 6.4 High resolution C1s core-level spectra of Si surface after 80eV and 100eV CF^+ ion bombardment at a dose of $3x10^{16}/cm^2$

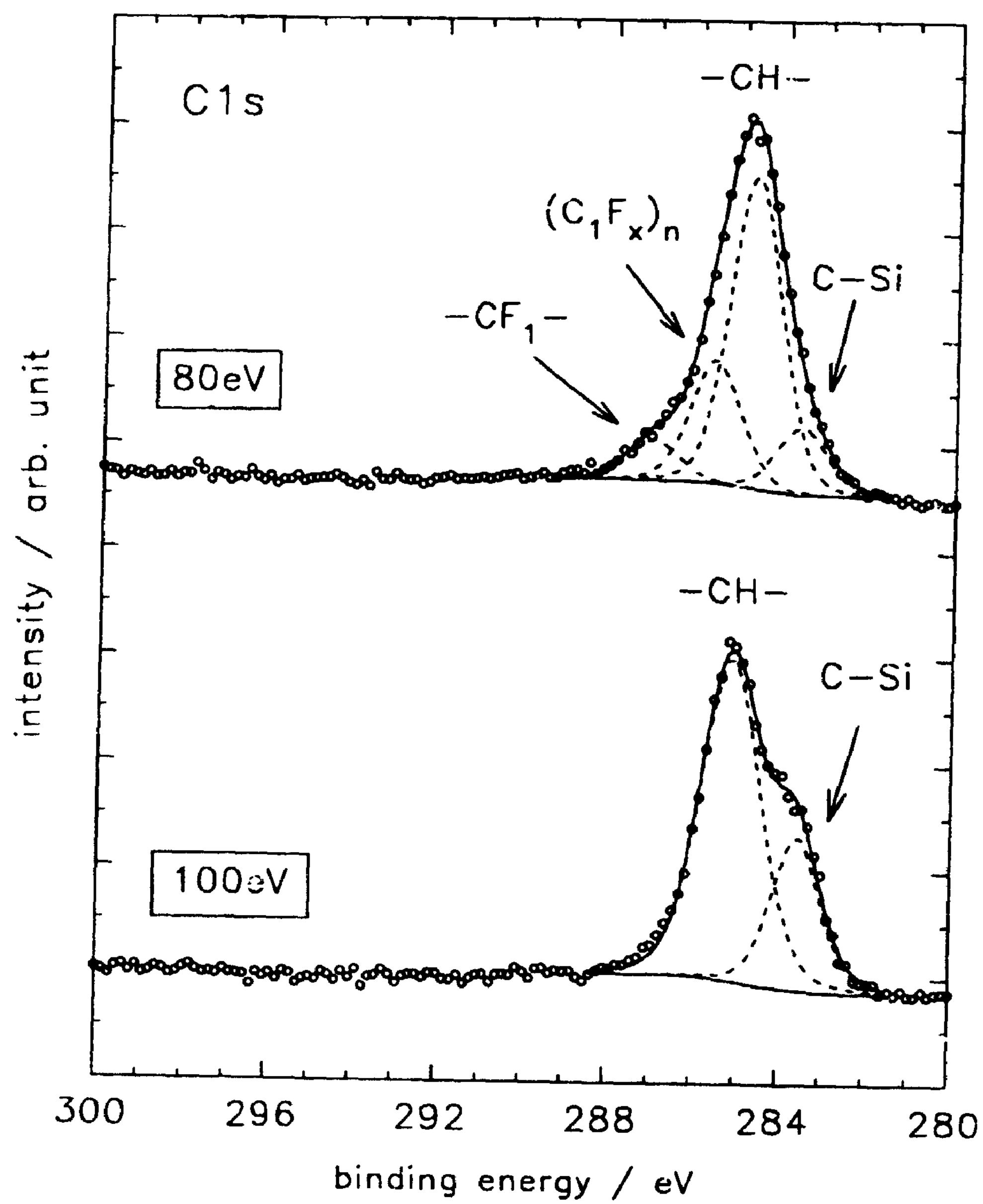
C1s
-CH-
$(C_1F_x)_n$
C-Si
$-CF_1-$
80eV
-CH-
C-Si
100eV
intensity / arb. unit
300
296
292
288
284
280
binding energy / eV

and to the accumulation adventitious hydrocarbon contamination after ion bombardment At 100eV, complete CF^+ ion dissociation has occurred. The absence of any fluorocarbon species suggests that the reaction pathway towards film deposition has been suppressed while that of Si reaction has been enhanced. At 80eV ion energy, the CF^+ molecular ion dissociates on impact with the surface, and there is still some C-F interaction, but most of the C and F atomic fragments possess sufficient kinetic energy to penetrate below the Si surface and break Si-Si bonds in the process. Such subsurface penetration allows some of the C to react with the Si. For the case of 100eV ion energy, the C-Si reaction probability was even greater than the 80eV case with the result that there were no stable fluorocarbon species. Thus the principle form of residual damage was Si-containing compound formation with minor stable surface fluorocarbon species

Figure 6.5 illustrates the Si2p peak profiles for surfaces bombarded by 80eV and 100eV CF^+ ions. The elemental Si peak was at 99eV binding energy and a broad, less intense peak was present towards higher binding energy. The unresolved components due to SiF_n (n=1,2,3) and Si-C species are labelled in Figure 6 5 If the density of the reaction layer was assumed to be the same as for SiO_2, then the layer thickness may be calculated from [6 25]:

$$d\ (nm) = \lambda \cos\theta \ln\left([I_o n_s \lambda_s]/[I_s n_o \lambda_o] + 1\right)$$

The Si reaction layer thickness was estimated to be 2 2nm for the 100eV ion bombardment and 1 5nm for the 80eV ion energy The higher energy ion exposure produced a thicker reaction layer This may be the result of a greater penetration depth

Figure 6 5 High resolution Si2p core-level spectra corresponding to Figure 6 4

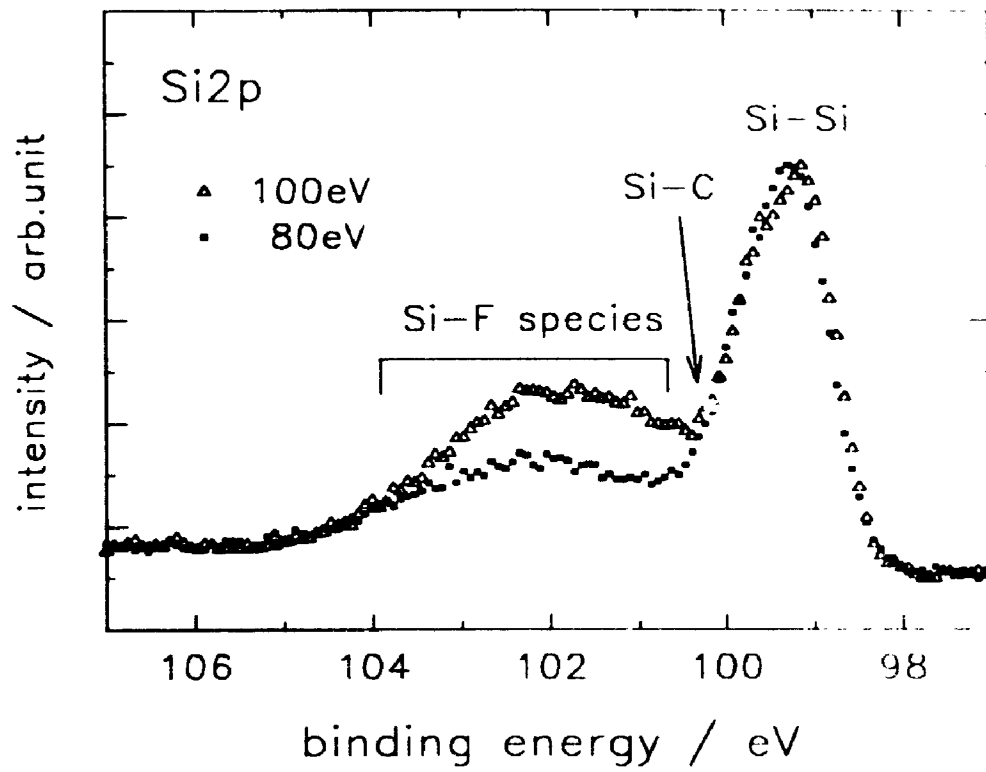
Si2p
100eV
80eV
Si-Si
Si-C
Si-F species
intensity / arb.unit
106
104
102
100
98
binding energy / eV

of C and F atoms below the Si surface to produce fluorosilyl and silicon carbide species. In the 80eV case, there was some evidence that the CF^+ ion was not dissociated or that the dissociated C and F were reacting together to form the stable fluorocarbon species (Figure 6.4), and this was not the situation at 100eV. Therefore, less C and F were available to react with the Si at 80eV CF^+ ion energy. The interaction of the molecular ion with the Si surface at these energies promotes the formation of stable, surface fluorosilyl and silicon carbide reaction products, whereas between 40eV and 60eV there was the promotion of fluorocarbon film deposition. Sputtering (both physical and physico-chemical) are also expected to become more important as the bombardment energy increases, and may thus contribute to the decrease of fluorocarbon film accumulation when the bombardment energy is above 60eV.

High resolution spectra were taken of the F1s core-level for all the samples. Figure 6.6 shows typical F1s spectra for the Si surfaces bombarded by 10eV and 100eV CF^+ ions. The 100eV ion energy is an order of magnitude greater than the previous case of 10eV, and the surface modifications resulting from such energetic molecular ion-surface interactions suggests that a simple dissociative chemisorption process is not viable/acceptable. The 10eV ion energy case produced two resolved components at 686.9eV and 688.9eV (with an area ratio of 4.5:1). The lower binding energy peak was assigned to a single fluorine-carbon bonded species while the higher binding energy component may be identified with multiple fluorines bonded to carbon, and this was consistent with the C1s spectra from Figure 6.2. For 100eV CF^+ ion bombardment, a single F1s peak was detected at 686.8eV binding energy with FWHM of 1.9eV. From the corresponding Si2p spectrum of Figure 6.5, this peak was identified as fluorine

Figure 6 6 High resolution F1s core-level spectra of Si surface after 10eV and 100eV CF^+ ion bombardment

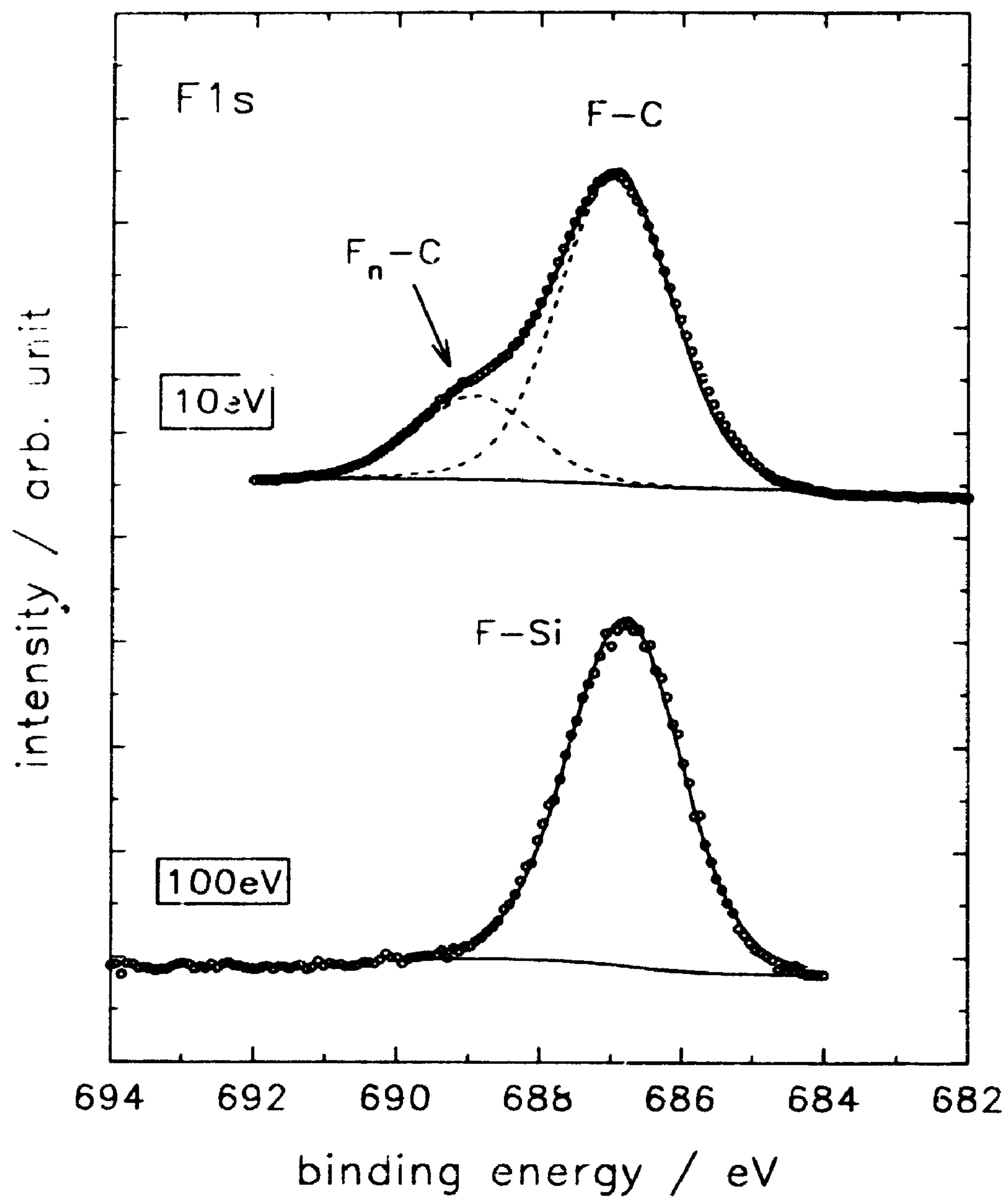
F1s
F–C
F_n–C
10eV
100eV
F–Si
intensity / arb. unit
694
692
690
688
686
684
682
binding energy / eV

bonded to silicon. The absence of any fluorocarbon species from the corresponding C1s spectrum at 100eV is also consistent with this peak assignment. The F1s core-level spectra provided complimentary information as to the identity of the various fluorine species. However, unambiguous peak assignment from the F1s signal alone was not possible due to the similar binding energies for F-C and F-Si surface species.

Figure 6.7 shows a comparison of valence band photoemission spectra for the Si surfaces exposed to different ion kinetic energies. The control surface shows three broad bands near 3eV, 7eV and 10eV binding energies. These valence bands between 0 and 15eV are comprised of the molecular orbitals of the Si3s and Si3p electrons [6.6]. Such a spectrum is indicative of crystalline Si(100) terminated by hydrogen [6.26]. After 100eV ion bombardment, the two peaks at 3eV and 7eV were completely broadened with the 3eV peak intensity reduced. This indicates the effects of both surface crystalline damage, removal of surface hydrogen, and the presence of fluorosilyl and carbide species. The valence spectra after 80eV ion exposure shows the 3eV peak having a slightly larger intensity than for the 100eV case. This could be due to a lesser degree of surface amorphization as well as less fluorosilyl and carbide concentrations. The 60eV case shows an absence of the peak at 3eV binding energy. This valence band spectrum is representative of the surface of fluorocarbon polymers [6.27,28]. At 60eV ion kinetic energy, the Si surface was covered by almost 5nm of a fluorocarbon film. Hence, the valence band spectrum was predominantly due to the film character.

At 100eV ion energy, if the individual atoms deliver kinetic energies equal to their respective mass fractions the carbon atoms will carry about 39eV while the fluorine atoms carry 61eV of energy. Related to this, Al-Bayati *et al* [6.13] recently showed that

3 OF/DE 3

PM-1 3½"x4" PHOTOGRAPHIC MICROCOPY TARGET
NBS 1010a ANSI/ISO #2 EQUIVALENT

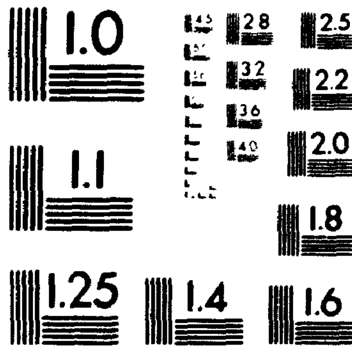

Figure 6 7 Valence band photoemission spectra for Si surfaces bombarded by 60eV, 80eV and 100eV CF^+ ions. The valence band spectrum of the wet HF/H_2O etched Si control surface represents the surface before ion beam bombardment

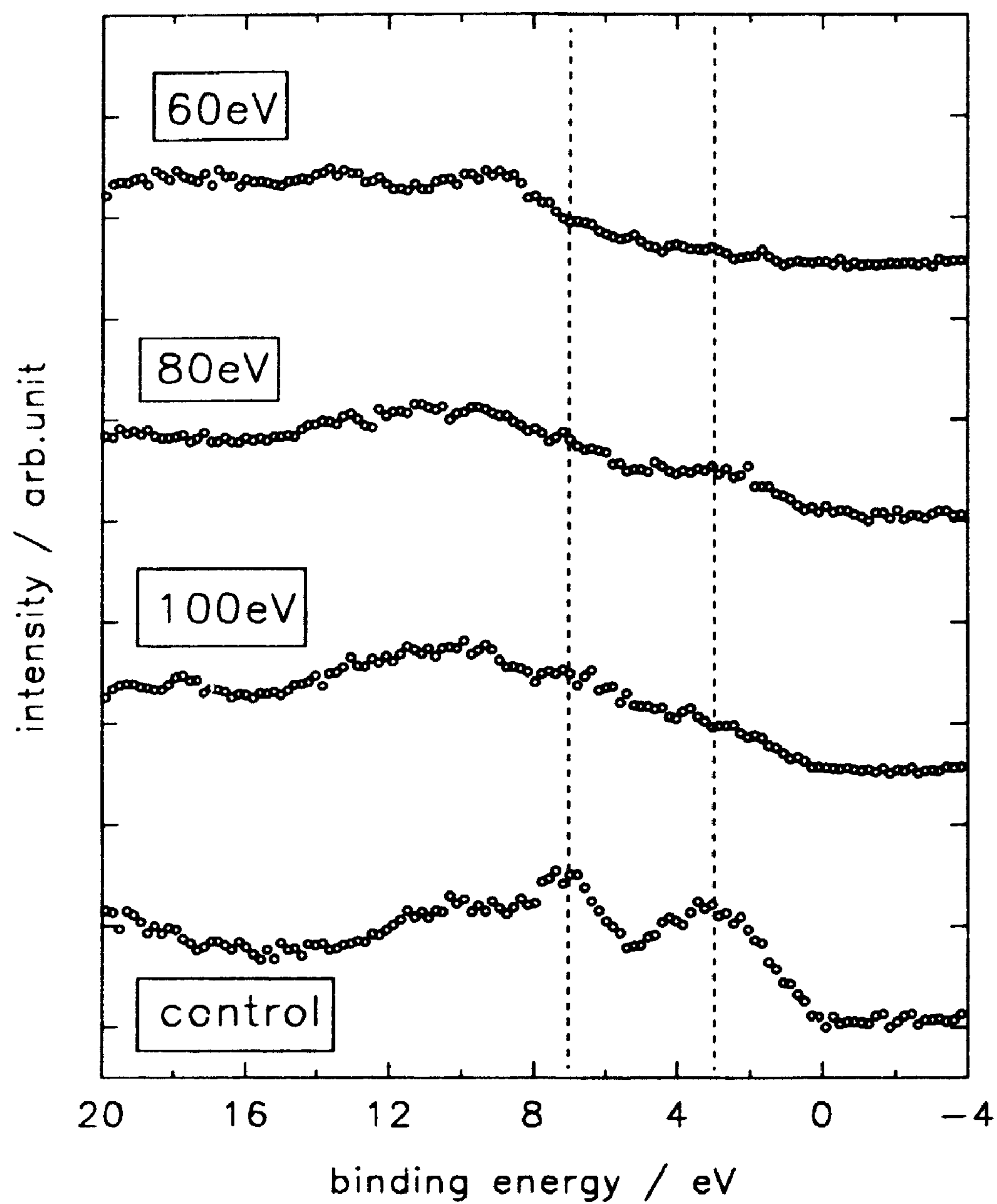
60eV
80eV
100eV
control
intensity / arb.unit
20
16
12
8
4
0
−4
binding energy / eV

argon bombardment at 60eV can cause an amorphization of silicon to a depth of about 20Å as a result of ion penetration and collision cascades. Therefore, the energies of the carbon and fluorine atoms were sufficient to cause sub-surface penetration and silicon defect formation. This work indicates that at this CF^+ bombardment energy, the initial surface reactions favour the formation of silicon carbide and a fluorosilyl layer over the development of a fluorocarbon deposition layer. Because the ion bombardment process is a non-equilibrium condition, effects such as thermal enhancement of atomic mobility and modification of reaction species growth kinetics [6.22] may have contributed to a silicon-containing reaction layer developing at the higher ion kinetic energy. These distinct reactions show that the role of the reactive ion kinetic energy is to perhaps allow different surface chemical reactions to proceed.

6.3.2 Structure of residual damage layer at 100eV

Figure 6.8 shows overlays of the C1s and Si2p spectra at two different sampling depths from angle-dependent XPS analysis for the sample exposed to 100eV CF^+ ions. At 0° polar angle (greatest sampling depth), there was a larger amount of silicon carbide seen in the C1s spectra in Figure 6.8a. From Figure 6.8b at this same angle, there was a substantial reduction in the peak intensity attributable to either fluorosilyl species or silicon carbide at this same sampling depth from the Si2p spectra. This latter figure also shows a broadening of the elemental Si peak at the shallower sampling depth corresponding to a polar angle of 63°. This broadening was likely due to the surface being amorphized from energetic ion beam bombardment. Since there was a decrease in the silicon carbide peak at 63° from the C1s spectrum, one would expect to see a

Figure 6.8 High resolution XPS spectra of Si surface after 100eV CF^+ ion bombardment with $3x10^{16}/cm^2$ showing the effects of two different photoemission polar angles of $\theta=0°$ and $\theta=63°$ on (a) C1s core-level spectra, and (b) Si2p core-level spectra.

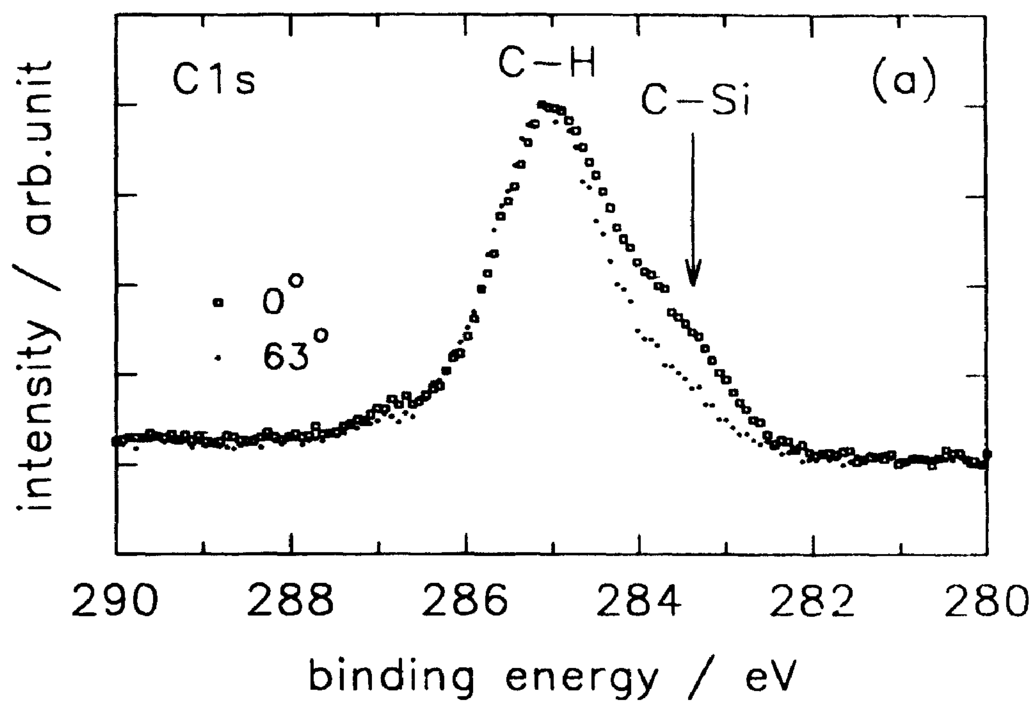
C1s
C–H
C–Si
(a)
0°
63°
intensity / arb.unit
290
288
286
284
282
280
binding energy / eV

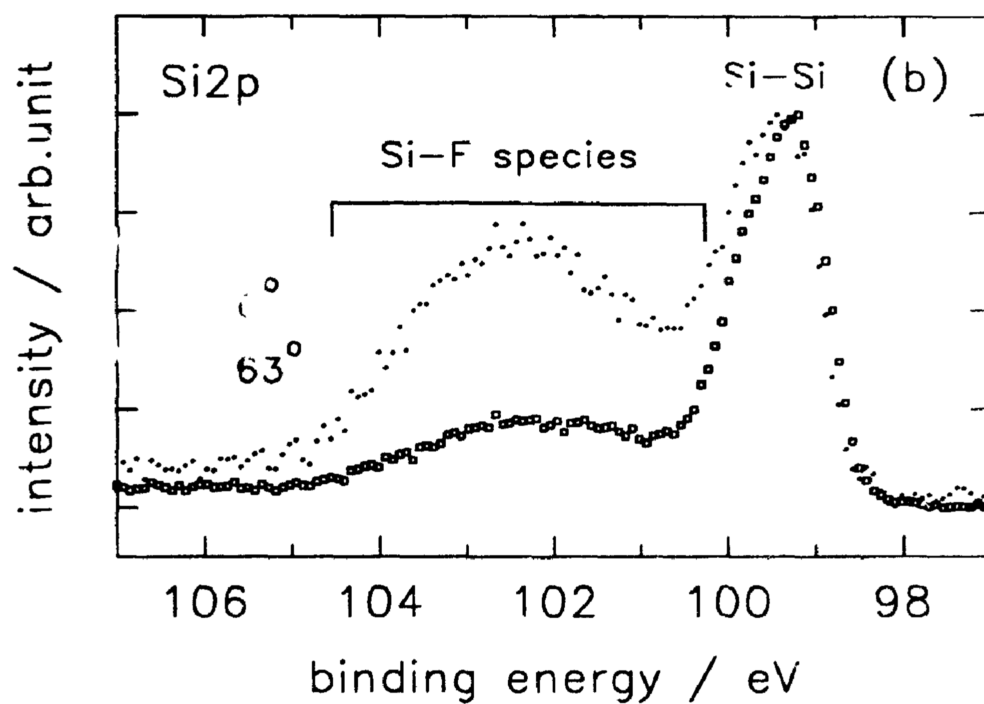
Si2p
Si–Si
(b)
Si–F species
63°
intensity / arb.unit
106
104
102
100
98
binding energy / eV

corresponding decrease in the Si2p spectrum. The observed Si2p intensity increase at 100-104 eV shows clearly that the photoemission originated from a fluorosilyl species layer, and that these species were located at the top-most surface region.

The depth distributions of the fluorosilyl species and silicon carbide are further summarized in Figure 6.9 which shows the various component areas of Si-F species from the Si2p core-level and C-Si species from the C1s core-level spectrum as a function of polar angle. In Figure 6.9, an approximate depth scale was calculated (see Chapter 3, section 3.5.4) using:

$$d = 2\lambda cos\theta$$

where d is the sampling depth in nanometres, λ is the inelastic mean free path of the photoelectrons with an estimated value of 3nm [6.29], and θ is the polar angle between the surface normal and the detector axis. The silicon carbide species showed a graded depletion towards the surface where most of the fluorosilyl species resided.

Analysis of the data in Figure 6.9 by the depth compositional profiling algorithm by Bussing and Holloway [6.30,31] is shown in Figure 6.10. The component areas due to fluorosilyl and carbide species were quantified from the elemental compositions. The IMFP was assumed to be constant at 3nm. This assumption was valid because the data manipulated by the algorithm was due only to the Si2p core-level which has its IMFP near 3nm [6.29]. The depth profiles show that there was no elemental Si in the top few nanometres of the surface. The simulated fluorosilyl and silicon carbide composition profiles suggest that the carbide layer is buried below the fluorosilyl layer. This result

Figure 6.9 Changes in percent area of C1s and Si2p core-level intensities attributed to Si-F and C-Si species as a function of photoemission polar angle, θ corresponding to Figure 6.8. Included in the Figure is the approximate sampling depth axis

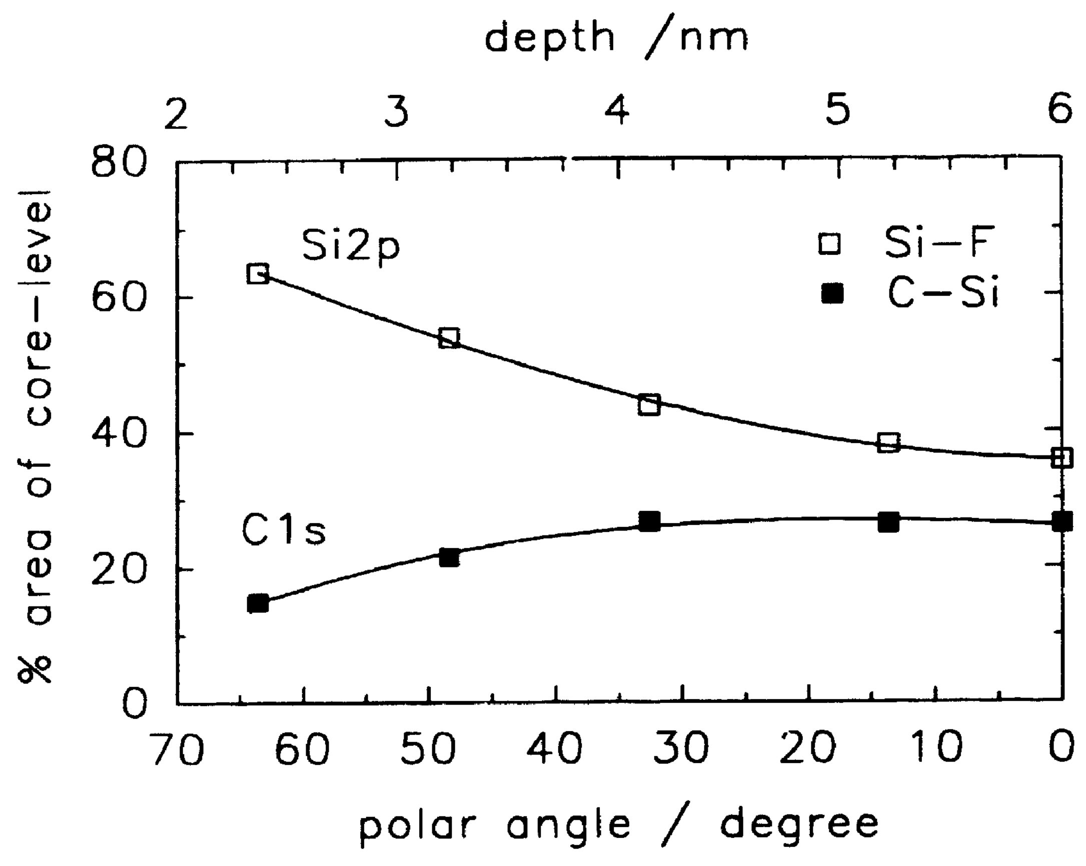
depth /nm
2
3
4
5
6
80
60
40
20
0
% area of core-level
Si2p
C1s
Si-F
C-Si
70
60
50
40
30
20
10
0
polar angle / degree

Figure 6.10 Normalized concentration depth-profile for Si-containing species calculated with the B-H algorithm using the data from Figure 6.9. IMFP was constant at 3nm.

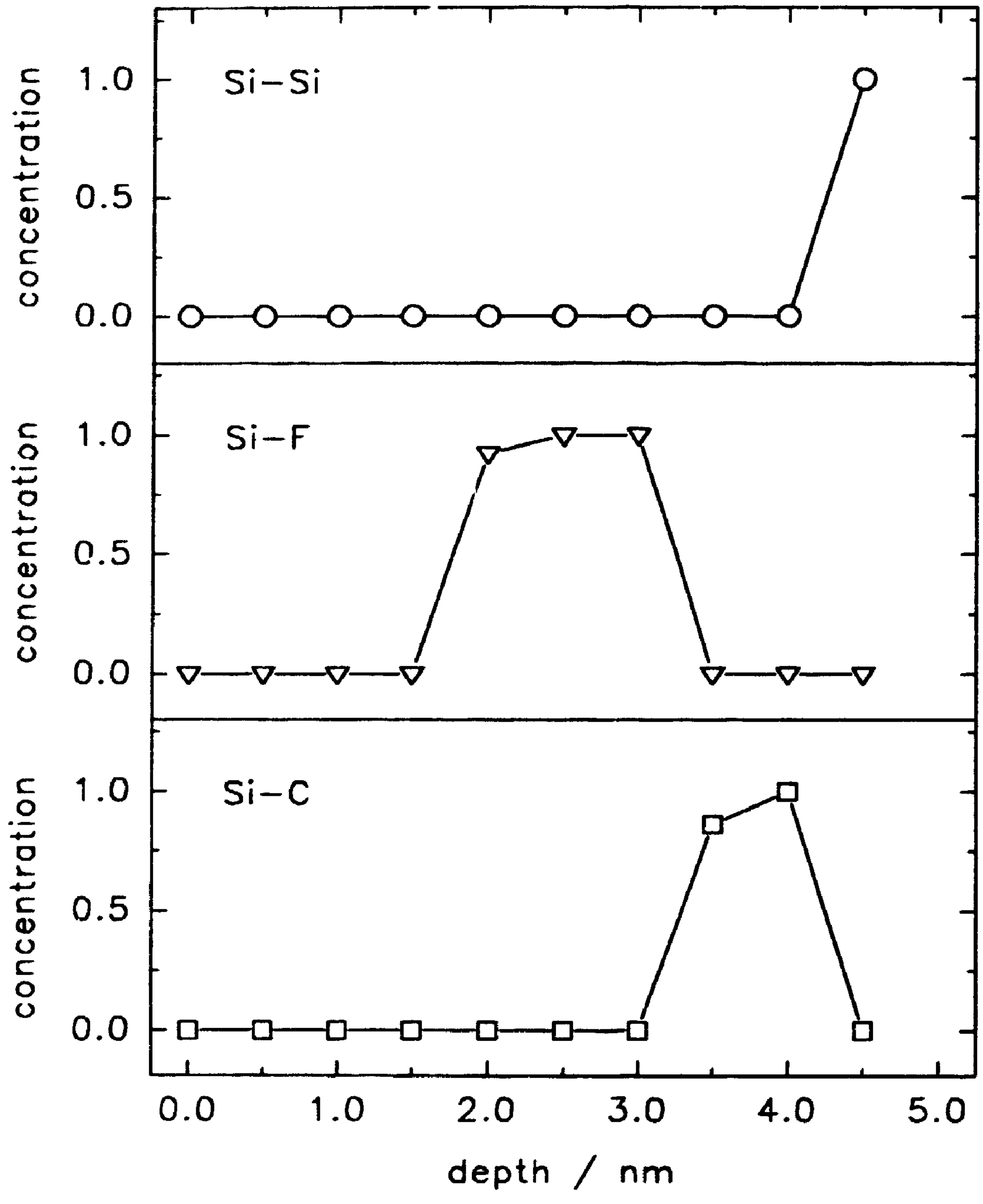
Si–Si
Si–F
Si–C
concentration
1.0
0.5
0.0
0.0
1.0
2.0
3.0
4.0
5.0
depth / nm

is supported by the photoemission intensity variation as a function of polar angle in Figure 6.9. Therefore, the fluorosilyl and carbide species exist as separate Si compound layers with Si-F species closer to the surface.

The valence band photoemission spectra taken at various photoelectron polar takeoff angle is shown in Figure 6.11. The control surface represents the Si(100) surface before ion beam bombardment at 100eV. As the polar angle was increased, corresponding to increased surface sensitive analysis, the three molecular orbital peaks at 3eV, 7eV and 10eV were seen to decrease in intensity as well as broaden into one wide band between 0eV and 14eV. Closest to the top surface, the Si lattice structure was disrupted and Si-F and Si-C compounds were formed. This accounts for the observed disappearance of the initial valence band peak components.

Assuming that when CF dissociates, the carbon atom carried 40% of the kinetic energy, TRIM (transport of ions in materials) simulations were used to estimate the penetration depths of the carbon and fluorine fragments. The calculations showed that the respective penetration depths (FWHM of the projectile distribution) for 100eV C^+ and 150eV F^+ were approximately 20 and 25Å, respectively. Hence 60eV F^+ ions should also penetrate to the same, if not larger depth in comparison to 40eV C^+ The discrepancy between the experimental distributions and the simulated distributions could be attributed to the higher diffusivity of fluorine relative to that of carbon in silicon, and to the higher volatility of fluorosilyl species relative to that of silicon carbide In support of this, previous data [6.32] on BF_2^+ implantation and annealing in silicon also showed surface segregation of fluorine. As well, the ion kinetic energies of 100 and 150eV used from the simulation were lower ion energy limits and the effects of ion channeling were not

Figure 6.11 Valence photoemission spectra of Si surface after 100eV CF^+ ion bombardment with dose of $3x10^{16}/cm^2$ at various photoemission polar angles. The control surface was the same as that described for Figure 6.7.

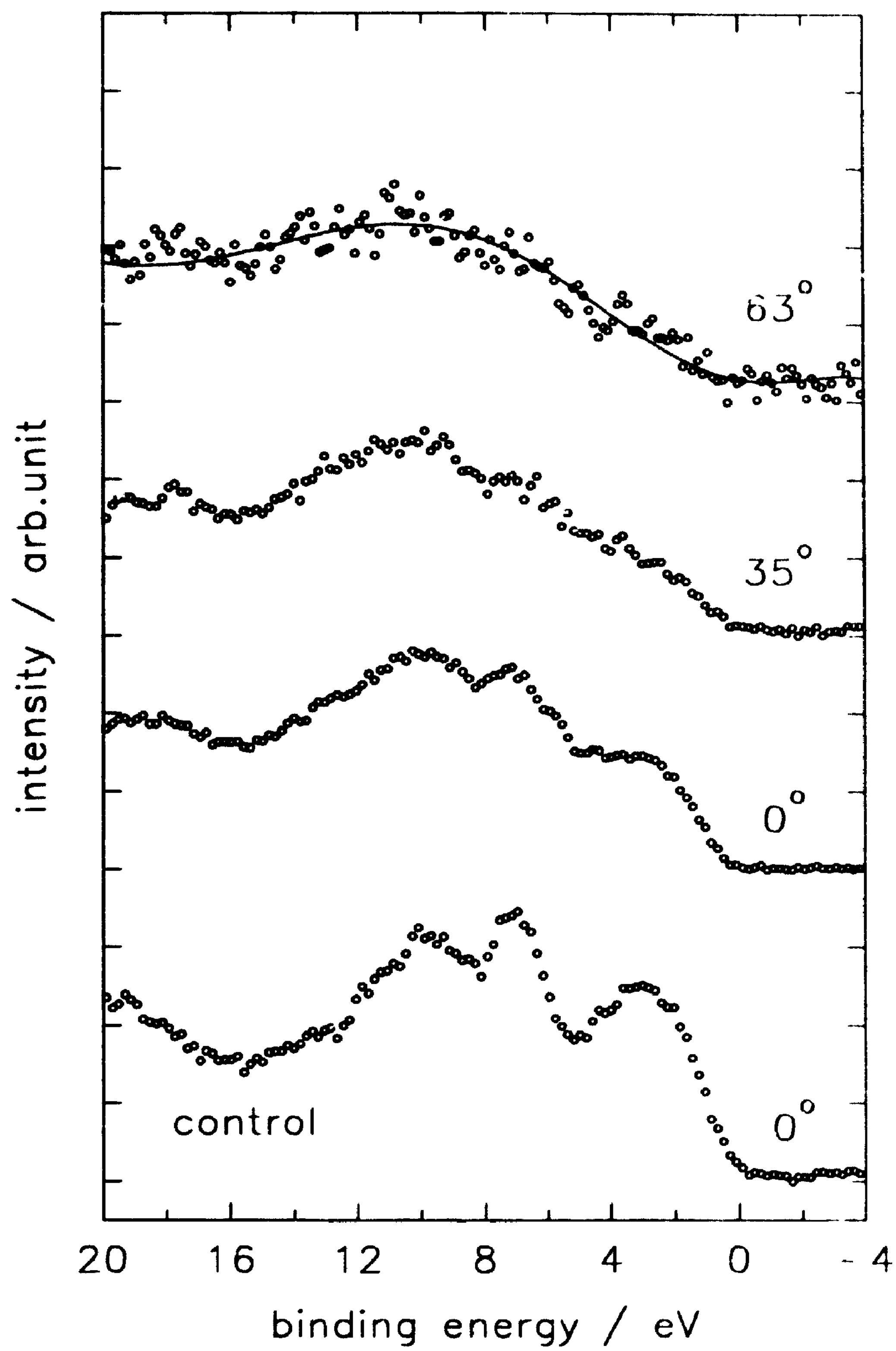

intensity / arb.unit
binding energy / eV
63°
35°
0°
0°
control
20
16
12
8
4
0
-4

considered in the TRIM code. These limitations also were likely to affect the estimated penetration depths for fluorine and carbon

6.4 Conclusions

Experimental evidence has been presented for the surface modifications of Si as a result of reactive CF^+ ion beam bombardment. Distinct surface chemical reactions were produced at ion kinetic energies of 2eV and 100eV. Below the C-F bond dissociation energy, molecular adsorption on the Si surface occurred, while just above the dissociation threshold dissociative chemisorption was observed. In the ion energy range of 10eV to 100eV, there were three regimes of surface residual damage caused by ion bombardment. In the first regime with ion energy range of 20eV to 40eV, there was a competition between molecular ion scattering and fluorocarbon film deposition on the Si surface. Between 60eV and 80eV, film deposition was suppressed while subsurface penetration by the reactive CF^+ occurred along with the development of a Si-F and Si-C reaction layer. It was considered that sputtering (both physical and physico-chemical) of the deposited fluorocarbon film became more important as the ion energy increased. At 100eV ion kinetic energy, the depth distribution of the reaction layer showed a graded enrichment of fluorosilyl species and a depletion of silicon carbide towards the very surface. Such a behaviour cannot be accounted for by TRIM simulations and indicates that the difference of atoms and chemical reactivity of the ion-surface interaction is important for the CF^+-Si system at and below 100eV.

REFERENCES

6.1 G.S. Oehrlein, R.M. Tromp, J.C. Tsang, Y.H Lee, E J Petrillo, J Electrochem Soc., 132(6), 1441, 1985.

6.2 G.S. Oehrlein, Y.H. Lee, J. Vac. Sci. Technol., A5(4), 1585, 1987

6.3 S.J. Jeng, G S. Oehrlein, Appl. Phys. Lett., 50 (26), 1912, 1987

6.4 D. Bollinger, S. Iida, O. Matsumoto, Solid State Technol., 111, 1984

6.5 Y.Y. Tu, T.J. Chuang, H.F. Winters, Phys Rev B., 23(2), 823, 1981

6.6 T.J. Chuang, H.F. Winters, J.W. Coburn, Appl Surf. Sci, 2, 514, 1978

6.7 T. Tokuyama, K.Yagi, K.Miyake, M.Tamura, N Natsuaki, S Tachi, Nucl Instr and Meth., 182/183, 241, 1981.

6.8 S. Tachi, K. Tsujimoto, S. Arai, T. Kure, J Vac. Sci Technol , A9 (3), 796, 1991.

6.9 D.C. Gray, H.H. Sawin, J.W. Butterbaugh, J. Vac Sci Technol, A9(3), 779, 1991.

6.10 M. Pichot, Vacuum, 41 (4-6), 895, 1990.

6.11 S. Tachi, S. Okudaira, J. Vac. Sci. Technol., B4(2), 459, 1986

6.12 D.G. Armour, P Bailey, G Sharples, Vacuum, 36(11), 769, 1986

6.13 A.H. Al-Bayati, K G. Orrman-Rossiter, R Badheka, D G Armour, Surf Sci, 237, 213, 1990

6.14 P.F.A Meharg, E.A Ogryzlo, I Bello, W M Lau, J Vac Sci Technol, A10(4) 1358, 1992.

6.15 L.R. Williston, I Bello, W M Lau, J. Vac. Sci Technol, A10(4), 1365, 1992

6.16 R T Sanderson, Chemical Bonds and Bond Energy, Academic Press, Second Edition, New York, 147, 1976.

6.17 H F Winters, J W. Coburn, Surf. Sci. Rep., 14, 161, 1992

6.18 C Cardinaud, A Rhounna, G Turban, B. Grolleau, J. Electrochem. Soc., 135(6), 14472, 1988

6.19 H F. Winters, D E Horne, Surf. Sci., 24, 587, 1971.

6.20 J.W Coburn, H F. Winters, T.J Chuang, J. Appl. Phys., 48 (8), 3532, 1977.

6.21 C Steinbruchel, J Vac. Sci. Technol., B 2 (1), 38, 1984.

6.22 O Vancauwenberghe, N Herbots, O.C. Hellman, J. Vac. Sci. Technol., B 9 (4), 2027, 1991.

6.23 Y Shen, W.M. Lau, J. Vac. Sci. Technol., in press.

6.24 G.J Coyle, G.S. Oehrlein, Appl. Phys. Lett., 47 (6), 604 , 1985.

6.25 B Strohmeier, Surf. Interface Anal., 15, 51, 1990.

6.26 M Niwano, Y. Takeda, K. Kurita, N. Miyamoto, J. Appl Phys., 72(6), 1992.

6.27 J Delhalle, S. Delhalle, J.M. Andre, J.J. Pireaux, J. Riga, R. Caudano, J.J. Verbist, J Electron Spectosc., 12, 293, 1977.

6.28 A Dilks, in Electron Spectroscopy: Theory, Techniques and Applications, Volume 4, edited by C.R. Brundle, A.D. Baker, Academic Press, London, 278, 1981.

6.29 S Tanuma, C J Powell, D.R Penn, Surf. Interface Anal., 17, 911, 1991.

6.30 T.D. Bussing, P.H. Holloway, J. Vac.Sci. Technol., A3(5), 1973, 1985.

6.31 B J Flinn, N S. McIntyre, Surf. Interface Anal., 15, 19, 1990

6.32 K Ohyu, T Itoga, N Natsuaki, Jpn. J. Appl. Phys., 29, 457, 1990.

CHAPTER 7.

SURFACE REACTIONS INDUCED BY Cl^+ ION BOMBARDMENT

7.1 Introduction

Low energy reactive ion bombardment has been an important technique in the dry etching of microelectronic materials [7.1]. The implementation of reactive energetic ions from glow discharges (plasma) to etch solids is critical to the development of very large scale integrated circuit (VLSI) fabrication [7.2]. The neutrals, radicals and ions from the reactive plasma impinge on the surface of the material to be etched. This interaction results in the formation of gas phase volatile species containing elements of the material being dry etched. In this way, the erosion of material is accomplished. The energetic ion bombardment provides the preferential etching of material in a specific direction, i.e. anisotropic etching. This ion bombardment effect enhances the etch yield of material over the case of no ion bombardment [7.3,4]. However, the ion bombardment process usually produces some degree of residual surface damage in the form of surface crystalline disorder and incorporation of contaminant species.

Pogge et al [7.5] studied the dry etching of silicon (Si) and silicon dioxide (SiO_2) using molecular chlorine (Cl_2) and argon (Ar) gas mixtures in a commercial reactive ion etching (RIE) system as an alternative to fluorocarbon plasma RIE. The etching characteristics of Si as function of processing parameters were found and an etch rate

ratio of 20:1 for Si:SiO_2 was achieved. This work shows the feasibility of Cl RIE as an alternative to fluorocarbon RIE of Si. Cl-based plasma etching of Si yields anisotropic etching because of a low spontaneous Cl-Si reaction rate and sidewall passivation [7.6-7]. A CCl_2F_2 plasma is used to conventionally etch Si with the etchant assumed to be atomic Cl [7.8]. RIE of Si with this plasma results in a modified Si surface reaction layer [7.9]. X-ray photoelectron spectroscopy (XPS) analysis of the Si surface after etching indicates a chlorosilyl compound ($SiCl_n$, n=1,2,3,4) layer [7.9]. The presence of fluorine (F) in the plasma makes interpretation of this chlorosilyl reaction layer ambiguous since fluorosilyl species will also form [7.10]. Fundamental studies of Cl etching of Si have utilized Ar^+ ion bombardment in the presence of a Cl_2 gas flux [7.11-14]. Such studies have been primarily interested in the elucidation of etching mechanisms and identification of gas phase etch products with limited surface analysis studies. Hence, the need to study the residual damage and modifications induced by the Cl^+ ion bombardment of Si is of both fundamental scientific and technological importance in the development of Cl-based RIE.

Cl^+ ion bombardment between 20 and 65eV kinetic energies has also been adopted as a surface cleaning technique for Si prior to epitaxial growth of Si and germanium (Ge) under vacuum conditions [7.15,16]. It was proposed that Cl^+ ion impingement at these low energies neither physically sputter the target nor introduce any significant crystalline damage, but instead removed surface impurities and contaminants by forming gas phase volatile complexes. Such a hypothesis has not been investigated in detail. It was shown [7.15,16] that homoepitaxy of Si for substrates cleaned by 20 and 40eV Cl^+ ions with a dose near 10^{17}ions/cm^2 at 600°C resulted in the formation of dislocation loops below the interface. This implies that radiation damage cannot be completely ruled out at this low

ion energy regime. Related to the above work, Armour and coworkers have studied the detailed surface residual damage on Si caused by Ar^+ and Cl^+ ions at 110eV [7.17] and at 300eV [7.18]. Because of the chemical effects associated with Cl^+ bombardment, it is conceivable that ion etching with this halogen species can provide some advantages over Ar^+ ion sputter-cleaning. However, any Si surface previously exposed to air ambient or subjected to a wet HF treatment will attract some oxygen (O) surface contamination. Hence, the initial stages of any subsequent surface cleaning procedure must also remove these contaminants. It is thus relevant to study the role of Cl^+ bombardment on such oxygen removal. Accordingly, the surface residual contamination and damage in Cl^+ bombardment of Si needs to be understood before acceptance of such an ion cleaning procedure.

The aim of this chapter was to characterize the residual surface damage and contamination of the p-type Si(100) surface induced by Cl^+ ion bombardment in the energy range of 1-100eV. The ion kinetic energy range of interest was chosen based upon a comparison with Cl-based plasma RIE and surface cleaning of Si. The effects of Cl surface incorporation and surface band-bending on ion fluence was also investigated within the above energy range. The ion dose range investigated was $10^{15}/cm^2$ to $10^{18}/cm^2$.

The effects of Cl^+ ion bombardment of Si(100) was studied using a mass-separated ion beam of $^{35}Cl^+$ ions. This ensured that a pure Cl^+ beam of species was impinging on the Si surface. The ion beam was directed at normal incidence to the Si surface because this is the conventional direction found in dry etching/cleaning. XPS was the surface analysis technique of choice because it provides information on surface concentrations (quantitation) and the different chemical states of surface constituents.

7.2 Experimental procedure

The Si(100) samples were boron implanted at 16keV with a dose of $1.6x10^{15}$ /cm^2 followed by rapid thermal annealling at 1050°C for 30s to electrically activate the dopant. The samples were wet etched in a dilute aqueous hydrofluoric acid (HF) solution for 30-45s and blown dry with nitrogen gas to remove the passivating oxide. The samples were then immediately loaded into the LEIB system for reactive Cl^+ ion bombardment.

$^{35}Cl^+$ ions were extracted from a CCl_2F_2 plasma confined within a hot dc filament Colutron ion source. The LEIB system is described in Chapter 3. The ion beam impinged at normal incidence to the Si(100) surface for a range of ion kinetic energies between 1-100eV and a range of ion doses from $1x10^{14}$ to $1.5x10^{18}$/cm^2. All ion bombardment experiments were conducted at room temperature. Once samples were exposed to the ions, the specimens were transferred under vacuum ($P<1x10^{-6}$Torr) to an XPS system for surface analysis.

The XPS spectrometer was a SSX-100 small X-ray spot system (see Chapter 3). Spectra were collected at pass energies of 100eV for quantitation and 20eV for high resolution. The X-ray spot size at the sample surface was approximately 300μm in diameter. All spectra were acquired at a constant polar photoemission angle of 55° with respect to the sample normal. Surface atomic concentrations were calculated (see Chapter 3) and binding energy positions were determined using an iterative chi-squared minimization peak-fitting program with a Gaussian-Lorentzian profile. All peak positions

were referenced to the $Au4f_{7/2}$ core-level peak position at 83.93eV from an Ar^+ sputter-cleaned gold foil always present under UHV conditions.

7.3 Results and discussion

7.3.1 Surface oxidation induced by 1eV bombardment

Figure 7.1a shows the Cl2p spectrum of the Si(100) surface bombarded with 1eV Cl^+ to $3x10^{16}/cm^2$. Two chemical components were clearly resolved with the binding energies of the $Cl2p_{3/2}$ component at 199.4 and 200.8eV. These two components were attributed to Cl-Si and Cl-O-Si species, respectively. The justification for such assignments will be discussed below.

After each ion bombardment experiment, XPS was carried out both in the bombarded area and outside that area for comparison purposes. Figure 7.1b shows the Si2p spectra of the non-bombarded area overlaid with that taken in the area receiving $3x10^{16}/cm^2$ at a bombardment energy of 1eV. At this low bombardment energy, atom displacement induced by the collisional cascade was negligible. The reactive Cl^+ exposure of the surface however, clearly induced some photoemission intensity at about 104 eV which was absent in the spectrum of the non-bombarded area. When this peak was curve-fitted with one chemical component, the $Si2p_{3/2}$ level binding energy was 103.5 eV. This value is characteristic of SiO_2 [7.19].

The main peaks of the two spectra in the binding energy range 99-100 eV showed

Figure 7 1 High resolution XPS spectra of (a) Cl2p and, (b) Si2p core-levels for Si surface receiving 1eV Cl^+ ion bombardment with a dose of $3x10^{16}$ ions/cm^2. The control surface was for the same sample wet etched in aqueous HF solution before ion beam exposure.

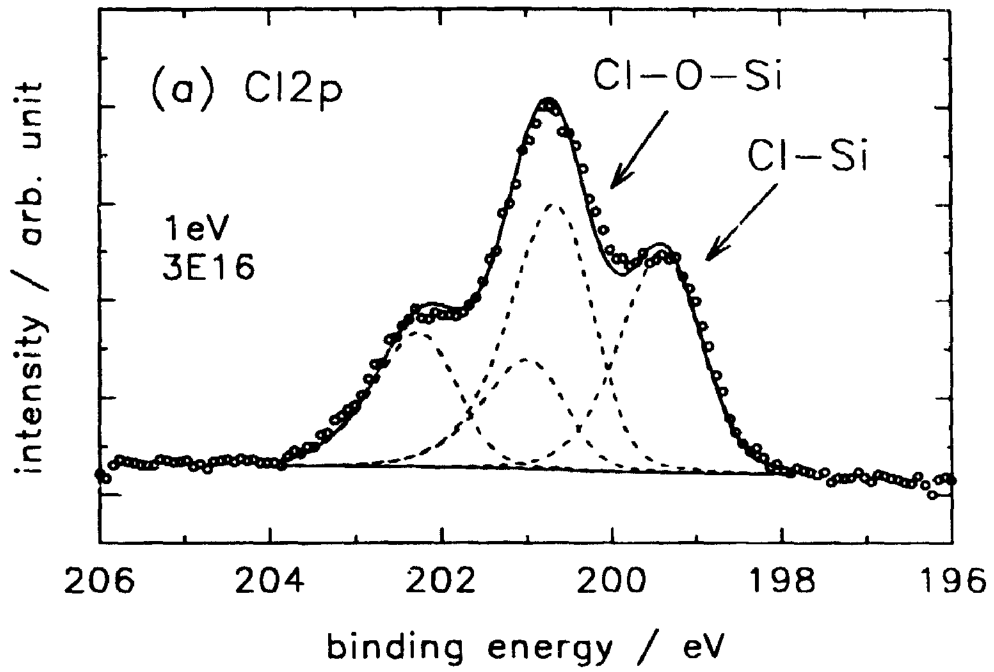
(a) Cl2p
Cl–O–Si
Cl–Si
1eV
3E16
intensity / arb. unit
206
204
202
200
198
196
binding energy / eV

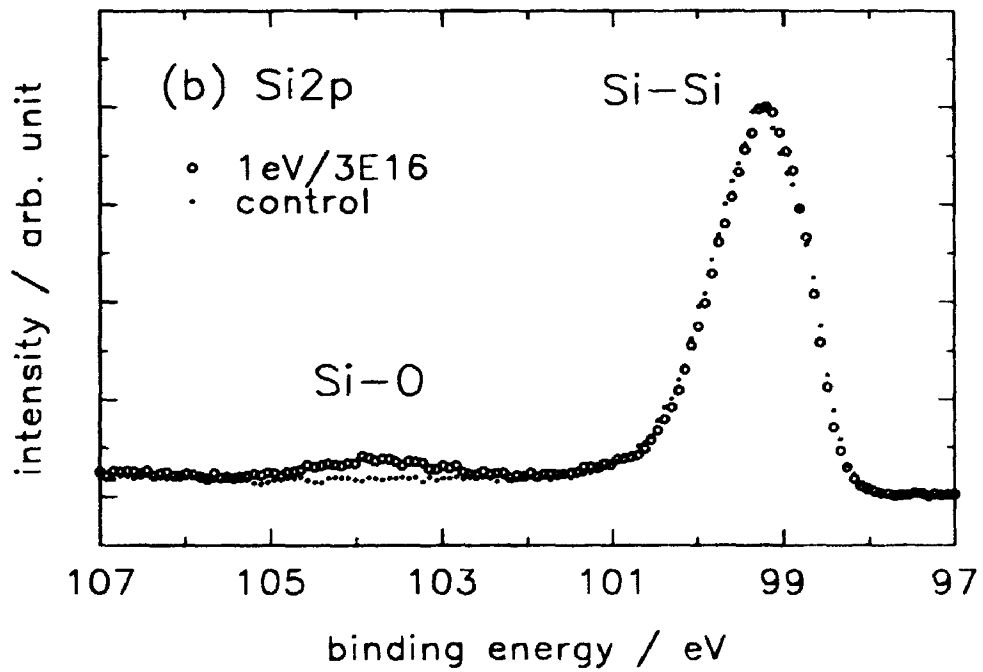
(b) Si2p
Si–Si
1eV/3E16
control
Si–O
intensity / arb. unit
107
105
103
101
99
97
binding energy / eV

no differences caused by the exposure to 1eV Cl^+ ions. The curve-fitting of the peak shape required a minimum set of three pairs of spin-orbit split components. The $Si2p_{3/2}$ binding energies were 99.0, 99.4, and 100.2eV. This first component was attributed to the bulk-like silicon. Our database of $Si2p_{3/2}$ spectra shows the bulk-like silicon with its Fermi level at the valence band maximum (VBM) has a binding energy of 98.7eV [7.20]. Hence, the surface Fermi level of the sample was at 0.3 ± 0.1 eV from VBM. Although the samples were heavily doped with boron and the Fermi level position was expected to be close to the VBM, some of the dopant was deactivated by hydrogen during the wet HF-etch surface treatment [7.21] procedure before ion bombardment. Therefore, the present XPS investigation confirms this hydrogen passivation effect and also shows that low energy Cl^+ ion bombardment at 1eV did not significantly induce a surface band bending condition of the Si.

The $Si2p_{3/2}$ chemical component towards a higher binding energy of 0.4eV from the bulk-like peak has previously been assigned to silicon bonded with hydrogen [7.22]. Since the silicon of SiO_2 is in its +4 oxidation state and shows a chemical shift of 4.5 eV, every unit increment of oxidation number thus roughly contributes a chemical shift of about 1.1eV. On the surface receiving no ion bombardment, it is plausible that some of the intensity of the component shifted by 1.2eV is contributed from Si-OH bonds or Si atoms associated with adsorbed water. Such an assignment was also consistent with the observation of photoemission in the O1s region, photoemission which amounted to less than one monolayer equivalent of oxygen atoms. The absence of any additional photoemission in the binding energy range of 101 to 105eV from this unbombarded surface suggests that silicon atoms having an oxidation number higher than one were rare.

On the ion bombarded surface, the chemistry is more complicated because Si-Cl on a silicon surface is known to give a chemical shift of 0.9eV [7.23] Hence, its presence is also plausible, which is confirmed by the analysis of the Cl2p core-level However, the absence of any addition photoemission in the binding energy range 101-103 eV indicates [7.23] that the amounts of $SiCl_2$ (chemical shift 1.7eV) and $SiCl_3$ (chemical shift 2.7eV) were below the XPS instrumental detection limit. Since the observed $Si2p_{1/2}$ chemical shift of 4.5 eV was far greater than that of any silicon chlorides and since the surface contaminants were mainly chlorine and oxygen, the photoemission with this chemical shift was attributed within reason to Si atoms with Si-O bonds and an oxidation state number of +4.

The results above suggest that before bombardment, the residual surface oxygen was present in the form of $Si(-OH)_n$ with n=1 or adsorbed water, and that the bombardment aggregated these residual O atoms into oxygenated species of $Si(-O-X)_4$ with X = Cl or Si. The proposed Si-O-Si network is required to hold the highly oxidized species on the surface. The reaction mechanism for the formation of this highly oxidized species can be partitioned as follows: (a) neutralization of the chlorine ion by the silicon valence electrons; (b) formation of Si-Cl bonds; (c) replacement of the Si-Cl bond with an Si-O-Cl bond. The bond replacement is thermodynamically favorable and has been previously discussed and shown experimentally [7.13]. With the assumption that the $Si(-O-X)_4$ species formed a uniform overlayer, the thickness of this layer was estimated to be about 0.3nm (assuming the oxide intensity is 10% and the main peak is 90%, and the inelastic mean free path in the oxide is 3.0nm [7.24]) Further Cl^+ bombardment at 1eV did not induce any significant changes of the spectral data, probably because the

transformation of surface oxygen to Si-(O-X)$_4$ was completed and because the etch yield of the surface "oxide" by atomic chlorine is very small [7.25] and the sputtering yield at 1eV was negligible.

7.3.2 Effect of ion kinetic energy

Although the surface oxide (referring to the Si-(O-X)$_4$ species) induced by Cl^+ bombardment was not effectively removed by further Cl^+ bombardment at 1eV, the oxide removal was observed at higher bombardment energies and for greater doses (see section 7.3.3). Figure 7.2a shows the Cl2p and Si2p spectra after bombardment by 20eV Cl^+ ion at the same dose of $3x10^{16}/cm^2$. In comparison to the bombardment at 1eV, this higher ion energy resulted in a lesser amount of Cl-O-Si species, surface oxide and suboxides (referring to Si-(O-X)$_n$ with n<4). These surface composition changes can be attributed to the increase in ion kinetic energy.

Analyses of the Cl2p spectra showed that the samples bombarded at 1eV and at 20eV both had Cl-Si and Cl-O-Si species on their surfaces. The Cl-O-Si component was reduced in intensity on the sample receiving 20eV Cl^+ ions. This indicates a greater probability of removing such species at the higher ion kinetic energy. At a bombardment energy of 20eV, the Si-O physical sputter yield due to Cl^+ is expected to be larger than at 1eV simply because of the increased kinetic energy. This system of Cl^+ physical bombardment of Si can be compared to the Ar^+/Si case because of similar masses, e.g. Ar has an atomic weight of 39.9 and Cl has an atomic weight of 35.4. At a bombardment energy of 20eV, the Cl^+/SiO_2 sputter yield is expected to be much smaller than for Ar^+ bombardment at 50eV which is approximately 0.02 [7.26]. The lesser amount of Cl-O-Si

Figure 7.2 High resolution XPS spectra of (a) Cl2p and, (b) Si2p core-levels for Si surface receiving 20eV Cl^+ ion bombardment with a dose of $3x10^{16}$ions/cm^2. The control surface was for the same sample wet etched in aqueous HF solution before ion beam exposure

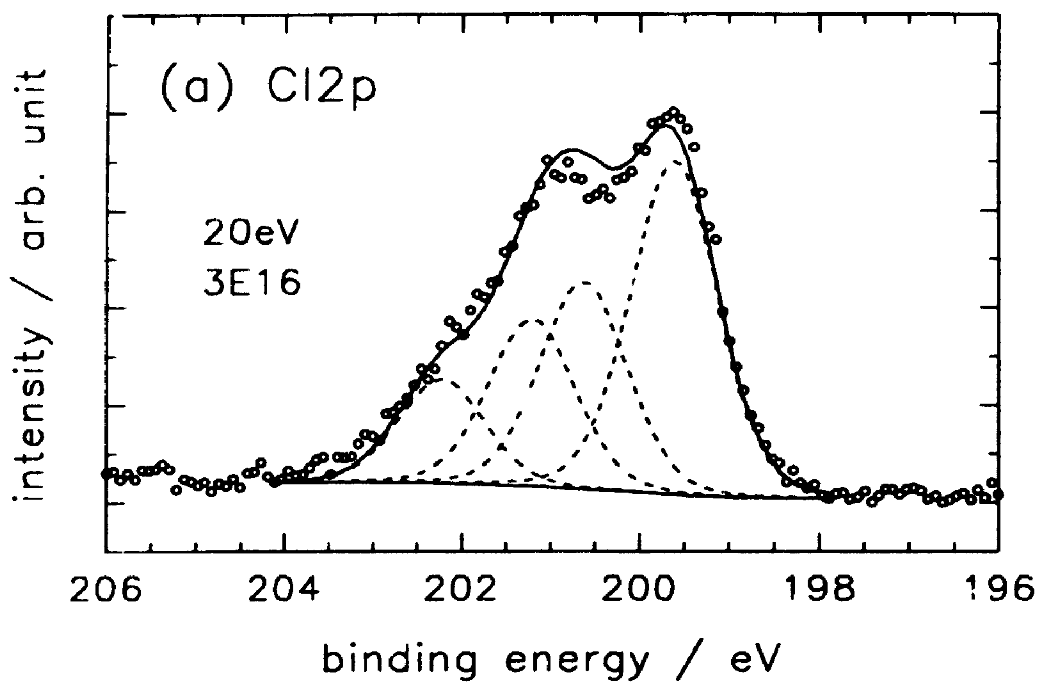
(a) Cl2p
20eV
3E16
intensity / arb. unit
206
204
202
200
198
196
binding energy / eV

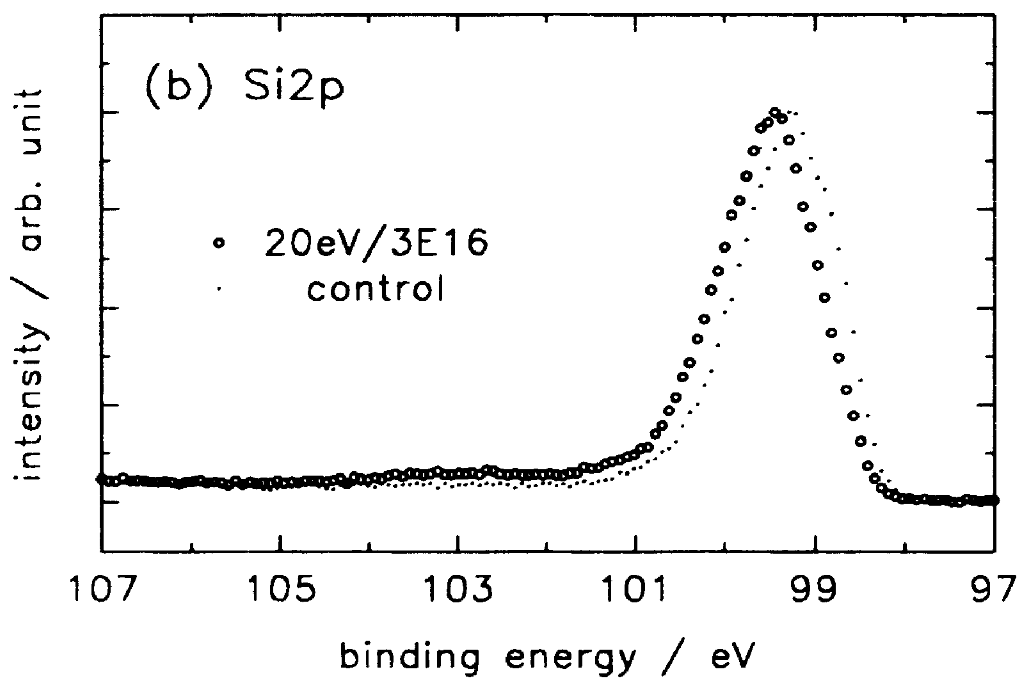
(b) Si2p
20eV/3E16
control
intensity / arb. unit
107
105
103
101
99
97
binding energy / eV

surface species at 20eV Cl^+ bombardment may therefore be the result of more efficient physical sputtering.

Figure 7.2b shows the presence of a low intensity component towards higher binding energy from the dominant peak near 99eV binding energy The importance of cascade collisions for Ar^+ bombardment of Si at this low energy has also been shown recently [7.27]. The presence of very low level suboxides in Figure 7 2b also indicates that even at this low energy, atom mixing due to the collisional cascade already becomes an important factor in determining the surface reaction products.

The Si2p core-level spectra of Figure 7.2b also show the main peak position for the 20eV ion bombarded surface at a slightly higher binding energy compared to the surface not receiving energetic Cl^+ ion exposure. The Cl2p spectrum in Figure 7 2a behaved in a similar manner with the Cl-Si species identified from the $Cl2p_{3/2}$ binding energy position at 199.5eV. This binding energy was approximately 0 2eV higher than the corresponding spectrum for Cl^+ bombardment at 1eV. The differences in these core-level spectra were due to the downward band-bending of the Si surface bombarded by Cl^+ at 20eV. This surface band-bending phenomena will be discussed in section 7 3 3

For Si(100) surfaces receiving 100eV Cl^+ reactive ions with the same dose of $3x10^{16}/cm^2$ as for the 1 and 20eV cases, there was even less Cl-O-Si species present from the Cl2p spectrum At this incident ion energy, the surface sputtering of the oxygenated species was greatest for the range of 2-100eV The physical sputter yield of SiO_2 by Ar^+ at 100eV is about 0.03 [7.13]. Hence, it is not too surprising that Cl^+ bombardment at 100eV was sufficient to remove the submonolayer of surface oxygenated species layer formed at the initial stages of bombardment.

The Si2p spectrum for the sample bombarded at 100eV was similar to that from Figure 7 2b The relative shift in binding energy between regions exposed to ion bombardment and an unexposed region was approximately 0.4eV which was greater than at 20eV ion beam exposure Physical bombardment effects can be explained by comparing the Cl^+ bombardment to Ar^+ ion bombardment. The Si lattice is known to be damaged by Ar^+ ion bombardment in this energy range [7.28]. The surface damage produces electrically active defect states within the semiconductor bandgap. If electrically active surface defects are present as donor states within the semiconductor bandgap of the p-type Si [7 29], then the effective doping concentration may be reduced causing the semiconductor Fermi level to shift away from the valence band maximum. This is manifested as surface band bending [7.30,31]. Such band-bending is seen as a shift in the core-level spectrum [7.30,31] which is distinct from the conventional chemical shift effect [7 19] Such damage was expected from Cl^+ ion bombardment, and the spectral shifts in binding energy support this premise (see also the discussion of Figure 7.8 in the next section)

Although the surface roughness of samples bombarded by 100eV Cl^+ for the removal of residual surface oxygen will be negligible because the dose required is low, a drawback was observed for bombardment at this high energy. As mentioned earlier, the relative shifting of the Si2p peaks in Figure 7.2b indicates that Cl^+ bombardment at 20-100 eV induced a surface band-bending on the p-type Si. The increase of the band bending with an increasing energy suggests that the observed band bending was due to the incorporation of chlorine into the silicon subsurface. For the samples bombarded with Cl^+ at 100 eV, a type-inversion was evident (i.e. the p-type Si surface was converted to

n-type). It has been shown recently that Ar^+ bombardment merges the surface Fermi levels of n-type and p-type Si to the midgap [7.21]. Hence, the type-inversion induced by Cl^+ bombardment is definitely not due to simple radiation induced defects in silicon, but instead, was likely caused by chlorine incorporation

Figure 7.3 shows a plot of [Cl/Si] surface composition ratio as a function of Cl^+ ion kinetic energy for a constant ion dose of $3x10^{16}/cm^2$ The amount of surface Cl relative to the silicon was found to increase from 20 to 40eV and then decrease from 40 to 100eVas a result of Cl^+ bombardment. This halogen ion kinetic energy effect on surface chlorination of silicon was slightly different than for the case of F^+ ion bombardment over the same energy and fixed dose (see Figure 5 4 in Chapter 5)

The reduction of surface chlorine with increasing ion energy between 40 to 100eV was considered to be caused by greater ion penetration and sputtering The physical penetration depth is predicted to be greater for the higher incident ion kinetic energies Because XPS is a surface sensitive technique, the quantification of the amount of surface Cl distributed at greater depths at 100eV compared with the lower energy of 40eV would underestimate the actual amount. This would then give a lower amount of surface chlorine at the higher energies. Also, the physical sputtering of Si by Cl^+ will be greater towards the higher energies, and this would contribute to a reduction in the amount of implanted chlorine (i.e. chlorine self-sputtering).

As well, since the Cl-O-Si species concentration was greater at lower energy, this indicates that the surface contamination of O was less easily removed at lower energy, and this behaviour was supported by the detection of Cl-O-Si species from Figure 7 1a and 7.2a. The abundance of these species at lower energies may be due to less energetic

Figure 7 3 XPS surface composition ratio of Cl/Si (at a polar photoemission angle of 55° with respect to the sample surface normal) as a function Cl^+ ion kinetic energy.

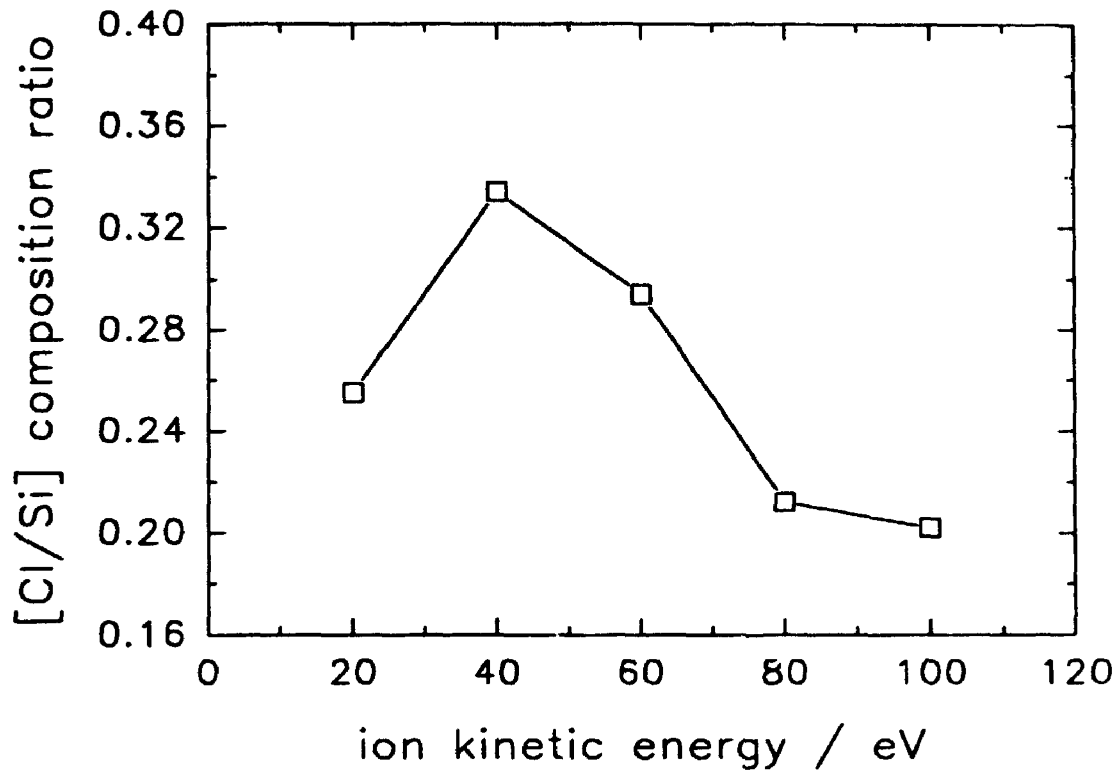
[Cl/Si] composition ratio
0.40
0.36
0.32
0.28
0.24
0.20
0.16
0
20
40
60
80
100
120
ion kinetic energy / eV

collisional cascade-induced desorption of such species. The lower energy Cl^+ ions may also react with the O to give stable surface oxygen species such as Si-(O-X)$_4$ (see section 7.3 1), whereas at 100eV, these species were removed by physical sputtering. In addition, the chemical reactivity of Cl with the surface oxides is low [7.11,25], hence there was not likely to be any significant chemical enhancement of the sputtering yield in the low energy ion bombardment.

The observed decrease in [Cl/Si] surface composition ratio from 40eV to 20eV (Figure 7 3) was not seen for the F^+ ion bombarded Si(100) system (see Chapter 5). The difference in these two systems is due to the fact that the spontaneous reaction probability of F with Si is much greater than Cl with Si [7.11]. When F atoms arrive on the Si surface, it reacts readily with the silicon. Hence, prior to the formation of the final etching products which will be desorbed, the F sticking probability is near unity. In comparison, the Cl sticking probability is very small. In other words, when chlorine atoms possessing near thermal energies arrive on the Si surface, they will more than likely leave the surface. Therefore, for Cl^+ bombardment, the chlorine surface incorporation probability is expected to drop when the incident ion energy approaches zero. These results emphasize the importance of the chemical reactivity and kinetic energy of the incident reactive ion species in producing residual surface Si damage.

7.3 3 Effect of ion fluence at 100eV and 40eV

Figure 7.4 illustrates the effects of ion dose or fluence at two different ion kinetic energies The ion kinetic energies of 100eV and 40eV were chosen based upon the Cl

Figure 7.4 XPS surface composition ratio of Cl/Si (at a photoemission polar angle of 55° with respect to the sample surface normal) as a function Cl^+ ion dose at (a) K.E.=100eV, and (b) K.E.=40eV

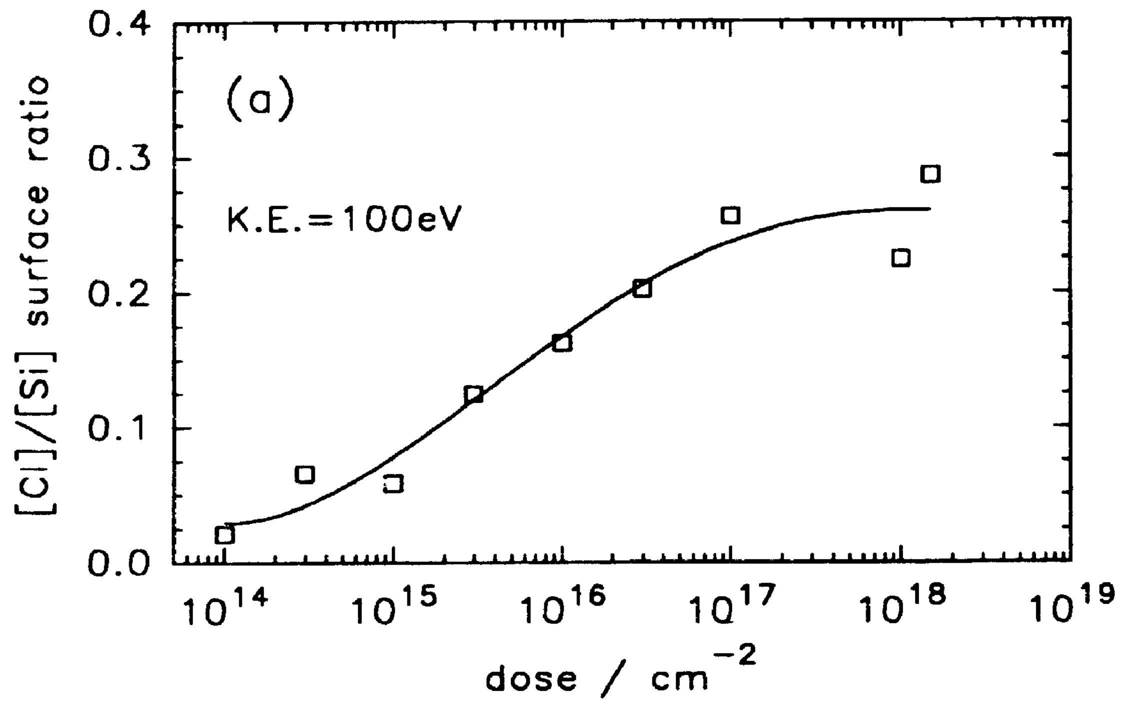
0.4
0.3
0.2
0.1
0.0
(a)
K.E.=100eV
[Cl]/[Si] surface ratio
10^{14}
10^{15}
10^{16}
10^{17}
10^{18}
10^{19}
dose / cm^{-2}

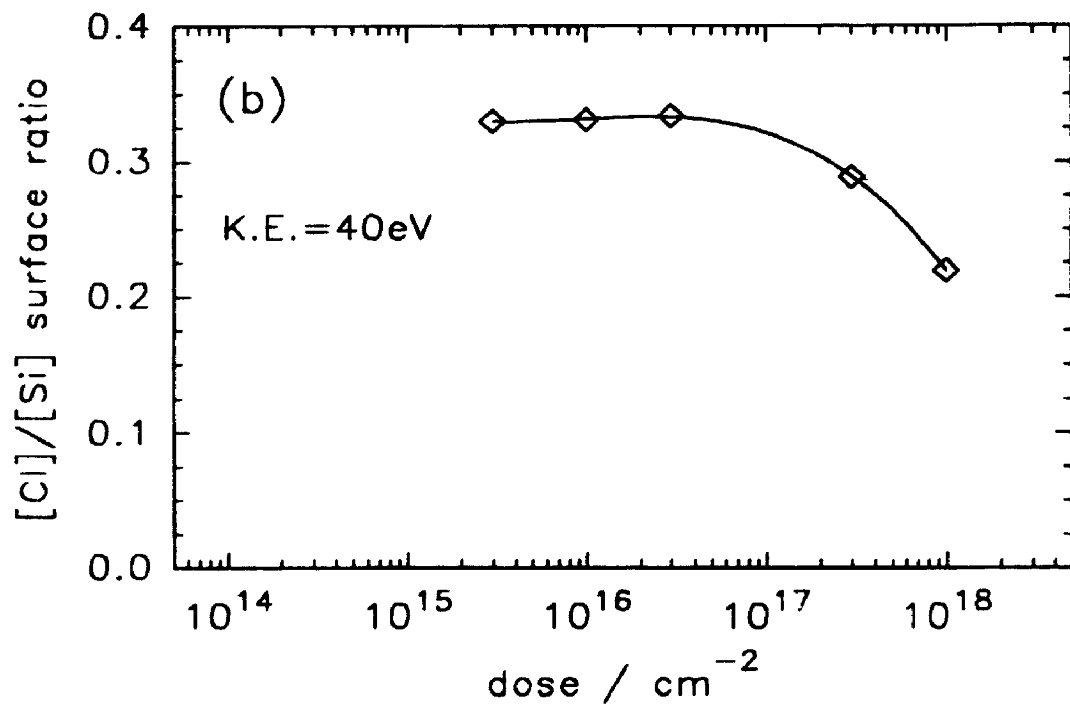
0.4
0.3
0.2
0.1
0.0
(b)
K.E.=40eV
[Cl]/[Si] surface ratio
10^{14}
10^{15}
10^{16}
10^{17}
10^{18}
dose / cm^{-2}

incorporation trend from Figure 7.3. The behaviour of Cl surface incorporation at 100eV (Figure 7.4a) was markedly different than at 40eV. At 100eV Cl^+ ion bombardment, the amount of surface chlorine gradually approached a saturation level towards higher doses, while the 40eV bombardment case showed larger amounts of surface Cl at lower doses. These results imply that the surface reactions induced at these two different ion kinetic energies over the same dose range may be different.

The gradual increase of surface Cl with ion dose at 100eV (Figure 7.4a) is similar to the Ar^+/Si system at the same ion kinetic energy [7.27] in which the Ar incorporation probability initially was small at low fluences and increased at higher doses and finally achieved a steady-state surface concentration. In comparison to Ar, Cl has a higher chemical reactivity with Si which would then result in a greater degree of Cl incorporation over Ar incorporation into the silicon.

The amorphization of the Si(100) surface by Ar^+ in the ion kinetic range of 60-510eV has been shown to increase with increasing ion dose up to $1x10^{16}/cm^2$ [7.28]. The mechanism of increasing surface damage with greater dose is attributed to the migration and accumulation of defects generated from the ion bombardment. These defects accumulate at the amorphous/crystalline interface, i.e. layer-by-layer amorphization mechanism. In addition, the effects of residual physical damage to Si(100) has been studied for Ar^+ and Cl^+ ion bombardment at 110eV [7.17] and shows that the depth of damage was similar. Hence it is reasonable to assume that a similar disordering of the crystalline silicon surface with increasing Cl^+ ion dose at 100eV was occurring. This observed increase in surface chlorine with dose at 100eV bombardment is then considered to be attributed to processes such as greater physical damage and implantation into the

silicon

Figure 7.4b shows the effect of ion dose on surface Cl incorporation into Si for 40eV ion bombardment. The surface [Cl/Si] ratio was higher than for the 100eV case at a fluence of $3x10^{15}/cm^2$ and showed less variation towards higher doses compared to Figure 7.4a. The [Cl/Si] ratio between $3x10^{15}$ and $3x10^{16}/cm^2$ were higher at 40eV than at 100eV and produced a slight decrease at higher doses of $3x10^{17}$ and $1x10^{18}/cm^2$. This decrease at the greatest doses was in contrast to the gradual increase in [Cl/Si] ratio for 100eV ion bombardment.

For this case of 40eV chlorine ion bombardment over the ion dose range of $3x10^{15}$ to $1x10^{18}/cm^2$, it is believed that the interaction between the incident ion and the surface was primarily due to Cl^+ bombardment of the surface oxygen, e.g. Si-$(O\text{-}X)_4$ with X=Cl or Si. The Cl^+ ion was less efficient in removing the Si-$(O\text{-}X)_4$ compared to 100eV bombardment and a greater amount of surface Cl was present to react with the oxygen contamination present after HF-etching of the Si surface. As the ion dose increased, the slight reduction in surface chlorine at 40eV bombardment was due to an increased physical sputter-removal of the Si-$(O\text{-}X)_4$ species.

Figures 7.5 and 7.6 show the high resolution Cl2p core-level spectra at two different doses for 100eV and 40eV ion bombardment, respectively. Figure 7.5 indicates the complete removal of Cl-O-Si species for 100eV Cl^+ ions at the highest dose of $1.5x10^{18}/cm^2$. These species were removed as a result of physical sputtering and perhaps ion radiation-enhanced desorption. Figure 7.6 shows that only partial removal of the Cl-O-Si species for 40eV Cl^+ ions at the highest dose of $1x10^{18}/cm^2$. The degree of desorption for the oxygenated chlorosilyl species was less at 40eV due to reduced

Figure 7.5 XPS high resolution spectra of the Cl2p core-level for Cl^{+} ion bombardment at 100eV showing the effects of ion dose at $3x10^{15}$ and $1.5x10^{18}$ions/cm^2.

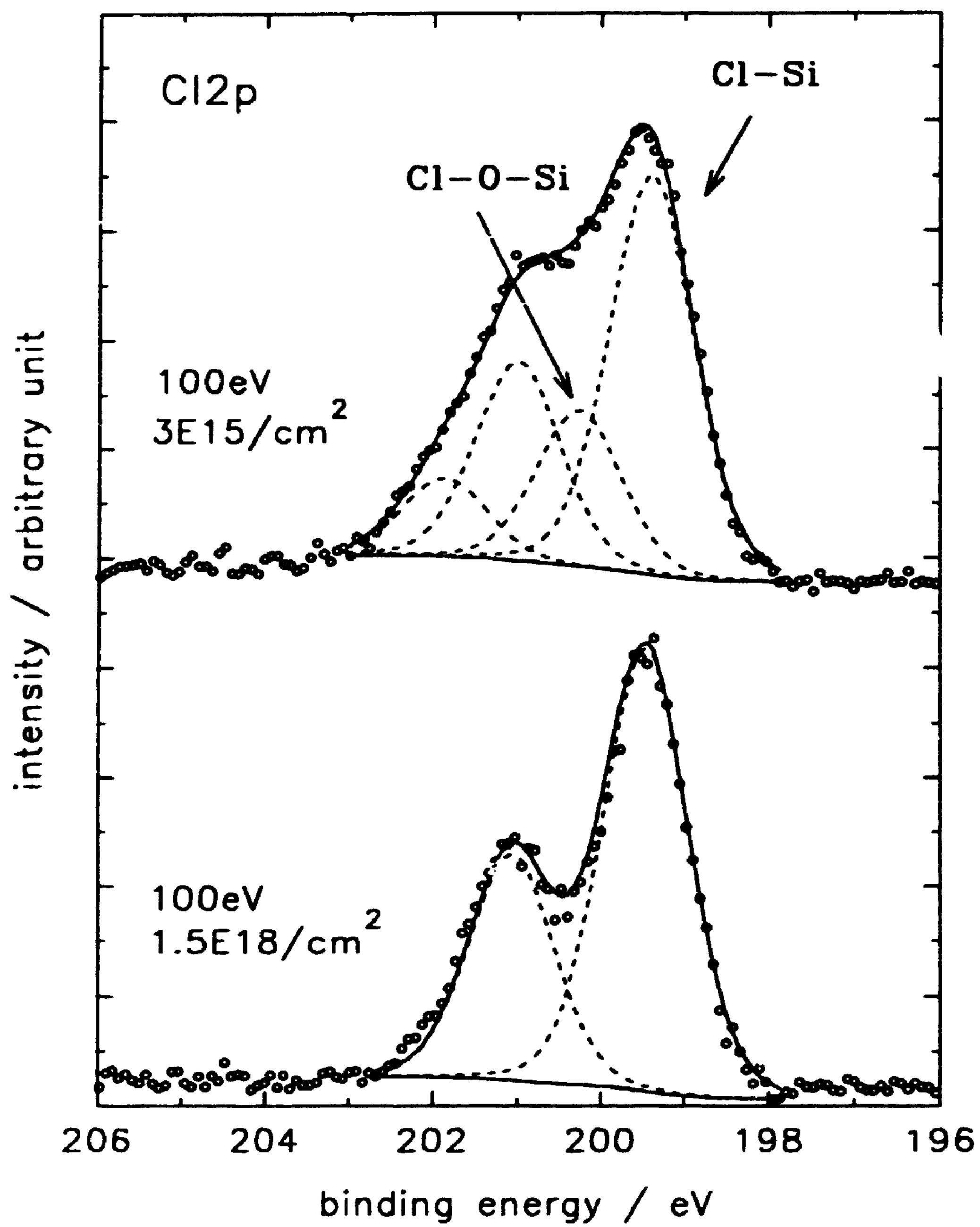

Cl2p
Cl-Si
Cl-O-Si
100eV
3E15/cm2
100eV
1.5E18/cm2
intensity / arbitrary unit
206
204
202
200
198
196
binding energy / eV

Figure 7.6 **XPS high resolution spectra of the Cl2p core-level for Cl^+ ion bombardment at 40eV showing the effects of ion dose at $3x10^{15}$ and $1x10^{18}$ions/cm^2.**

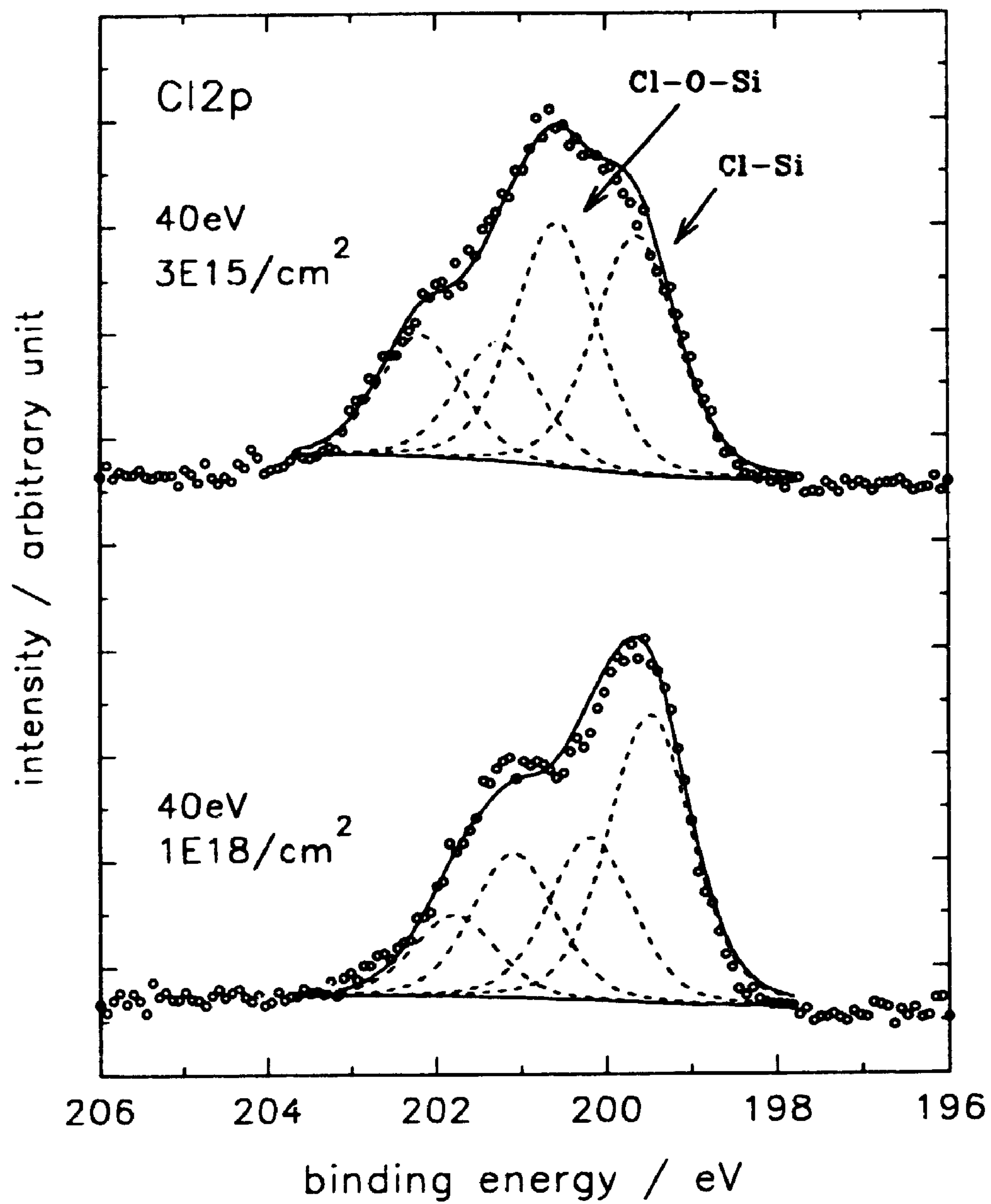
Cl2p
Cl-O-Si
Cl-Si
40eV
3E15/cm2
40eV
1E18/cm2
intensity / arbitrary unit
206
204
202
200
198
196
binding energy / eV

energies of the collisional cascades (physical sputtering) compared to the 100eV case Ion-enhanced radiation may have contributed to the desorption of the Cl-O-Si species at 40eV, but such radiation effects were less than at 100eV

The differences between Figures 7.5 and 7.6 are then ascribed to physical sputtering of the surface Si-$(O-X)_4$ species. For the 100eV case, these species were completely removed at the highest dose, and Figure 7.5 illustrates this clearly, while at 40eV Cl^+ bombardment, the Cl-O-Si component was still present after the highest dose of $1x10^{18}/cm^2$ (Figure 7.6). The presence of surface Si-$(O-X)_4$ species resulted in the larger amounts of surface chlorine for the 40eV case in comparison to the 100eV case

Figure 7.7 shows the Si2p spectra corresponding to Figure 7.6 for 40eV ion bombardment. It was instructive to compare the control spectra representing a region of the same Si sample not exposed to Cl^+ ion beam. At a dose of $3x10^{15}/cm^2$, the dominant peak at 99.3eV produced a detectable broad component towards higher binding energy which was absent from the overlayed control surface spectrum This component was assigned earlier in section 7.3.1 to Si-$(O-X)_4$ with X=Cl or Si species resulting from the initial reaction of Cl^+ ions with the O surface contamination As the dose increased to $1x10^{18}/cm^2$, this Si-O-Cl component was completely removed (Figure 7.7) The behaviour suggests that initial Cl^+ ions reacted with surface O, and once all the O was consumed, the subsequent Cl^+ ions impinging at the greater doses sputtered away these Si-O-Cl species

A comparison of the Si2p spectra in Figure 7.7 shows that the semiconductor Si component near 99eV binding energy was shifted slightly towards higher binding energy with increased dose with respect to the control spectra This binding energy shift was

Figure 7 7 XPS high resolution spectra of the Si2p core-level for Cl^+ ion bombardment at 40eV showing the effects of ion dose at $3x10^{15}$ and $1x10^{18}$ ions/cm^2.

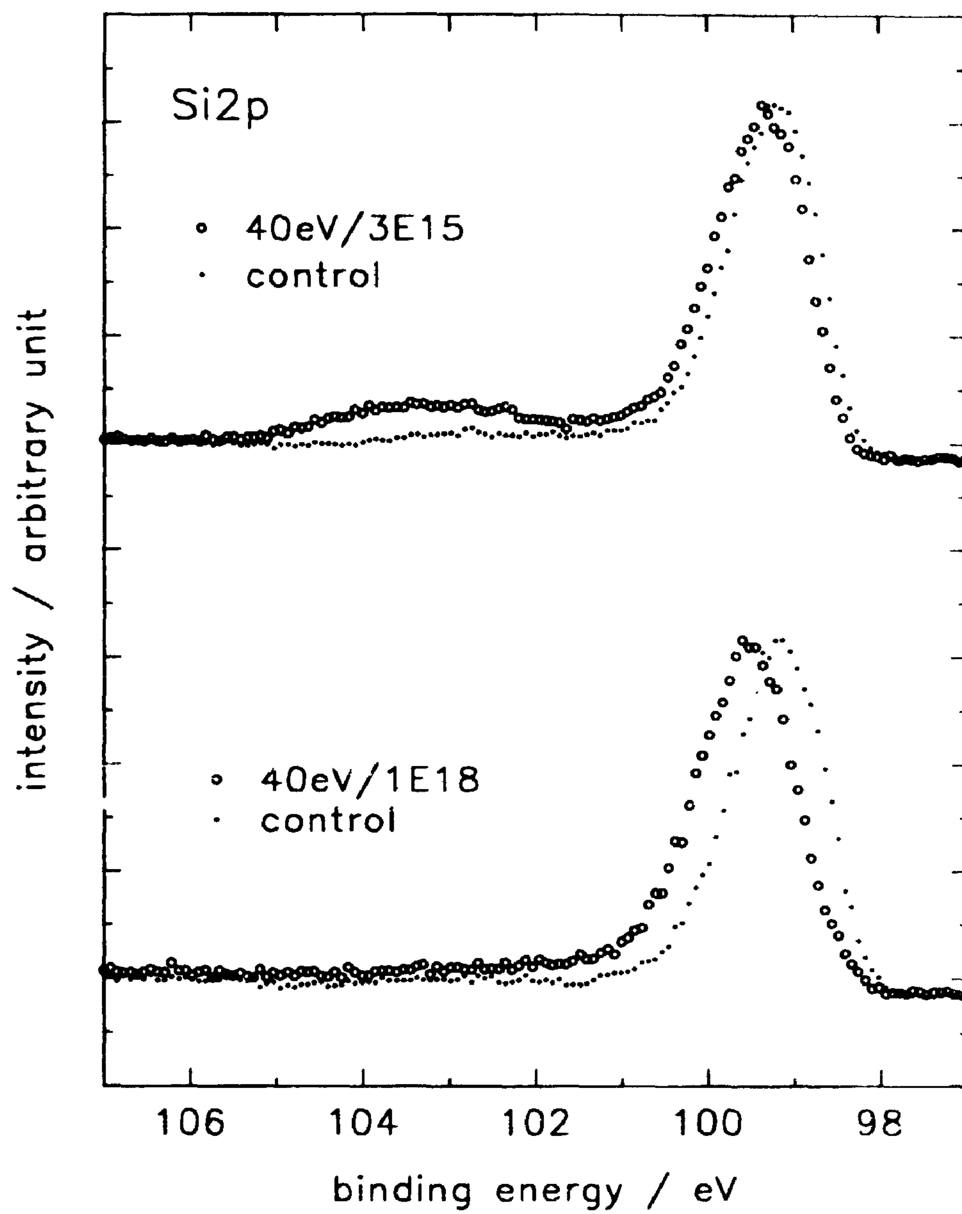
Si2p
40eV/3E15
control
40eV/1E18
control
intensity / arbitrary unit
106
104
102
100
98
binding energy / eV

observed in Figure 7.2 at 20eV and indicates that the Cl^+ bombardment induced surface band-bending of the Si(100). Thus, the surface Fermi level was being shifted away from the valence band maximum for this case of p-type Si as a result of increasing ion dose. Because Cl is a highly electronegative species, its presence in the disordered Si surface region could have been identified as an effective n-type dopant and altered the surface semiconducting properties.

The case for 100eV Cl^+ bombardment of the Si surface was similar to 40eV bombardment with complete removal of the broad component towards higher binding energy from the Si2p spectrum as was seen in Figure 7.7 for the high doses. At 100eV Cl^+ impingement on the Si surface, the physical sputtering effect was considered to be significant as has been described in the previous section. Hence, the surface contamination species were eventually sputtered away at higher doses.

The shift in binding energy for the semiconducting Si peak was more pronounced at 100eV than at the 40eV case described above. This suggests that surface band-bending induced by energetic Cl^+ ion exposure was greater at the higher ion energies. Figure 7.8 shows plots of the surface Fermi level as a function of ion fluence at 100eV and 40eV for the p-type Si(100) material. At doses near $1\times10^{15}/cm^2$ in both cases, the Fermi level was already near the middle of the Si bandgap. While at the highest doses for 100eV bombardment, the surface was n-type. Since argon bombardment merges the surface Fermi levels of n-type and p-type Si to the midgap [7.21], the type-inversion induced by Cl^+ ion bombardment is not considered to be due to simple radiation-induced defects in the silicon. Instead, it is likely caused by chlorine incorporation.

Analyses of the Si2p data for samples receiving a dose of over $1\times10^{18}/cm^2$ at

Figure 7.8 Effect of ion dose on surface Fermi level position as a result of Cl^+ ion bombardment at (a) 100eV, and (b) 40eV

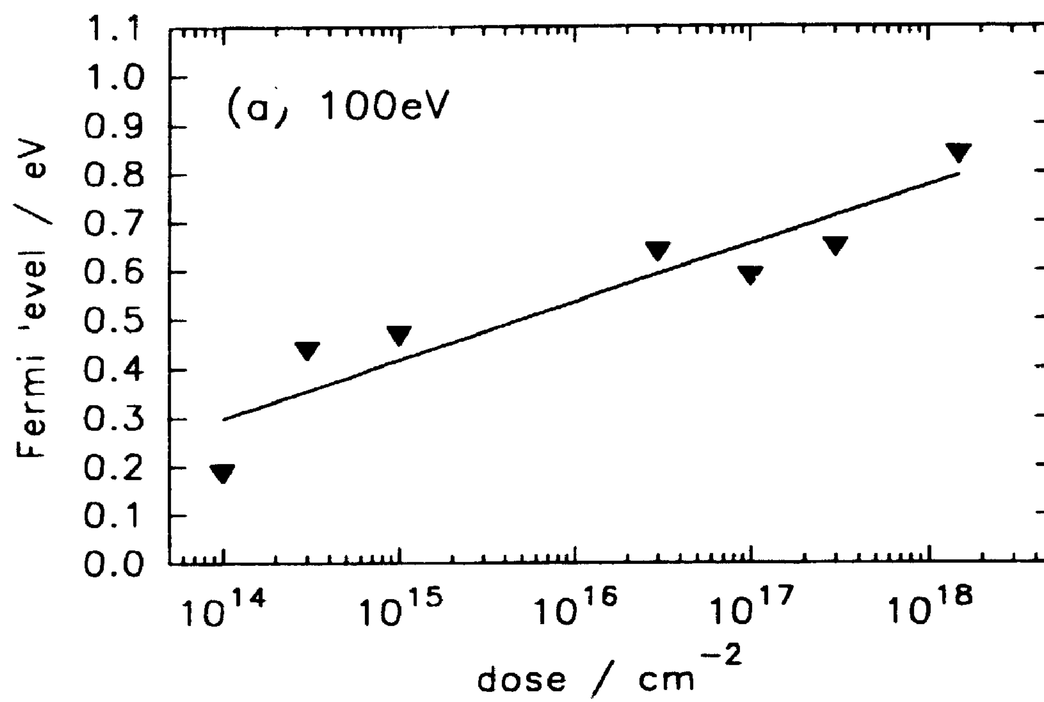

(a) 100eV
Fermi level / eV
dose / cm−2

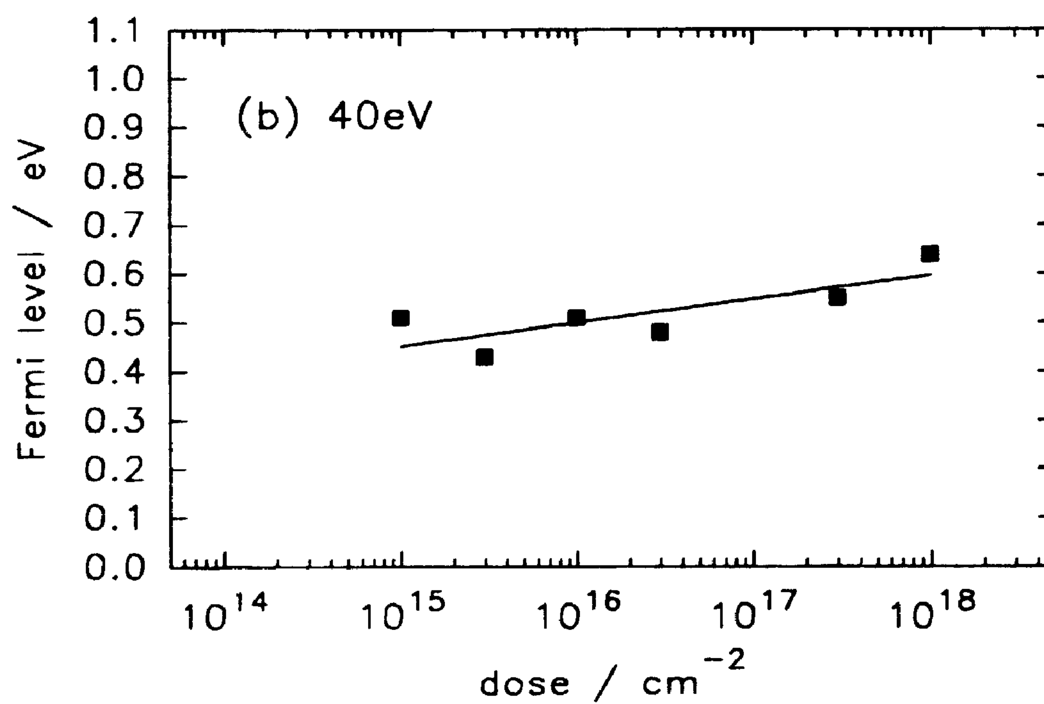

(b) 40eV
Fermi level / eV
dose / cm−2

bombardment energies higher than 40eV showed that $SiCl_n$ species with n=1 could be found as a minor component chemically shifted approximately 1eV towards higher binding energy compared to the semiconducting Si peak near 99eV binding energy. It is believed that a chlorosilyl layer formation occurs analogous to the fluorosilyl layer (SiF_n, n=1,2,3,4) of the F/Si system [7.10]. The development of stable chlorosilyl species with n>1 was not observed within detection limits by XPS. It is known that $SiCl_2$ is emitted from a silicon surface simultaneously receiving chlorine and an argon ion beam [7.12-14]. This gas phase species is considered to be the dominant etch product for the Cl etching of Si at room temperature [7.11]. The presence of only the mono-chlorosilyl ($SiCl_1$) species suggests that surface reaction pathways toward the formation of stable di- and tri-chlorosilyl surface species were not observed from this work of Cl^+ ion bombardment of Si(100) in the energy range studied.

Effective silicon etching by a chlorine ion beam was also confirmed in this study by the observation of etch-craters for samples receiving high doses at 20-100eV. Whitman et al [7.33] studied molecular chlorine exposed to Si(111). Such results reported the presence of $SiCl_3$, $SiCl_2$ and SiCl surface species. However, there has not been any reported characterization of a chlorosilyl layer formed as a result of Cl^+ ion etching of Si(100) [7.11]. The results from this work showed no room temperature stable $SiCl_n$ surface species for n>1.

Cl^+ bombardment results in more efficient etching of the radiation damaged region than Ar^+ bombardment, and the radiation damage is very shallow in this low energy regime [7.17,28]. In this sense, Cl^+ bombardment is better than Ar^+ sputtering in removing surface contamination on Si. Any residual Si-Cl surface species can be

removed by a subsequent ozone oxidation plus HF-etch to remove the oxide [7.34]. This process is feasible because the presence of chlorine on the silicon surface has been shown to enhance the silicon oxidation rate [7.35].

7.4 Conclusions

Cl^+ bombardment was effective in transforming any residual surface oxygen on Si to surface oxygenated species such as Cl-O-Si . These species can then be removed by further Cl^+ bombardment at higher energy and doses, mainly via physical sputtering. Once the oxygenated species were removed, subsequent Cl^+ bombardment etched the Si surface appreciably. The energetic Cl^+ ion interaction with the Si(100) surface produced residual surface damage in the form of Cl incorporation and surface lattice disorder. The amount of surface Cl increased with lower ion kinetic energy in the range of 100eV to 40eV This behaviour was believed to be attributed to less efficient physical sputtering of the surface oxide. The Cl incorporation also produced surface band-bending as a function of both ion kinetic energy and fluence with the p-type Si(100) being converted to n-type for 100eV bombardment at $1\times10^{18}/cm^2$

REFERENCES

7.1 S.J. Fonash, Solid State Technol., 28, 150, 1985

7.2 D. Bollinger, S. Iida, O. Matsumoto, Solid State Technol., 27, 111, 1984

7.3 L. Holland, S.M. Ojha, Vacuum, 26, 53, 1976.

7.4 J.W. Coburn, H.F. Winters, J. Appl. Phys, 50, 3189, 1979

7.5 H.B. Pogge, J.A. Bondur, P.J. Burkhardt, J.Electrochem Soc., 130(7), 1592, 1983

7.6 C.J. Mogab, H.J. Levinson, J. Vac.Sci. Technol., 17, 721, 1980

7.7 G.S. Oehrlein, J.F. Rembetski, E.H. Payne, J Vac.Sci Technol., B8, 1199, 1990

7.8 D.L. Flamm, V.M. Donnelly, Plasma Chem. Plasma Proc., 1, 317, 1981

7.9 Y. Zhang, G.S. Oehrlein, E. de Fresart, J.W. Corbett, J Appl Phys, 71(4), 1936, 1992.

7.10 F.R. McFeely, J.F. Morar, F.J. Himpsel, Surf. Sci., 165, 277, 1986

7.11 H.F. Winters and J.W. Coburn, Surf. Sci. Rep., 14, 161, 1992 and references therein.

7.12 F.H.M. Sanders, A.W. Kolfschoten, J. Dieleman, R.A. Haring, A Haring, and A E de Vries, J. Vac. Sci. Technol., A2, 487, 1984.

7.13 D J. Oostra, R.P. van Ingen, A. Haring, A.E de Vries, and G N A van Veen, Appl. Phys Lett. 50, 1506, 1987

7.14 D.J. Oostra, A. Haring, R.P. van Ingen, and A E. de Vries, J Appl Phys, 64, 315, 1988

7.15 B.R. Appleton, S.J. Pennycook, R A Zuhr, N Herbots, T S Noggle, Nucl Instrum Meth, B19/20, 975, 1987

7.16 R.A. Zuhr, S.J. Pennycook, T.S. Noggle, N. Herbots, T.E. Haynes, B.R. Appleton, Nucl. Instrum. Meth., B37/38, 16, 1989.

7.17 A.H. Al-Bayati, K.G. Orrman-Rossiter, D.G. Armour, Surf. Sci., 249, 293, 1991.

7.18 S. Kostic, D.G. Armour, G. Carter, in Materials Modifications by High-fluence Ion Beams, edited by R. Kelly, M. Fernanda da Silva, Kluwer Academic Publishers, Dordrecht, 237, 1989.

7.19 J.F. Moulder, W.F. Stickle, P.E. Sobol, K.D. Bomben, in PHI Handbook of X-ray Photoelectron Spectroscopy, edited by J. Chastain, Perkin-Elmer Corporation, Eden Prairie, 1992 and references therein.

7.20 W.M. Lau, J. Appl. Phys., 67(3), 1504, 1990.

7.21 L.J. Huang, W.M. Lau, J. Vac. Sci. Technol., A10, 812, 1992; and references therein.

7.22 M. Niwano, H. Katakura, Y. Takeda, Y. Takakuwa, N. Miyamoto, A. Hiraiwa, K. Yagi, J. Vac. Sci. Technol., A9(2), 195, 1991.

7.23 J.A. Yarmoff, D.K. Shuh, T.D. Durbin, C.W. Lo, D.A. Lapiano-Smith, F.R. McFeely, and F.J. Himpsel, J. Vac. Sci. Technol. A10, 2303(1992).

7.24 S. Tanuma, C.J. Powell, D.R. Penn, Surf. Interface Anal., 17, 911, 1991.

7.25 E.A. Ogryzlo, D.E. Ibbotson, D.L. Flamm, and J.A. Mucha, J. Appl. Phys., 67(6), 3115, 1990

7.26 G.V. Jorgenson, G.K. Wehner, J. Appl. Phys., 36, 2672, 1965.

7.27 W.M. Lau, I. Bello, L.J. Huang, X. Feng, M. Vos, I.V. Mitchell, J. Appl. Phys. (in press)

7.28 A.H. Al-Bayati, K.G. Orrman-Rossiter, R. Badheka, D.G. Armour, Surf. Sci., 237,

213 (1990)

7.29 S.M. Sze, in Physics of Semiconductor Devices, Wiley-Interscience, New York, 1981.

7.30 J.R. Waldrop, R.W. Grant, J. Vac. Sci. Technol., B6, 1432, 1988

7.31 W.M. Lau, Appl. Phys. Lett., 54, 338, 1989.

7.32 J. Linnros, R.G. Elliman, W.L. Brown, J. Mater. Res., 3, 1208, 1988

7.33 L.J. Whitman, S.A. Joyce, J.A. Yarmoff, F.R. McFeely, L.J. Terminello, Surf. Sci., 232, 297, 1990.

7.34 W.M. Lau, L. Huang, W.H. Chang, M. Vos, I.V. Mitchell, Appl. Phys. Lett., 63(1), 78, 1993.

7.35 P.K. Charvat, E.E. Krueger, A.L. Ruoff, J. Vac. Sci. Technol., B4(4), 812, 1986

CHAPTER 8.

GENERAL SUMMARY

8.1 Conclusions

The conclusions from the work discussed in this thesis may be summarized generally in the following points:

(i) for surface characterization of p-type Si(100) after RIE:

(a) ultrashallow depth-profiling by ozone oxidation and HF oxide wet etching followed by XPS and SCS surface analysis has been used successfully for analyzing the residual surface damage induced in a commercial RIE system;

(b) these processing and analytical techniques have been shown to provide a means for identifying species confined to shallow depths of 0.5nm within the surface region, and the identification and removal of surface Fermi level pinning;

(ii) for surface reactions induced by $^{19}F^+$ ion bombardment:

(a) the surface fluorination of p-type Si(100) by low energy F^+ ions results in an increase in F incoporation with dose producing increases in surface crystalline damage, an increase in surface fluorosilyl species formation which was stable at room temperature under UHV

conditions, and an increase in surface band-bending with the surface no longer p-type;

(c) F^+ ion bombardment resulted in a thin fluorosilyl species layer which was not significantly dependent on ion energy between 20 and 100eV;

(d) the effect of vacuum heating the Si surface bombarded by F^+ resulted in greater fluorine desorption at the lowest energies.

(iii) for surface reactions induced by CF^+ ion bombardment

(a) the interactions of p-type Si(100) with low energy CF^+ ion bombardment showed that different surface reaction pathways were "switched" at different ion kinetic energy regimes with molecular adsorption and surface scattering occurring at 2eV, fluorocarbon film deposition between 10 and 60eV, and significant subsurface penetration resulting in silicon carbide and fluorosilyl speciation at 80 and 100eV,

(b) non-destructive depth-profiling by angle-resolved XPS analysis of the carbide-fluorosilyl layer formed on silicon after 100eV ion bombardment showed that the fluorosilyl layer was above the silicon carbide layer in the surface region,

(iv) for surface reactions induced by $^{35}Cl^+$ ion bombardment

(a) the effect of Cl^+ ion bombardment of p-type Si(100) showed that there was not an appreciable formation of $Si\text{-}X_n$ (where X = F or Cl,

n~1) compared to the F^+/Si(100) over the same ion energy range of 20 to 100eV,

(b) the interaction of the Cl^+ ions with residual contamination of oxygen was detected, and this surface oxygen contaminant was only removed by physical sputtering,

(c) the Cl^+ bombardment also was seen to induce surface band-bending with type inversion occurring at the highest doses investigated in this thesis

8.2 Future recommendations

The work presented in this thesis may be continued in a number of different directions The interactions of very low energy reactive ions both atomic and molecular with the Si(100) surface may be investigated in future work with the following suggestions

(a) the measurement of total etch yield of single crystal silicon as a function of different reactive atomic ions such as F^+ and Cl^+ and ion kinetic energy in the range of 20 to 100eV is important to the understanding of reactive ion etching using high density plasma (HDP) systems,

(b) the effect of silicon substrate temperature on the surface reactions induced by the reactive ions studied in this thesis is important in determining a suitable temperature for minimizing dry etch-induced

residual surface damage;

(c) the studies presented in this thesis using Si(100) as the substrate material can be repeated using a thin SiO_2 overlayer because invariably the selectivity betweeen Si and SiO_2 will be different using HDP etching compared to conventional RIE